NOVA SCHOOL OF SCIENCE & TECHNOLOGY

DEPARTMENT OF PHYSICS

ANDRÉ FILIPE DOS SANTOS ROSA

Bachelor Degree in Biomedical Engineering Sciences

SINGLE-STEP LASER-INDUCED GRAPHENE ON PAPER AS A PLATFORM FOR MONITORING PH WITHIN SMART BANDAGES FOR WOUND APPLICATION

MASTER IN BIOMEDICAL ENGINEERING

NOVA University Lisbon
April, 2022

NOVA SCHOOL OF SCIENCE & TECHNOLOGY

DEPARTMENT OF PHYSICS

SINGLE-STEP LASER-INDUCED GRAPHENE ON PAPER AS A PLATFORM FOR MONITORING PH WITHIN SMART BANDAGES FOR WOUND APPLICATION

ANDRÉ FILIPE DOS SANTOS ROSA

Bachelor Degree in Biomedical Engineering Sciences

Adviser: Elvira Fortunato
Full Professor, NOVA University Lisbon

Examination Committee

Chair: Ricardo Nuno Pereira Verga e Afonso Vigário
Full Professor, FCT-NOVA

Rapporteur: Ana Cecília Afonso Roque
Full Professor, FCT NOVA

MASTER IN BIOMEDICAL ENGINEERING

NOVA University Lisbon
April, 2022

Single-step laser-induced graphene on paper as a platform for monitoring pH within smart bandages for wound application

Para os meus pais e irmã.
Para os meus avós.

Acknowledgements

Chego ao fim desta importante etapa com uma enorme alegria por ter sido parte desta enorme casa que é a FCT NOVA. Levo comigo experiências, conhecimento e, acima de tudo, pessoas que espero sempre ter ao meu lado.

Deixo o meu agradecimento à Professora Elvira Fortunato por me ter concedido a oportunidade de concluir esta etapa no CENIMAT|i3N, reunindo as condições necessárias ao desenvolvimento deste projeto. Ao Tomás, agradeço por todo o apoio ao longo desta dura jornada, por me ter orientado da melhor forma possível estando sempre presente, dentro e fora de campo. À restante equipa do CENIMAT|i3N, tenho a agradecer todo o conhecimento partilhado e a forma como me acolheram durante este período.

Ao Enguiça, Xico, Sérgio e Braga, obrigado por partilharem comigo esta paixão pela música, que tantas vezes serviu de escape para os piores momentos, e por acreditarem tanto como eu nos Green Leather e naquilo que queremos alcançar. Juntos passámos por grandes momentos e sei que muitos mais virão.

Mité, Silva e Rita, não me poderia ter calhado melhor família, e ao fim destes anos agradeço-vos por terem sido autênticos irmãos mais velhos que me guiaram por bons e (às vezes) "maus caminhos".

Aos meus lindos Ortiz, Daniela, Luísa, Maria e Carina, obrigado por todos os dias ensinarem algo novo a este velho e estarem ao meu lado a cada nova etapa, cada convívio, cada fofoca, cada jantar, ou mesmo à distância.

À Mara, Melo, Coutinho, Correia e Zagalo, obrigado por todas as cantinas do meio-dia, café da uma e cervejas das cinco que por tantas vezes me limparam a cabeça quando mais precisava.

Aos meus 11 macacos: Megs, Martinha, Babel, Barrocas, Rita, Dô, Marinha, Braga (outra vez), Joana, Bruninho, Madeira, obrigado por terem sido o melhor que esta casa me deu nestes 5 anos (e meio), e que para sempre continuemos a criar histórias como as que hoje nos fazem chorar, rir, e chorar a rir.

Um obrigado especial à Joana, minha cientista, por ainda ter paciência para mim ao fim deste tempo todo, por me dar na cabeça e manter-me em sentido quando foi preciso, por todos os bons e maus episódios ultrapassados para chegar até aqui.

À minha família tenho a agradecer por todo o esforço para me trazer até aqui, todos os ensinamentos e todo o apoio incondicional sem os quais jamais seria a pessoa que sou hoje.

"Só olho para a estrada antes da curva, porque não posso ver senão a estrada antes da curva." (Alberto Caeiro)

Abstract

Chronic wounds and wound infection occurrences have become major public health concerns over the last years, affecting millions of people and costing billions to national healthcare systems. Many of these incidents are avoidable through proper monitoring of the wound health status.

The boom of wearable sensors for *in situ* monitoring of relevant biomarkers like temperature, humidity, glucose concentration, and other analytes have shown to be viable pathways to continuous injury monitoring for chronic status and infection prevention. Among these analytes, pH has been a much-neglected parameter despite having a strong correlation with the wound healing status. Acute wounds initially present acidic pH levels (≈4), while chronic wounds oscillate indefinitely at higher pH levels (≈8).

The discovery of laser-induced graphene (LIG) gave rise to the development of low-cost, flexible electrodes for the fabrication of biosensors on a multitude of recyclable and sustainable substrates, namely on paper.

This dissertation project contributes to the research and optimization of LIG on paper as a medium for the fabrication of environmentally friendly, low-cost, and biocompatible pH sensors for future implementation within smart bandages and medical wound dressings. LIG on paper fabrication parameters were optimized for better electrical performance, having reached a sheet resistance value of $14.0 \pm 1.50\ \Omega\ \mathrm{sq}^{-1}$. LIG-based pH sensors were conceived based on a voltammetric approach by modifying the working electrode with riboflavin (vitamin B_2) and monitoring its electrochemical response to different pH environments. The proposed device showed Super-Nernstian sensitivity of $78.2 \pm 3.37\ \mathrm{mV\ pH}^{-1}$ over a 2 to 8, physiologically relevant, pH range, making it suitable for the application within a wound environment.

Keywords: laser-induced graphene, paper, pH, wound monitoring, chronic wounds, biosensors, sustainable electronics

Resumo

Feridas crónicas e as ocorrências de infeção em feridas são atualmente grandes preocupações de saúde pública, afetando milhões de pessoas e custando milhares de milhões aos sistemas nacionais de saúde. Muitos destes incidentes são evitáveis através de uma monitorização adequada do estado de regeneração dos ferimentos.

A expansão dos sensores *wearable* para monitorização localizada de biomarcadores relevantes como temperatura, humidade, concentração de glucose, e outros analitos, tem demonstrado ser uma possível via de controlo contínuo do estado destas lesões, para prevenção da evolução para situação crónica e do surgimento de infeções. Entre estes analitos, o pH tem sido um parâmetro muito negligenciado, apesar de ter uma forte correlação com a fase de cicatrização da ferida. As feridas agudas apresentam inicialmente níveis de pH ácidos ($\approx$4), enquanto que as feridas crónicas oscilam indefinidamente entre níveis de pH mais elevados ($\approx$8).

A descoberta do grafeno induzido por laser (LIG) deu origem ao desenvolvimento de elétrodos flexíveis e de baixo custo para o fabrico de biossensores, tendo por base diversos substratos recicláveis e sustentáveis, nomeadamente o papel.

Este projeto de dissertação contribui para a investigação e otimização da produção de LIG em papel como meio para o fabrico de sensores de pH ecológicos, de baixo custo e biocompatíveis. Isto visando a implementação futura em pensos inteligentes e curativos médicos. Foi realizada a otimização dos parâmetros para fabricação do LIG em papel, tendo atingido valores de resistência em folha de $14.0 \pm 1.50\ \Omega\ \mathrm{sq}^{-1}$. Os sensores de pH baseados em LIG foram concebidos com base numa abordagem voltamétrica, modificando o elétrodo de trabalho com riboflavina (vitamina B_2) e monitorizando a sua resposta eletroquímica a ambientes com diferentes valores de pH. O dispositivo proposto mostrou sensibilidade Super-Nernstiana de $78.2 \pm 3.37\ \mathrm{mV\ pH}^{-1}$ ao longo de uma janela de pH fisiologicamente relevante de 2 a 8, tornando-o adequado para a aplicação em ferimentos.

Palavras-chave: grafeno induzido por laser, papel, pH, monitorização de feridas, feridas crónicas, biosensores, eletrónica sustentável

Contents

List of Figures

List of Tables

Constants

π	the numerical value of pi	3.1416
$\mathbf{D}_o$	diffusion coefficient for ferricyanide in KCl (0.1 M)	7.2×10^{-6} cm^2 s^{-1}
$\mathbf{D}_r$	diffusion coefficient for ferrocyanide in KCl (0.1 M)	6.7×10^{-6} cm^2 s^{-1}
F	Faraday constant	96485.33 C mol^{-1}
R	universal gas constant	8.314 J K^{-1} mol^{-1}

Acronyms

0D	zero-dimensional
1D	one-dimensional
2D	two-dimensional
3D	three-dimensional
AE	auxiliary electrode
BR	Britton-Robinson
CE	counter electrode
CV	cyclic voltammetry
CVD	chemical vapour deposition
CW	chronic wound
ECA	electrochemically active surface area
EDS	energy-dispersive X-ray Spectroscopy
EMF	electromotive force
GA	geometric area
IUPAC	International Union of Pure and Applied Chemistry
LDW	laser-direct writing
LIG	laser-induced graphene
MRS	micro-Raman spectroscopy
PA	polyamide
PANI	polyaniline
PBI	polybenzimidazole
PEI	polyetherimide

PET polyethylene terephthalate
PI polyimide
PPI pulses per inch

RE reference electrode
RGB red, green and blue
RSD relative standard deviation

SCE saturated calomel electrode
SD standard deviation
SEM scanning electron microscopy
SHE standard hydrogen electrode
SSI surgical site infection
SWV square wave voltammetry

WE working electrode
WI wound infection

XPS X-ray photoeletron spectroscopy

Symbols

α	charge transfer coefficient
A	amperes
$\mathbf{A}_e$	electrode's electrochemicaly active surface area
cm	centimeters
D	diffusion coefficient
°	degrees
dm	decimeters
E	measured potential
$\mathbf{E}^0$	standard electrode potential
eV	electron volts
g	grams
Hz	hertz
”	inches
k^0	heterogeneous electron transfer rate
keV	kiloelectron volts
km	kilometers
M	molar concentration
mA	milliamperes
µA	microamperes
µL	microliters
µm	micrometers
mL	milliliters
mm	millimeters

mM millimolar
mol moles
mV millivolts

nm nanometers

°C degrees Celsius
Ω ohms

pA picoamperes

s seconds
sq square
$\mathbf{R}_s$ sheet resistance

T temperature in Kelvin

v scan rate
V volts

W watts

ψ kinetic parameter

Chapter 1

Introduction

The introductory chapter has in view the global analysis and contextualization of the field of study in question. Worldwide stats and essential concepts are provided as a means to explore the motivation for developing the proposed device. Moreover, a brief description of the objectives of this project is presented.

1.1 Context and Motivation

Chronic wounds (CWs) and general wound infections (WIs) have become major public health concerns due to their implications for both the patients and the healthcare system [29, 88, 5]. Although it is hard to infer on the worldwide prevalence of surgical site infections (SSIs) because of the lack of standardized evaluation techniques, a World Health Organization study found that 5 to 34 % of nosocomial infections are WIs. This is an underestimate since it does not take into account the number of SSIs treated without hospital mediation after the patients are discharged. These occurrences come with great expense, costing the United Kingdom's National Health Service roughly 1 billion pounds per year [80]. Furthermore, the prevalence of CWs in patients is a significant burden as well, affecting over 5.7 million people in the United States and leading to 20 billion dollars worth of expenses to the US Healthcare System each year [88]. CWs are also a deadly condition, exhibiting a 5-year mortality rate of 50 % [77]. A strong correlation between CWs and the prevalence of diabetes has been reported with diabetic patients having a 15 to 25 % risk of developing diabetic foot ulcers and accounting for 97.2 % of neuro-ischaemic ulcer occurrences [43]. Despite the significant numbers, there is no tendency to their decrease, with studies showing that, in the Tropics, there was a rise of 95.1 % in wound-related inpatient admissions between 2013 and 2017 [43].

Although it is not feasible to extinguish these occurrences, research shows that 55 %

of SSIs are avoidable through evidence-based strategies [90]. It is imperative to find new ways to tackle this global issue in order to relieve the strain of millions of people, both patients and clinicians, as well as to reduce immensely the economic burden it brings to healthcare systems [43].

Monitoring wound status *in situ* through the analysis of parameters like temperature [62], pH [67], glucose [28] and other biomarkers throughout its healing stages has been viewed as a way to face the previously mentioned issues. The need for new wearable devices able to perform real-time monitoring, diagnosis, and conduct local therapy is now recognized [62, 5, 97]. This can lead to promising results by reducing hospitalization time, the number of unnecessary doctor appointments, patient travels to healthcare facilities, expensive lab testing for diagnosis, and with that, preventing WIs and better manage CW condition [5].

The hydration level within the wound environment is one of the essential factors to take into account in wound care. Providing the wound bed with adequate moisture concentration is key to facilitating and enabling the several stages of wound healing at their full potential, contrasting with a dry environment, which can lead to a longer healing process and other complications [59, 53]. Water is responsible for triggering biochemical processes involved in the vascularization, granulation, and re-epithelialization stages [9]. In the work of Rippon et al. [72] hyper-hydration is described as a highly beneficial wound healing model. However, excess fluid can also hamper wound healing, leading to maceration and moisture-associated skin damage due to extensive contact with wound exudate. This fluid of corrosive nature is typically more abundant during the inflammatory stage of the wound healing process, although in many CWs it becomes long-lasting [9, 72].

Schneider et al. [75] reported wounds as "a large biological building site" in which damaged cells and tissue are gradually replaced by new ones through the action of several protein-degrading enzymes, neutrophils, and cytokines [9]. Notwithstanding being wounding agents, it is logical to deduce that an excess of wound exudate may lead to corrosion of the surrounding tissue, expanding the wound rather than aiding its closure [72]. Furthermore, this constraint on wound healing increases the possibility of WI and other complications [9, 72, 53].

The metabolic rate is very high at the wound site during its regeneration [75]. The chemical composition of wound exudate also varies a lot while the regeneration process takes place, presenting distinct values of parameters like pH that can be indicative of the healing stage and WI eminence [97, 67].

The pH value is a representation of the concentration of hydrogen ions, acquired from the negative logarithm of this concentration ($pH = -\log[H^+]$) [30]. As such, pH, directly and indirectly, influences all biochemical reactions occurring at the wound site. Even so, pH is still a much-neglected parameter in the field of wound care and outcome prediction [75].

For several decades, it has been widely accepted that a low pH is a solid precursor to

wound healing. An acidic pH, similar to that of the skin, which acts as a physiological barrier to bacteria proliferation, is key to healthy wound regeneration. Research states that acute wounds and wounds that reveal positive healing progress are characterized by an acidic pH. On the other hand, injuries that show a propensity to reach a chronic or infected status tend to have alkaline pH values (see Figure 2.3) [75, 67, 5, 51].

This dynamic behavior of pH during the healing stages boosted the need for monitoring this parameter. Despite the existence of several sensors capable of performing *in situ* wound exudate analysis, active pH monitoring devices have received much less attention [9]. A higher offer and better accessibility of pH monitoring sensors can lead to improvements in wound condition assessment, CW monitoring, and early detection of complications such as onset of infection and moisture-associated skin damage.

In recent years, the progress of laser-direct writing (LDW) technology and the discovery of laser-induced graphene (LIG) has led to the development of low-cost and flexible electrodes [73] that can be easily integrated onto existing wound dressings and monitor pH through electrochemical response oscillations [9, 97]. The ultimate goal of this up-and-coming technology is to be able to perform local wound status diagnostics as well as on-demand therapy [5, 62], and wirelessly communicate with the patient or clinician providing them with the necessary data to apply proper therapy [9, 62].

One keynote that may dictate both the feasibility and potential use of these devices is the substrate on which they're fabricated. Nowadays, graphene-based sensors can be created on all sorts of base platforms, such as polyimide (PI) [9, 48, 73, 5], polyethylene terephthalate (PET) [55, 63, 5] and other polymers. Although these have shown great results, paper-based graphene sensors have an extremely high economic potential seeing that paper is the cheapest known substrate [49]. Furthermore, cellulose, the main component of paper, is also widely available on Earth, making it a truly low-cost, flexible substrate [49, 87]. To put into perspective, the price of paper is about 0.1 cent dm^{-2}, while PET costs around 2 cent dm^{-2}, and PI 30 cent dm^{-2}. Beyond the low cost, paper also has a fast roll-to-roll manufacturing process, sometimes exceeding 100 km h^{-1}, and it's recyclable, making it an environmentally friendly material [87].

Additionally, the applications of paper in the electronics industry have been increasing, with cellulose-based materials being used in capacitors, transistors, batteries, foldable printed circuit boards, sensors, among others [49]. LIG on paper [13] allowed for single-step direct writing of specified patterns of highly conductive graphitic material on this substrate, opening possibilities for expansion of its applications as, for example, a platform for sensing devices.

1.2 Aim and Dissertation Plan

The main goal of this thesis is the development and fabrication of a low-cost LIG-based pH sensor on paper, comprised of laser-scribed flexible electrodes, which can be directly

integrated within wound dressings in order to conveniently monitor wound healing, improve clinical outcome and prevent further complications like WIs and progression into CW status. The device construction will be based on paper substrate, with embedded graphene electrodes, synthesized using LDW technique as pictured in Figure 1.1.

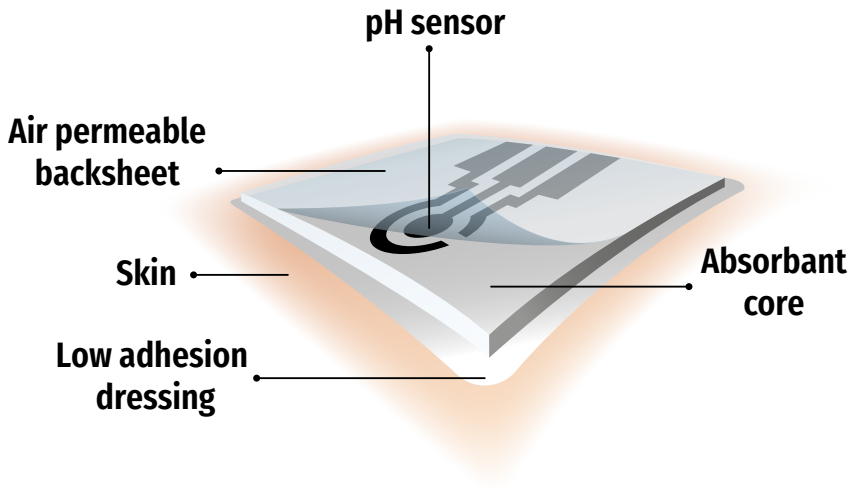

Figure 1.1: Illustration of LIG electrodes for pH biosensor and possible implementation within a conventional wound dressing.

This work will be divided into three stages: first, a systematic study will be conducted in order to optimize the different laser parameters for graphene induction on paper with the best electrical and electrochemical properties; the second and central task of this work will be the fabrication of LIG electrodes using LDW techniques with previously established laser parameters and implementation within a pH sensor; the last stage will be the testing and validation of the pH sensor coupled with the evaluation of a possible prototype implementation.

LIG will be synthesized using a commercial CO_2 laser. Chemical and morphological characterization of the produced graphene electrodes will be carried out by scanning electron microscopy (SEM), energy-dispersive X-ray Spectroscopy (EDS), X-ray photoeletron spectroscopy (XPS) and micro-Raman spectroscopy (MRS) analysis. Electrical inference of the produced LIG samples will be carried out through sheet resistance measurements. Electrochemical characterization of the fabricated sensors will be performed using a portable potentiostat.

CHAPTER 2

THEORETICAL CONCEPTS

This chapter provides the fundamental theoretical concepts for development and research facilitation. These notions will be essential for the conceptualization and production stages of the proposed device as they encompass the explanation for many of its functionalities and components.

2.1 Wound Healing

Wound healing is an essential human and animal biological process responsible for replacing injured tissue with new and healthy tissue, repairing the original function or structure of the damaged site. The regeneration of wounded tissue is achieved by four sequential yet overlapping stages (see Figure 2.1): hemostasis, inflammation, proliferation, and finally, the tissue remodeling phase [27, 94]. In order to accomplish proper healing of wounded tissue, it is imperative that all the stages mentioned above occur at a specific time, duration, and with the right intensity [27, 51].

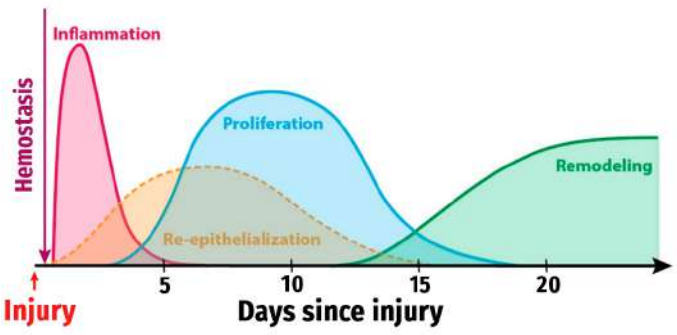

Figure 2.1: Timeline of wound healing process demonstrating phase specificity in time and stage overlap. Adapted from [77].

Within a good healing process, each cellular and physiological event is carried out by specific precursors along the four stages (Figure 2.2):

1. Initially, right after the tissue is damaged, the hemostasis phase promotes vascular constriction and fibrin clot formation. Faced with injury to the skin, the exposed subendothelium, collagen, and tissue factor will promote platelet aggregation. Blood platelets begin to aggregate, degranulate, and the release of pro-inflammatory cytokines and growth factors is induced.

2. After the bleeding is controlled, there is an increase in the affluence of inflammatory cells to the wound site, such as neutrophils, macrophages, and lymphocytes, initializing the inflammatory stage. Neutrophils are responsible for withdrawing invading substances or organisms, removing cellular debris, and providing a good healing environment. Macrophages facilitate phagocytosis during these stages, making hemostasis, and the inflammatory phases last on average 72 hours [82].

3. The proliferative stage is the next to occur and generally overlaps with the previous one. During this period, there is an increase in epithelial proliferation and re-epithelialization associated with a boost in collagen production, angiogenesis, and the renewal of the extracellular matrix by fibroblasts forming the granulation tissue. The proliferative phase may proceed for three to six weeks [82].

4. Remodelling comes about in the last step of wound healing, during which a fine-tuned balance between cellular apoptosis and new cell generation is required. In the course of the remodeling process, there is degradation of the extracellular matrix and maturation of blood vessels and type III collagen into type I collagen [94, 27]. This last step may take up to 9 months to be completed and until the tissue has fully regenerated [82].

Several factors have to be considered in this process since they can interfere with the wounding process. Local factors include oxygenation, infection, a foreign body, and venous sufficiency. Certain systemic factors have to be taken into account that may also help induce the CW status. These are age and gender, sex hormones, stress, ischemia, obesity, certain diseases like diabetes, some medication, alcoholism and smoking, poor nutrition and immunocompromised conditions from cancer, AIDS and radiotherapy [27]. Interference in any healing stage can lead to an impaired regeneration process. Aberrations in wound healing could include excessive remodelling, which leads to hypertrophic scars [82], and, in the case of prolonged and non-healing tissue, it may evolve into CWs [94, 16].

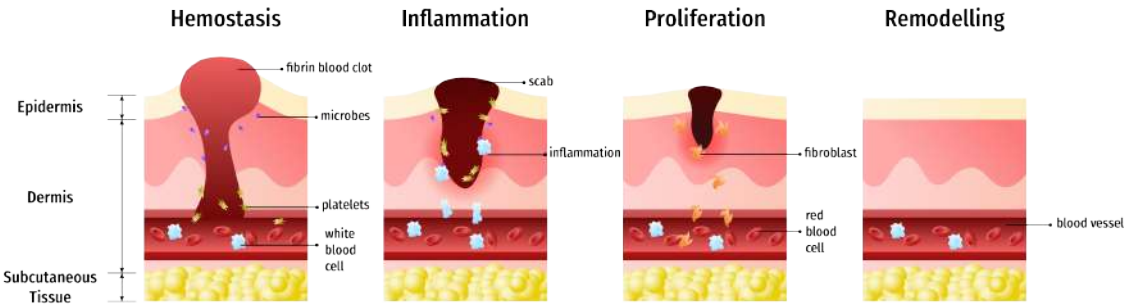

Figure 2.2: Wound healing stages.

2.1.1 Chronic Wounds

The definition of chronic wound (CW) was proposed by Eaglstein and Falanga [16] as a category of wounds that show no prospect or an inability to heal in proper time. This condition encompasses the failure to fully recover damaged tissue's anatomic or functional integrity [77]. In these cases, CWs may result from an acute wound that suffered impaired healing. Non-healing injuries are often characterized by a longer-lasting inflammation stage, some defects in the re-epithelization, and matrix remodeling [17]. Some origins include vascular occlusion, inflammation, pressure necrosis (ulcers), physical agents like heat or radiation, and WI. The most common type of CWs are skin ulcers, diabetic ulcers, and venous ulcers, constituting about 70 % of all CW occurrences [16]. CWs are a common but severe condition and, if not monitored, can lead to complications, the most extreme cases resulting in limb amputation [29].

2.1.2 Wound Infection

As mentioned in Chapter 1, WI is a critical issue in the context of wound care as it is directly linked with CW condition. Once the skin is damaged, the endothelium is exposed, and external microorganisms and particles gain access to the underlying tissue. As these microbes replicate, healing progression may be hindered, and the wound site is classified sequentially as being contaminated, having colonization, becoming a local infection, or critical colonization. With a further increase in pathogens, it may evolve into a more invasive severe infection which is manifested with septicemia [17].

Oftentimes, surgeries may lead to some complications, one of them being SSIs. SSI is an infection that occurs during tissue regeneration following surgical intervention. This complication can be classified as incisional if it occurs at a superficial level or organ space SSI. SSIs are a widespread complication, being the second most common type of nosocomial infections [33].

Bacteria populate all CWs and, at low levels, may even be beneficial to the healing process. However, as the population increases and there are signs of WI, bacteria become very detrimental to wound healing. Studies have found that, in addition to the number

of bacteria and other microbial organisms present, the host's immune system and the number of different species colonizing, their virulence and interspecies interaction are also essential parameters that influence the evolution to WI [17].

2.1.3 Wound Exudate

Wound exudate is generally described as the fluid produced by wounds. Exudate is mainly produced during the inflammatory stage due to the influence of inflammatory precursors like histamine and bradykinin [95]. It is a common factor in acute wounds, and is considered a vital component of the reparation process. However, in non-healing injuries or CWs, wound exudate begins to be a burden and can discomfit the healing process, signaling the presence of infection or other abnormalities [95]. A small amount of exudate in the edges of the wound site coupled with dry exudate on the rest of the surface constitutes a natural barrier to bacteria and other microbial organisms. It is also indicative of healthy tissue regeneration [15]. The composition of this liquid may vary between stages and individuals, but, in general, wound exudate is extremely rich in essential nutrients for epithelial cells, responsible for providing a facile approach of white blood cells to the site. It has a high protein content and a significant concentration of electrolytes and inflammatory components like leukocytes, fibrinogen, and fibrin [15].

The correct amount of wound exudate provides a good hydration level and is vital for proper healing. Excess water may lead to tissue maceration, which is highly detrimental. Some benefits of a moist wound environment over dry include faster recovery, higher epithelization rate, reduced scarring, lower infection rates, pain sensitivity, and enhanced autolytic debris clearance [59, 72]. To assure correct healing, the pH of wound exudate is an important factor to be considered as it influences and reflects the wound environment state.

2.1.4 pH

The pH concept was first defined in the early twentieth century, in Denmark, when studies managed to attain information over the acidic properties of solutions with hydrogen electrodes. The results showed a correlation between hydrogen ion (H^+) concentration and the acidity measurement. The higher the H^+ concentration, the more acid the solution is. This measure of ion concentration and acidic properties was first labeled as the *"Power of Hydrogen"*, hence the pH lettering. pH value is calculated by $-\log_{10}[H^+]$ where $[H^+]$ is the hydrogen ion concentration [30].

In the context of wound healing, as mentioned in Section 1.1, pH has been neglected. Nevertheless, this biomarker is highly indicative of the wound site situation. The hydrogen ion concentration of wound exudate is ever-changing through different healing stages (see Figure 2.3). In the case of an acute wound, pH values tend to be low (4-6) in the earlier inflammation step, rapidly evolving into higher values (7-8) during the following stages and finally returning to baseline acid levels ($\approx$6) during the epithelization phase.

There is no epithelization stage with improper healing, and pH levels tend to stay high (> 7) for an undetermined period, reaching chronic status. The acidic or alkaline state of this fluid is then indicative of wound condition, its phase, and of the presence of WI or other complications [75].

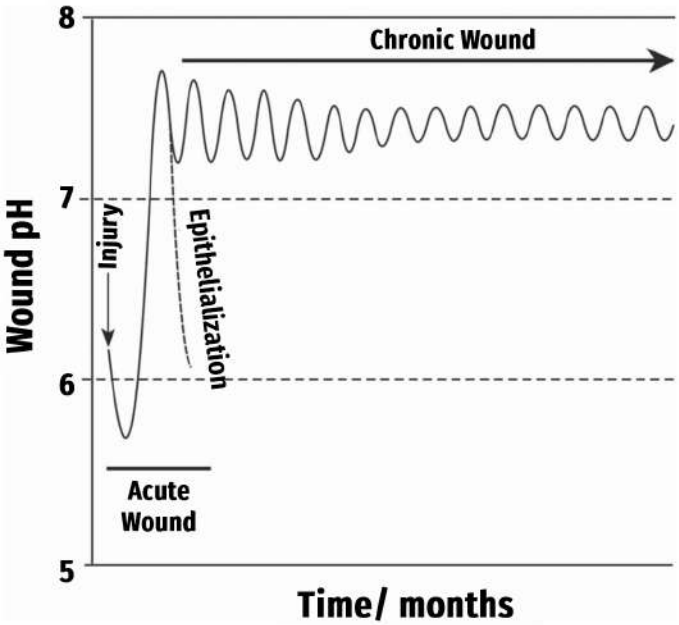

Figure 2.3: pH variation throughout the wound healing process: with acute wounds, pH tends to reach lower values (5-6) in the initial healing phases; in the last stages, it rises above seven and in the epithelialization stage, it reaches values between 6 and 7; in the case of chronic wounds, there is no stabilization of pH levels during the epithelialization stage, and wound pH oscillates between alkaline values (7-8). Adapted from [51].

2.2 Biosensors

Laboratory tests and hospital protocols are traditional ways to analyze and detect specific biomarkers and correctly diagnose many conditions. These procedures frequently require highly specialized professionals, costly equipment, and the patient's presence at the hospital or health facility. Biosensors have emerged to tackle these problems as they promptly enable low-cost and ambulatory diagnosis [1].

A biosensor is a device capable of analyzing specific biochemical components and turning them into an analytically useful signal. These devices are often small, self-contained, and perform biological recognition by direct contact with the transducing component. Biosensors are comprised of two primary components connected in series: a biochemical recognition system termed receptor and a physiochemical transducer [85].

Receptor: The recognition system is the one responsible for providing selectivity to the device. The purpose of this system is to ensure that the device is sensitive to the specific analyte to be measured [85]. It interacts with the specific analyte and generates effects that can be measured by the transducer [39].

Transducer: The transducing segment of biosensors is the system that provides the signal transfer between the recognition system and the electrical domain. Transducers, often referred to as electrodes, sensors, or detectors, are responsible for providing a bidirectional signal transference from non-electrical to electrical, and vice versa [85].

Biosensors can be categorized according to their transducer type, ranging between electrochemical, electronic, optical, piezoelectric, gravimetric, pyroelectric, and magnetic [39, 85]. Within the scope of this dissertation, we will focus on electrochemical biosensors.

2.2.1 Electrochemical Biosensors

An electrochemical biosensor is a sensing device characterized by an electrochemical transducer. These transducers are often referred to as chemically-modified electrodes [85] because its conducting surface is generally covered with enzymes able to provide electroactive substances to be detected by the transducer. In these cases, the analyte will act as the substrate for the deployed enzyme [66]. As of today, electrochemical biosensors are the most common wearable devices as they provide unique advantages like sensor miniaturization, high sensitivity, and direct measurement [97]. Within electrochemical biosensors, multiple electrochemical transducers can be employed depending on the operating principle, ranging from potentiometric, amperometric, impedimetric, or voltammetric [66].

2.2.1.1 Electrochemistry Principles

In order to understand the working principle of electrochemical biosensors, general insight on the basics of electrochemistry must be presented. Electrochemistry is a field of study focused on the interpretation of electrochemical reactions. These are processes involving the transfer of charges at an electrode/solution interface [101] which can be described by the following equation:

$$O(aq) + ne^- \rightleftharpoons R^{n-}(aq) \tag{2.1}$$

Where O and R refer to the oxidized and reduced species, respectively, of a redox couple in an aqueous solution. Equation 2.1 describes the electronic movement of n charges across the interface between an electrode, the source of electrons, and an aqueous (aq) solution. It is worth noting that this phenomenon only occurs once an electrode is placed within the solution, acting as a source or destination for traveling charges [6].

These particles traverse the interfacial region between the electrode and solution, which ultimately creates a potential difference at this site. To measure the potential difference in equilibrium, a second electrode must be placed inside the solution that is able to maintain a fixed potential at its electrode/solution interface, acting as a reference electrode (RE). The RE can be fabricated from a variety of materials, and most commonly is a standard hydrogen electrode (SHE), or saturated calomel electrode (SCE), but Ag/AgCl is also widely used [6]. The potential is then measured in relation to the constant potential at the RE.

The analytical method of describing the correlation between potential measurements and the concentration of the involved redox species at the surface of the electrode was described by Walther Nernst:

$$E = E^0 + \frac{RT}{nF} \ln \frac{[O]}{[R]} \tag{2.2}$$

Where E refers to the measured potential between the working electrode (WE) and RE, also termed electromotive force (EMF), E^0 is the standard electrode potential, R is the universal gas constant (8.314 J K^{-1} mol^{-1}), T is the temperature in Kelvin, F stands for the Faraday constant (96485.33 C mol^{-1}). The *Nernst Equation* (Equation 2.2) became a tenet in the electrochemistry world allowing for the calculation of EMF under equilibrium circumstances and becoming the basis of potentiometric sensors [101].

Despite equilibrium electrochemistry being a key area within this field of study, dynamic electrochemistry has more applications, namely in the sensing devices industry [6]. The most common setup for dynamic electrochemical experiments requires an extra electrode, totaling three, one WE, one RE as previously described, and one counter electrode (CE) or auxiliary electrode (AE) whose function is to close the circuit and serve as a pathway for travelling electrons within the solution. The CE should have a high surface area and must be of a non-reactive material like platinum or carbon [6]. Figure 2.4 depicts the general process of a dynamic electrochemical reaction, where initially,

the reactant, in this case, the oxidized species (O), diffuses from the bulk solution to the electrode/solution interface, with a process deemed mass transport. Then, a potential difference distinct from the equilibrium is applied to the system, inducing charge transfer between the electrode surface and solution. Finally, traveling electrons lead to the electrolysis of the oxidized molecules. The product of this reaction is termed the reduced species (R) and is diffused into the bulk solution via mass transfer [6].

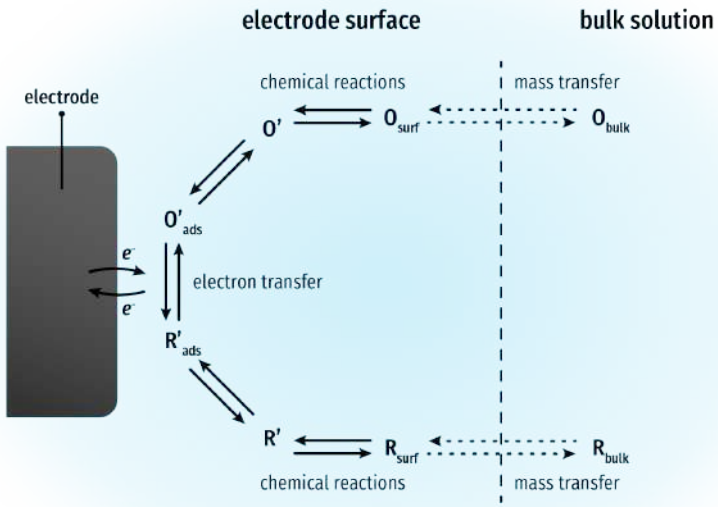

Figure 2.4: Standard electrochemical reaction mechanism. O and R are the oxidized and reduced forms of a electroactive species. These can be found initially in the bulk solution (O_{bulk} and R_{bulk}), from there, diffusion takes place towards the electrode/solution interface through mass transport (O_{surf} and R_{surf}). Chemical reactions may occur (O' and R') before the species contact with the electrode surface (O'_{ads} and R'_{ads}), where electron transfer takes place. Adapted from [6].

Note that this process may occur both ways, depending on the applied potential. From Figure 2.4 one can verify that the current produced at the electrodes is dependent on mass transfer, which is tied to subsequent processes like chemical reactions, adsorption/desorption, and the heterogeneous electron transfer rate (k^0) of the system [6].

2.2.1.2 Cyclic Voltammetry

Cyclic voltammetry (CV) is one of the most popular electrochemistry tools, being acclaimed as one of the go-to methods for electrode kinetic measurements [56]. In recent years, CV has been extensively applied in the qualitative study of electrochemical reactions by allowing the monitoring of the thermodynamics of specific redox couples reactions, and the kinetics of heterogeneous electron-transfer processes as well as other processes like adsorption/desorption [6].

Considering a three-electrode system previously described in Section 2.2.1.1, CV consists in linearly scanning the potential applied to the WE from a preselected initial potential E_1 to a desired limit potential E_2 where the direction of the scan is reversed (Figure 2.5a) until it reaches E_1 again, completing the cycle. E_2 is commonly referred to as the switching potential [45]. Upon reaching the switching potential, if the scan is stopped, the procedure is called linear sweep voltammetry. According to the user's input, the procedure can also be limited to a single cycle or continue the scanning of the potential for multiple cycles. The rate at which the potential is swept is termed voltammetric scan rate (V s^{-1}) and corresponds to the slope of the potential function presented in Figure 2.5a [6].

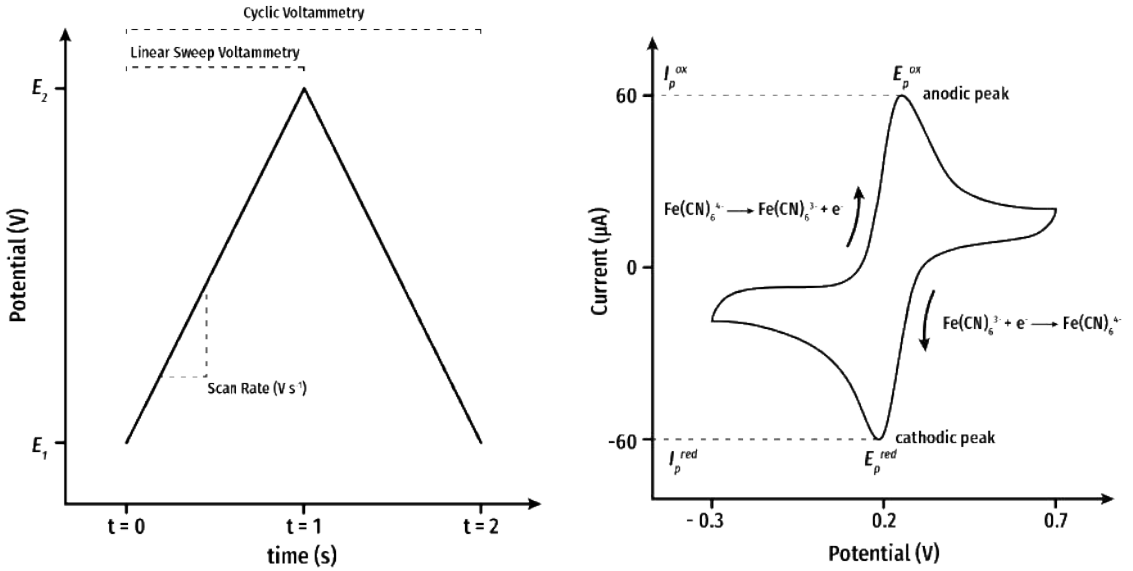

(a) (b)

Figure 2.5: (a) Potential profile applied during cyclic voltammetry and linear sweep voltammetry scans. (b) Current plot of cyclic voltammetry scan for ferri-ferrocyanide redox probe, depicting the characteristic anodic and cathodic current peaks (I_p^{ox} and I_p^{red}), at specific potentials during the cycle (E_p^{ox} and E_p^{red}).

As displayed in Figure 2.5b, the current resulting from the applied potential is measured using a potentiostat and is plotted in a current (I) vs. applied potential/voltage (E) graphic designated as cyclic voltammogram [45]. The x-axis represents the potential energy (in *volts*) imposed on the system throughout the cycles. At the same time, the y-axis is a scale for the electrode response, representing the resulting current (in *amperes*) [19].

CV can be performed against a multitude of electroactive species, but one of the standard redox probes used in electrochemical studies is the ferri-ferrocyanide redox couple $Fe(CN)_6^{3-} + e^- \rightleftharpoons Fe(CN)_6^{4-}$ [45, 10, 6] characterized by its well-defined oxidation and reduction current peaks shown in Figure 2.5b.

Although there are several voltammetric data plotting conventions, this work will

only feature CV data according to the International Union of Pure and Applied Chemistry (IUPAC) convention where positive applied potentials are displayed along the positive x-axis direction and cathodic currents, resulting from species reductions, are negative [19, 6]. Figure 2.6 displays the difference between the classical (widely adopted in the USA) and the IUPAC conventions for CV plots.

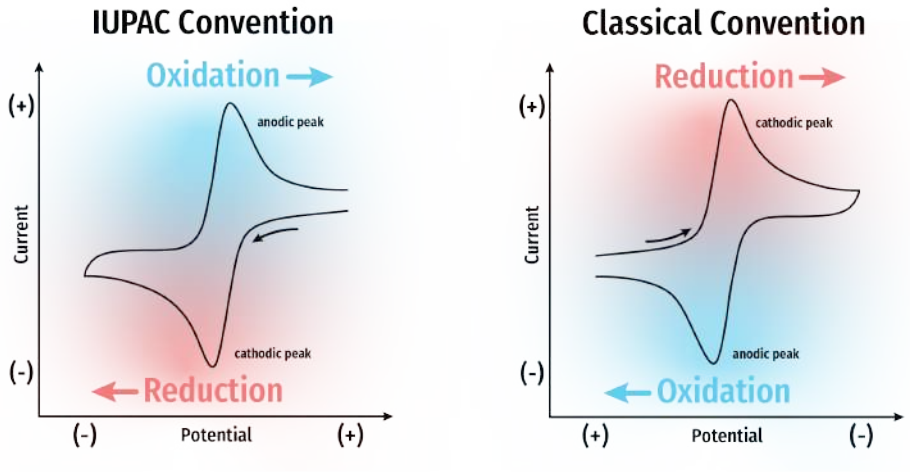

Figure 2.6: IUPAC vs. Polarographic (Classical) conventions for cyclic voltammograms.

Voltammogram analysis mainly departs from the monitoring of current peak heights (I_p) and location, that is, the potential at which the peak is prominent (E_p). These can give insight into electrode's performance, more specifically of the k^0 which dictates whether a system is electrochemically reversible, quasi-reversible, or irreversible [6].

In a reversible system, the electrode kinetics are extremely fast and surpass the mass transport rate (Figure 2.7a). This allows for the Nernstian equilibrium (Equation 2.2) to be applied through the voltammogram at any given potential. Quasi-reversible systems show kinetics that are slower or close to mass transport rates (Figure 2.7b). In contrast, irreversible electrode kinetics are much slower and far from mass transport rates (Figure 2.7c) [6].

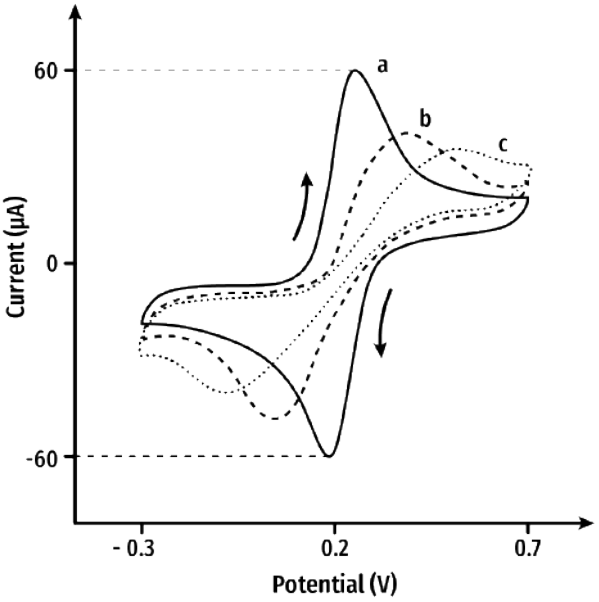

Figure 2.7: Cyclic voltammograms for different electrode kinetics: (a) reversible (b) quasi-reversible (c) irreversible electron-transfer process.

It is possible to extrapolate the reversibility of an electrochemical system by analyzing peak-to-peak separation $\Delta E = (E_p^{ox} - E_p^{red})$. If ΔE is below 57/n mV, at a temperature of 298 K, for a one-electron exchange reaction (n=1), the process is said to be reversible [6, 19, 34].

The relationship between peak current (I_p) and scan rate is described by the Randles-Ševćik equation [22]:

$$I_p^{rev} = \pm 0.446 nFA_e C\sqrt{\frac{nFD\upsilon}{RT}} \tag{2.3}$$

$$I_p^{quasi} = \pm 0.436 nFA_e C\sqrt{\frac{nFD\upsilon}{RT}} \tag{2.4}$$

$$I_p^{irrev} = \pm 0.496\sqrt{\alpha n'}nFA_e C\sqrt{\frac{nFD\upsilon}{RT}} \tag{2.5}$$

Where Equations 2.3, 2.4, and 2.5 refer to the Randles-Ševćik relation for reversible, quasi-reversible, and irreversible electrochemical processes, respectively. The ± sign refers to the oxidation or reductive stage of the reaction depending on the peak being analyzed (positive for the forward scan peak and negative for the reverse scan peak). I_p is the peak current (in A), υ is the applied scan rate (V s^{-1}), A_e is the electrode's electroactive area (cm^2), D is the diffusion coefficient for the electroactive species (cm^2 s^{-1}), n is the number of electrons transferred per molecule in the electrochemical reaction, n' is the number of electrons transferred per mole before the rate determining step, C is the bulk concentration of the analyte (mol cm^{-3}), and α is the transfer coefficient [22].

The α parameter is usually considered to be 0.5 but can be more accurately defined by performing a voltammetric study (Figure 2.8) at multiple scan rates and applying the Laviron equation [10]:

$$\alpha = \frac{\delta_{ap}}{\delta_{ap} - \delta_{cp}} \tag{2.6}$$

Where δ_{ap}, and δ_{cp} represent the anodic and cathodic slopes of the linear portions of I_p^{an} and I_p^{cat} (anodic and cathodic peak currents) vs. the common logarithm of the applied scan rates ($log(\upsilon)$) plots [10].

Voltammetric scan rate studies can be helpful to acquire information about the limiting factors of an electrochemical process. Diffusion-controlled electrochemical reactions involve freely diffusing redox species. If reversible (Figure 2.8a), these are characterized by a linear response of peak currents (I_p) vs. square root of the scan rates ($\upsilon^{\frac{1}{2}}$) plots, and no ΔE_p shift with scan rate. Deviations from linearity in these plots may indicate that the process is quasi-reversible or that the electron transfer occurs in electrode-adsorbed species. Peak separation (ΔE) is a good tool to distinguish between the two cases since for quasi-reversible behavior, ΔE_p shifts with scan rate (Figure 2.8b), while with electrode-adsorbed species, no ΔE_p is observed, in which case the process is said to be surface-controlled. In surface-controlled processes, linearity is displayed in I_p vs. υ plots [19].

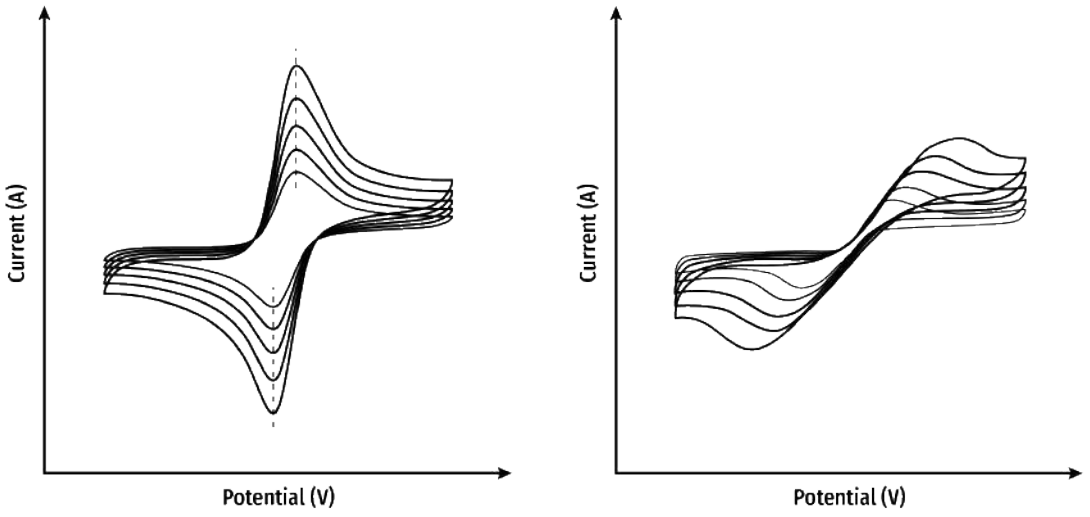

(a) (b)

Figure 2.8: Voltammetric scan rate study plots for different reversibility processes:(a) reversible (b) quasi-reversible/irreversible.

The k^0 of diffusion-controlled processes can be deduced from CV analysis using the Nicholson method.

$$\psi = k^0 \left(\frac{D_o}{D_r}\right)^{\frac{\alpha}{2}} \sqrt{\frac{RT}{\pi n F D_o \upsilon}} \tag{2.7}$$

Where ψ is the dimensionless kinetic parameter, k^0 is the heterogeneous electron transfer rate (cm s^{-1}), D_o and D_r are the diffusion coefficients of the oxidized and reduced form of the electroactive species, respectively, and υ is the scan rate (in V s^{-1}) [56].

ψ is also an indicator of the system's reversibility, with values of $\psi = 20$ occurring in reversible systems, while $\psi \leq 7$ indicates the process is quasi-reversible [71].

Assuming D_o and D_r to be approximately equal, and α to be ≈0.5, Equation 2.7 can be simplified to:

$$\psi = k^0 \sqrt{\frac{RT}{\pi n F D_o \upsilon}} \tag{2.8}$$

or

$$\psi = k^0 C \upsilon^{-\frac{1}{2}} \tag{2.9}$$

Where C is a constant derived from the simplification of $(RT/\pi n F D_o)^{\frac{1}{2}}$. In addition to the Nicholson method, in 2004, Lavagnini et al. [40] proposed another ΔE_p vs. υ correlation which allowed for a more practical way of calculating the kinetic parameter ψ:

$$\psi = \frac{(-0.6288 + 0.021X)}{1 - 0.017X} \tag{2.10}$$

Where $X = \Delta E_p \times n$, n being the number of electrons involved in the reaction, and ΔE_p is expressed in millivolts. Using Equations 2.7 and 2.10, one can readily extrapolate the k^0 value from the slope of the ψ vs. $C\upsilon^{-\frac{1}{2}}$ plots.

Although very useful, the Nicholson method has its limitations since it can only be applied to reversible or quasi-reversible, i.e. processes that show $\Delta E_p \times n \leq 200$ mV [40]. To bridge this gap, Klingler and Kochi devised another correlation fitting for higher ΔE_p values [34]:

$$k^0 = 2.18 \left(\frac{D_o \alpha n \upsilon F}{RT}\right)^{\frac{1}{2}} exp\left(-\frac{\alpha^2 n F}{RT} \Delta E_p\right) \tag{2.11}$$

Which can be rearranged to:

$$\psi = 2.18 \left(\frac{\alpha}{\pi}\right)^{\frac{1}{2}} exp\left(-\frac{\alpha^2 n F}{RT} \Delta E_p\right) \tag{2.12}$$

Equations 2.11 , and 2.12 tackle Nicholson's method limitations, giving us the complementing tool for electrochemical analysis outside Equations' 2.7, and 2.8 range for ψ values.

All the theoretical concepts and mathematical correlations presented above have proven to be essential in the electrochemical characterization of biosensors and will be extensively applied in Chapter 5.

2.2.2 Wearable and Flexible Biosensors

Wearable sensors have been the target of massive research in the past decade. As the world's population increases and healthcare costs continue rising, there is a growing need for these personalized health monitoring devices. These sensors open the possibility to perform diagnosis through biochemical sampling without hospital interference, conveniently and non-invasively. They are lightweight, low-cost, and have high flexibility, conformability, and stretchability due to the emergence of flexible electronics giving them also extreme versatility. Moreover, many possible applications are being explored, and as of recent years, flexible electronics have been used in physiological monitoring, robotics, smart displays, and energy storage. On the other hand, wearable sensors were developed to provide continuous physiological monitoring of an array of analytes, namely in tears, saliva, sweat, blood, breath, interstitial fluid, and in wounds for wound monitoring (see Figure 2.9) [97]. In the context of wound care, this state-of-the-art technology has been incorporated in wound dressings and bandages to develop smart bandages [9].

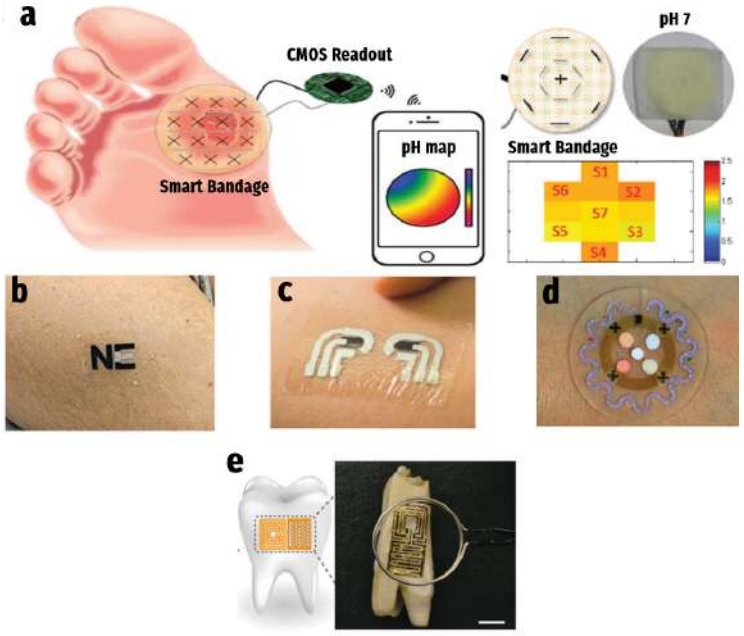

Figure 2.9: State-of-the-art wearable and flexible sensors for monitoring different biological analytes: (a) smart bandage for wound pH analysis using pH-sensitive polyaniline (PANI) coated threads. CMOS wireless readout and 2D mapping of pH levels were incorporated; (b) epidermal tattoo, sweat-based biosensor for local monitoring of lactate, pH, and other analytes; (c) printed tattoo-based interstitial fluid glucose sensor; (d) stretchable microfluidic patch for sweat routing through serpentine channels and reservoir with multiplexed colorimetric sensing system; (e) saliva sensor on tooth enamel with graphene-based nanosensors. Bacteria quantification was performed based on electrical resistance variation. Adapted from [97].

2.3 Graphene

Graphene is a carbon-based material consisting of a single sheet of carbon atoms densely packed into a two-dimensional (2D) honeycomb network given by its benzene-ring structure [24, 58, 57], as illustrated in Figure 2.10a. Each of the atoms in this carbon allotrope is sp^2 hybridized and tightly bonded to three other carbon atoms [86]. As of today, it is the world's thinnest and strongest known material [23]. Graphene is known for its outstanding electrical and mechanical properties, which granted it the "miracle material" epithet by the scientific community [58].

This single atomic plane of graphite is the first 2D atomic crystal structure to be discovered. This seems to defy several principles of the crystallization process since it implies the subjection to high-temperature environments and thermal variability, which would be greatly detrimental to one-dimensional (1D) and 2D atomic structures forcing them to morph into more stable three-dimensional (3D) structures [23]. Albeit, graphene can be found in many shapes, either wrapped into a zero-dimensional (0D) fullerenes (Figure 2.10b), rolled up into 1D nanotubes (Figure 2.10c) or as graphite formed by several graphene layers stacked up in the 3D space (Figure 2.10d) [24].

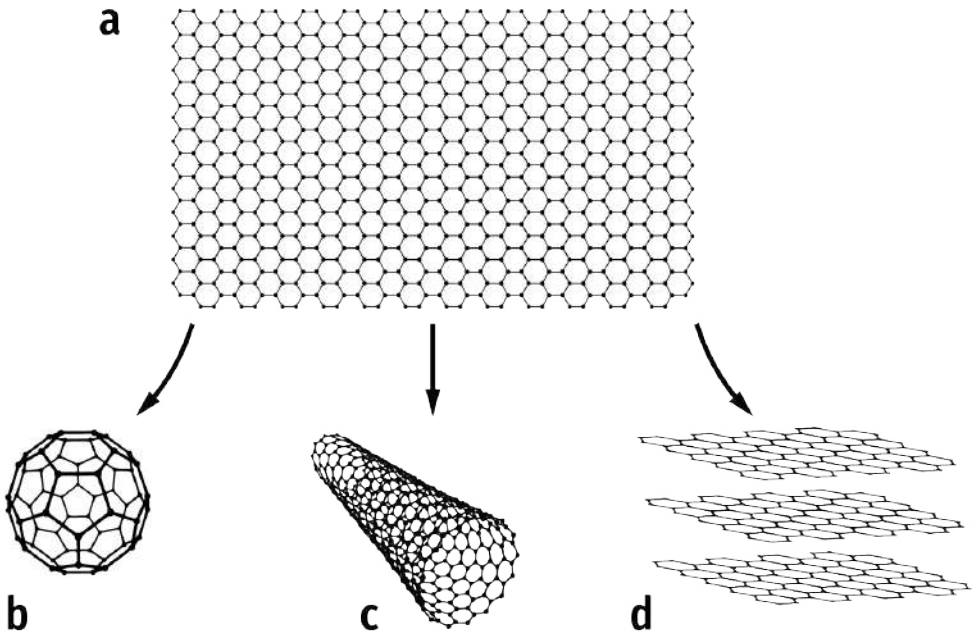

Figure 2.10: Representation of graphene (a) as a 2D sheet of carbon atom; (b) rolled up into a 0D fullerenes; (c) as a 1D nanotube; (c) stacked into a 3D structure, forming graphite.

Many graphene properties, like its mechanical stiffness, elasticity, thermal and electrical conductivity, have surpassed existing materials and have even reached theoretical

limits [58]. This material presents the ability to hold current densities a million times higher than copper and is entirely impervious to gases [58, 23].

The extreme properties of graphene grant it multiple applications within research fields like nanotechnology, biomedical engineering, material science physics, and green chemistry [86]. Many use cases have been studied in flexible and wearable electronics, photonics, biosensors, among others [69, 58].

Although the existence of one atom thick 2D crystalline structures was known by science, it was not until 2004 that Novoselov and colleagues [57] were able to isolate it through micromechanical exfoliation. Nonetheless, other fabrication techniques (Table 2.1) have been developed since then, ranging from chemical exfoliation, chemical vapour deposition (CVD), synthesis on silicon carbide (SiC), among others [58]. These traditional routes either require high-temperature processing or multi-stepped chemical synthesis, significantly hampering this material's commercial potential. Laser induction of graphene through LDW is a recent technique that managed to tackle these challenges by allowing a single-step, scalable and straightforward method of graphene production [42].

2.4 Laser-Direct Writing

LDW is the process of engraving certain patterns onto a surface or volume through a serial or "spot-by-spot" laser beaming technique. The patterning procedure is controlled by computer software and performed by a robotic system. Contrary to traditional methods like lithography, stamping or directed self-assembly, LDW does not require the use of masks, pattern stencils, a complex clean environment, or even direct contact with the device [3, 73]. These advantages propelled the rise of LDW as a low-cost, cleaner, and faster alternative to the production of electrodes on flexible substrates with high resolution. Its high versatility enabled the creation of new structures otherwise impossible to be achieved [73].

Although there are several iterations of LDW technique, these devices are essentially made up of a laser source, a substrate mounting system, and a beam delivery system, as shown in Figure 2.11. The working principle of this process is based on the emission of an ultra-fast and focused laser beam that leads to multiphoton absorption by the substrate. The effects of laser irradiation may vary between substrate materials and, for example, in the case of photopolymers (light-activated resin), it results in the polymerization with extremely high resolution (less than 100 nm) [76]. Patterning is then achieved either by moving the high-powered beam through the target surface or by maintaining a fixed beam and moving the substrate accordingly (Figure 2.11), making it possible to construct both 2D and 3D structures [3].

Amongst the numerous applications of LDW, this procedure has been contributing to astonishing advances in the development of new technologies, like supercapacitors [18]. Furthermore, in the field of nanotechnology, it has been distinguished in the production

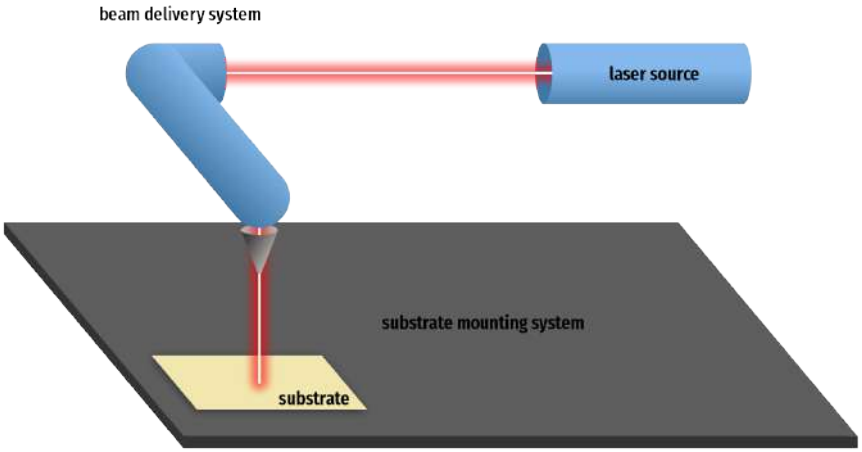

Figure 2.11: Illustration of the basic components of a LDW machine. The beam delivery or substrate mounting systems' motion is controlled by computer software during laser irradiation, designing and manufacturing the desired product.

of complex 3D nanostructures, photonics, micro-optics, and microfluidics. In the field of biomedical engineering, the development of implants and scaffolds for tissue engineering is highlighted [76].

Recently, there have been significant advances in the use of LDW as a means to produce graphene sensors, capable of monitoring several physiological markers, by laser irradiation of carbon-based substrates resulting in the induction of graphene-like conductive structures [44, 9, 69, 5].

2.4.1 Laser-Induced Graphene

In 2014, Lin et al. [42] proceeded with the irradiation of commercial PI and polyetherimide (PEI) thin films with a CO_2 infrared laser. The ablation of the substrate resulted in the creation of carbonized graphitic/graphenic structures. These findings were further analyzed and characterized as being graphene stacked structures, validating LDW as a new graphene synthesis technique with the resulting product being labeled laser-induced graphene (LIG). The resulting porous graphene from LDW processing showed resistance values as low as 15 Ω sq^{-1}.

LIG is a product of the LDW technique and, therefore, it is formed by the previously mentioned photothermal process of irradiating the target polymer surface with a powerful and precise laser beam (see Section 2.4). Beam energy is absorbed and induces vibrations in the substrate's molecular structure, resulting in extreme temperatures at these sites (>2500 °C). These temperatures are capable of breaking C-O, C=O, and C-N bonds, releasing gases like CO_2, CO, HCN, and C_2H_2. In addition to this, this process also

induces the sp^2 hybridization of carbon atoms needed in C-C bonds that shape graphene's carbon lattice structure [73, 42] (see Figure 2.12).

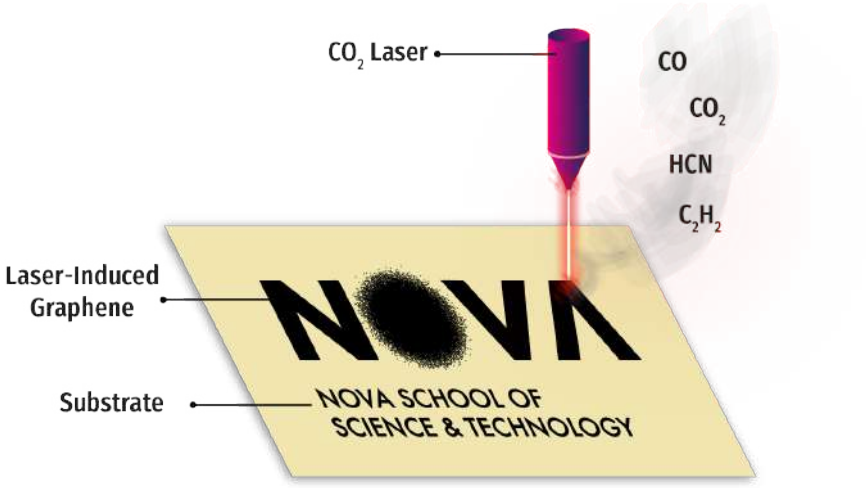

Figure 2.12: Illustration of laser-induced graphene formation mechanism.

Recently, LIG has been a hot research topic for its remarkable properties, being very scalable and cost-effective [42]. Research has focused on developing new viable substrates for LIG production to increase its cost-effectiveness and commercial potential. In 2017, Ye et al. [99] managed to produce LIG from wood samples, presenting low electrical resistance levels of under 10 Ω sq^{-1}. Many polymers like PEI, polybenzimidazole (PBI), epoxy, among others, have proven to be suitable substrates for LIG [69].

In a more recent study, Chyan et al. [13] achieved impressive results by being able to obtain patterned graphene by LDW the surface of renewable carbon precursors like food, cloth, and paper. This was achieved in two steps: first turning the organic material into amorphous carbon with laser irradiation, then converting it to graphene by subsequent lasing scans. Single-step conversion of carbon precursors to graphene was also achieved by lasing at defocused heights. Furthermore, Chyan's team [13] demonstrated that for the same level of pulses per inch (PPI) a defocused laser beam increased the spot size of each pulse resulting in overlapping pulses while lasing at the focal point showed no overlapping (see Figure 2.13). The overlapped spots were equivalent to multiple laser exposures and resulted in single-step/direct formation of LIG.

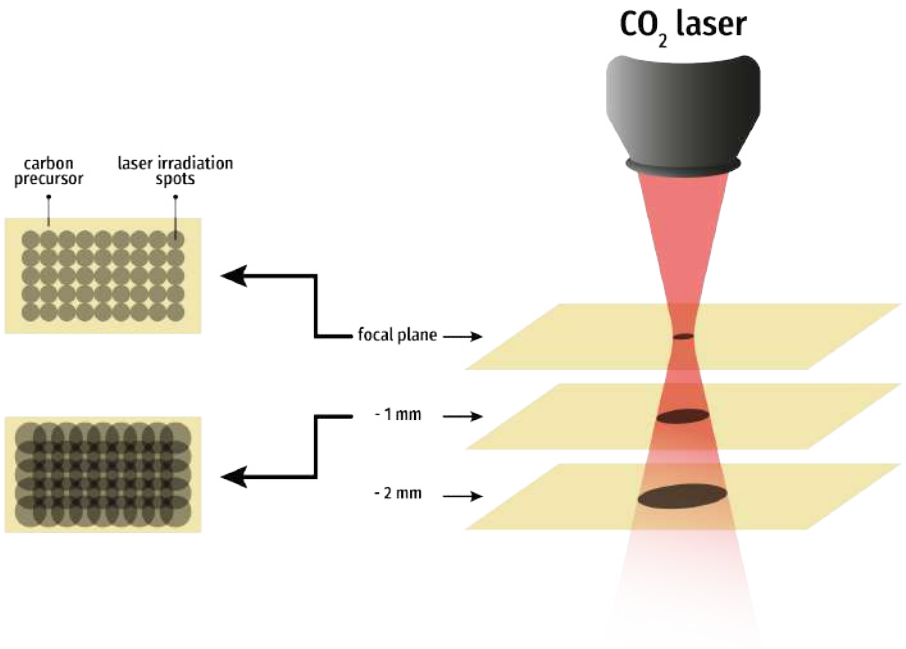

Figure 2.13: Diagram illustrating the effect laser defocusing has on spot size: laser spot size increases as defocusing increases, resulting in greater overlap of laser pulses inducing LIG in a single scan.

This technique has opened new horizons, allowing the incorporation into a wide range of devices such as supercapacitors. Additionally, LIG has taken part in the development of nanomaterials and nanodevices [99], optical sensors [73, 2]. It has also boosted the growth of stretchable and wearable [9, 69, 2, 5] and even edible electronics [13].

Micromechanical exfoliation, CVD, liquid-phase exfoliation, and graphene oxide reduction are some alternatives to the previously discussed method. When compared to others, laser scribing has the advantage of being highly programmable and fine-tunable, covering large surface areas, and being a very low-cost technique. Albeit, it has its cons, like the number of defects produced, its roughness, and the fact that it only results in multilayered graphene. In Table 2.1, multiple graphene synthesis techniques are presented with their respective advantages and weaknesses. Furthermore, different applications of these methods are described [69].

Table 2.1: Comparison between multiple graphene synthesis techniques. Adapted from [69].

Method	Advantage	Weakness	Application
Micromechanical exfoliation	Easy, high quality	Micrometer level, low efficiency	Basic mechanism research, high sensitivity sensor
CVD	Large area, controllable number of layers, high quality	High cost, need for transfer	Transistor, photodetector, transparent electrode, gas sensor, etc.
Liquid-phase exfoliation	Large quantity	Organic solvent	Transistor, Electrochemical sensor, Energy storage, and conversion, etc.
Graphene oxide reduction	Large quantity, aqueous solvent	Oxygen residues with functional groups	Mechanical sensor, transparent electrode, Energy storage, etc.
LIG	Programmable, large area, low cost	Multilayer, a high number of defects, rough	Mechanical sensor, energy storage, bioelectronics, electrochemical sensor, etc.
3D graphene	High strength, porous structure	Hard to pattern, a high number of defects, rough	Energy storage and conversion, gas and mechanical sensor, pollution treatment, etc.

2.5 Paper

As described in the contextualization of this project (Section 1.1), amongst the many available carbon precursors for LIG fabrication paper is the cheapest and widely available, making it a great candidate for LIG-based, low-cost and ecologic sensors fabrication.

Paper is usually a thin sheet material made by drying out a solution containing cellulose fibers, spreading, pressing and heating them into thin sheets. A dilute suspension of cellulosic fibers, named the pulp, is extracted from wood or other vegetable sources either through mechanical, thermomechanical, or chemical processes. Mechanical processing is usually cheaper and is generally referred to as wood-containing. In contrast, chemical processing is called wood-free since the cellulose fibers are separated by cooking, resulting in longer cellulose fibers and the removal of lignin, a component of paper that turns it yellow and more fragile over time [87]. Cellulose ($[C_6H_{10}O_5]_n$) is an organic compound and the main component of paper, forming long chains that make up its fibers, as seen in Figure 2.14. Hydrogen bonds between hydroxyl groups hold these fibers together

[87]. Cellulose is the most abundant organic polymer on Earth and the main structural component in plants, and some algae, constituting the cell walls [41].

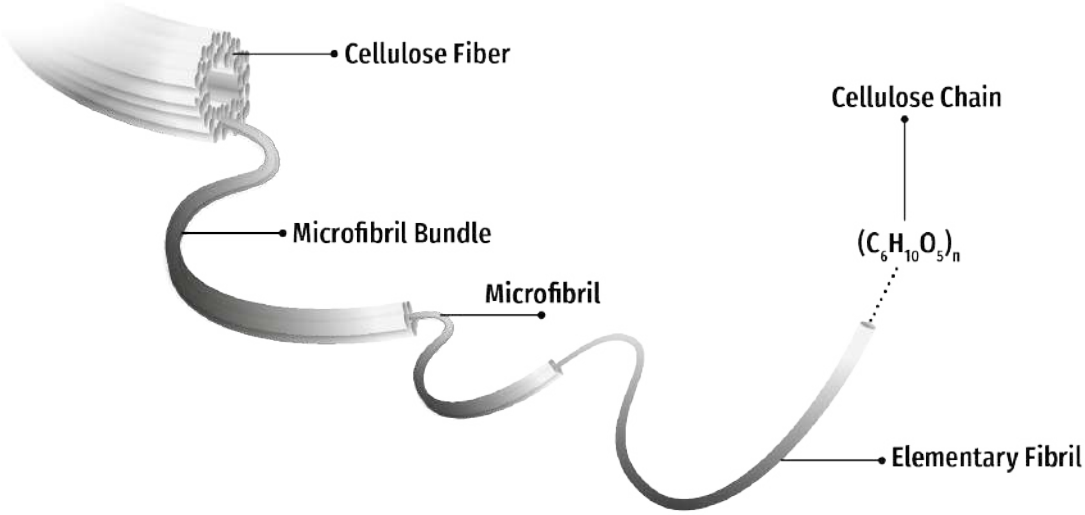

Figure 2.14: Structural composition of cellulose fibers.

Chapter 3

State-of-the-art

This chapter aims to provide a brief literature review on the field of study relevant to the present work. An overview is provided tackling several recently developed LIG technologies on different substrates for electrochemical applications, with the primary focus being pH-sensing devices on paper and other low-cost platforms.

3.1 Gold Standard of pH-sensing Devices

In recent years, the discovery of LIG and its exceptional electrical and mechanical properties coupled with the boost in wearable technology and flexible electronics development have propelled the expansion of wound monitoring devices that aim to improve wound care and outcome prediction by monitoring of multiple analytes. The research was focused on devices with pH as the monitoring target.

Concerning research on wound-monitoring devices, as discussed in Section 1.1, there has been much less attention given to pH as a target analyte. Despite this, studies show that pH is an essential and promising biomarker when it comes to wound condition assessment [75, 9, 67]. Moreover, by performing a simple search query at *PubMed* database with "pH AND wound monitoring AND (sensor OR biosensor)" results provide evidence of the rapidly growing trend and awareness of this biotechnological advancement opportunity, as seen in Figure 3.1.

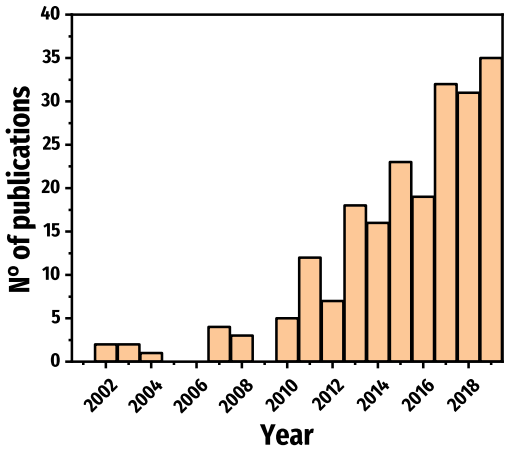

Figure 3.1: Number of search results on *PubMed* database for the "pH AND wound monitoring AND (sensor OR biosensor)" search query.

The glass electrode (Figure 3.2), is nowadays considered to be the gold standard for pH-monitoring devices. This system is made up of an inner Ag/AgCl RE separated by a glass membrane from another Ag/AgCl electrode. Both electrodes are immersed in a stable pH solution of known pH, the latter is enclosed within a glass bulb that's in contact with the unknown pH solution. The solution ions are adsorbed to the glass membrane and a potential difference is generated and measurable across this surface against the RE potential. Despite being highly reliable devices, pH-meters suffer from the need of frequent calibrations, and being fragile due to its glass composition [93]. Some of these drawbacks are bridged with electrochemical sensors, namely with potentiometric and voltammetric, which are the most common approaches and the focus of this study [93].

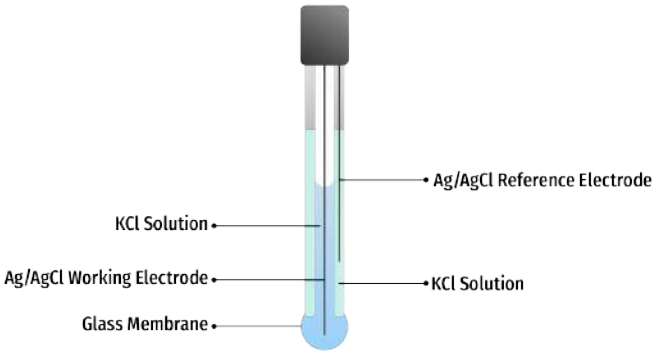

Figure 3.2: Schematic representation of a glass electrode and its components.

3.2 Potentiometric pH-sensing Devices

The potentiometric method is the most common within electrochemical pH sensing devices as it is a very straightforward technique. The operating principle is based on the measurement of the potential difference between two electrodes, one RE, the most widely used being an Ag/AgCl-based electrode since it has a very stable potential profile and is environmentally friendly, and one WE that can be made up of a variety of materials, from metal oxides to different conducting polymers [63].

Many applications have been explored for these potentiometric pH sensors, ranging from agriculture, and water quality management, to the healthcare field [63]. In 2014, Guinovart et al. [26] managed to construct a potentiometric pH sensor for wound monitoring based on screen-printed electrodes incorporated onto commercial bandages. The WE was established through carbon paste screen-printing onto a commercial wound dressing as the substrate and was functionalized with electropolymerized PANI as the conducting polymer for pH sensing (Figure 3.3b). A potentiometric approach was employed, resulting in a Nernstian response within a pH range of 5.5 to 8 with a sensitivity of 59.2 mV pH^{-1}.

More recently, significant advances were made when in 2017, Punjiya et al. [68] managed to develop a smart bandage capable of continuously monitoring pH within CWs using a potentiometric approach. The sensor was fabricated with pH-sensitive carbon-coated cotton threads modified with PANI and Ag/AgCl-coated threads that worked as the reference electrodes. The device encompassed custom complementary metal–oxide–semiconductor readout electronics attached to the pH sensor for wireless monitoring and data transmission. 2D mapping was achieved, and the device exhibited 54 mV pH^{-1} sensitivity (see Figure 2.9a).

Other approaches have been made to tackle the CW pH monitoring goal while having cost-effectiveness in mind. In 2018, Pal et al. [60] were able to develop a smart bandage by integrating a paper-based biosensor within commercial bandages. The paper-based sensor was achieved by stencil printing PANI-based solution and Ag/AgCl conductive ink onto the previously treated Whatman paper substrate (Figure 3.3a). The device was designed to monitor pH status in CW and detect pressure ulcers by measuring changes in impedance across the two electrodes. Pal's team also managed to fabricate a wearable potentiostat that attaches to the smart bandage and can wirelessly report wound status while being extremely lightweight (8 g), inexpensive (around 18 $), flexible, breathable, easy to apply, and disposable by burning (in the case of the paper sensor). Furthermore, this device was tested in an *in vivo* mouse model and was able to detect pressure ulcers prior to the formation of damaged tissue.

2018 saw significant advances with the work of the Xuan team [96] who managed to devise a flexible electrochemical pH sensor based on LIG, a novel fabrication technique that will be a crucial component in the construction of the device presented in this thesis. The pH sensor was based on a potentiometric method having two electrodes, the WE was

coated with a pH-sensitive PANI membrane on top of the LIG layer, and the potential drift was measured against an Ag/AgCl RE. The electrodes were scribed on PI and then transferred to a flexible and stretchable substrate made from a mixture of silver nanowires and a silicon base (PDMS). The sensor displayed good sensitivity with 66 mV pH^{-1} over a 4 to 7 pH range.

In 2019, the Park team [63] developed a simple, low-cost, potentiometric pH sensor based on the screen-printing technique. The system had a two-electrode configuration, an Ag/AgCl RE and a WE established by screen-printing carbon paste onto a PET substrate. The WE was modified with a PANI nanofiber array, which improved pH sensitivity (Figure 3.3c). The device showed a good pH sensitivity value of 62.4 mV pH^{-1}, 97.9 % repeatability, 12.8 s response time, and stability of 3.0 mV h^{-1} over a 3.9 to 10.1 pH range. Additional tests were made by monitoring milk spoilage compared to the measurements of a commercial pH-meter, and flexibility was tested by monitoring pH on the curved surface of an apple.

Vivaldi et al. [92] devised a graphene-based potentiometric pH sensor in 2019. The electrodes were printed onto a paper substrate via drop-cast. The WE consisted of a reduced graphene oxide solution functionalized with 3-(4-aminophenyl)propionic acid. The RE was prepared by painting onto the substrate with Ag/AgCl paste (Figure 3.3d). The potential was measured between the electrodes over a pH range of 4 to 10, leading to a sensor response of 46 mV pH^{-1}. Further testing was performed against human plasma and seawater, opening the possibility for application within fast point-of-care measurements.

In 2021, Mazzara et al. [50] researched the previously reported potentiometric approach and developed a pH sensor based on PANI electrodeposition on a PET substrate coated with iridium tin oxide. Sensor calibration was performed, and near-Nernstian pH sensitivity of 62.3 mV pH^{-1} was extrapolated for a 2 to 8 pH buffer range, simulating the pH range of human sweat. Reproducibility was ascertained, reaching a 3.8 % value. The device displayed good selectivity, suffering little response variation with the presence of interfering ions.

As of lately, Kucherenko and his team [37] expanded upon LIG research for application within sensing devices and conceived a LIG-based pH sensor by functionalizing LIG electrodes, etched on PI, with metallic nanoparticles, namely with poly(vinyl chloride)-based membranes containing K^+ and H^+ ionophores. The H^+ ionophores were responsible for the sensitivity and selectivity to hydrogen ions in the pH sensor, which displayed near-Nernstian performance with 56.6 mV pH^{-1}. The sensors had long-term stability of 40 days and were tested for ion-monitoring within artificial urine.

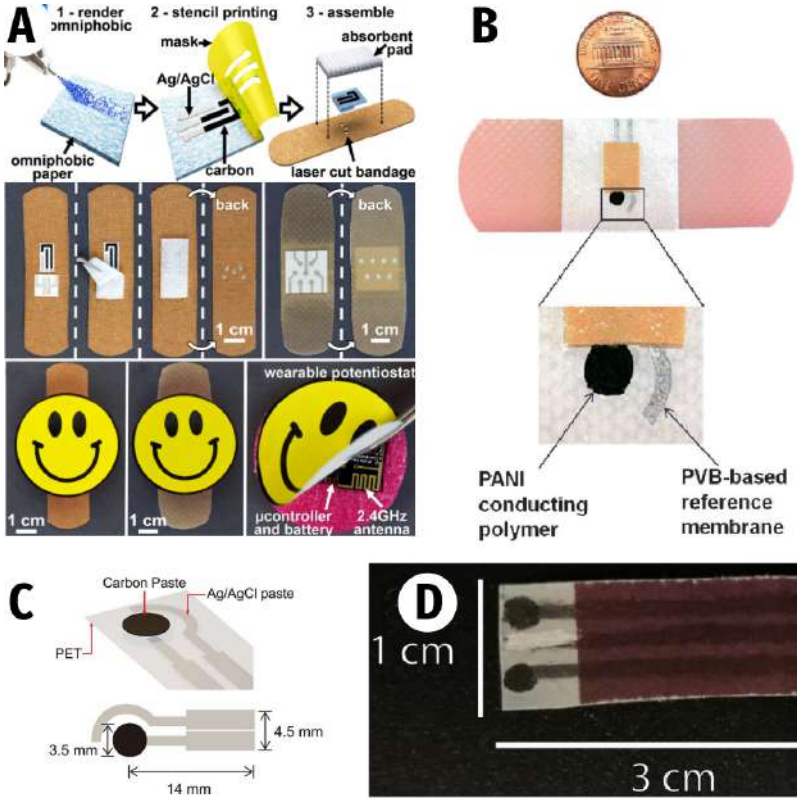

Figure 3.3: Potentiometric pH-sensing devices: (a) omniphobic paper-based smart bandages connected with wearable potentiostat (adapted from [60]); (b) carbon paste screen-printed sensor implemented within commercial bandage (adapted from [26]); (c) PANI-based carbon paste screen-printed sensor on PET substrate (adapted from [63]); (d) functionalized graphene-based potentiometric pH sensor (adapted from [92]).

3.3 Voltammetric pH-sensing Devices

Moving away from potentiometric approaches, several voltammetric pH sensing methods have been trialed. These are based on monitoring the redox response of a specific active molecule in variable pH environments, leading to a discrete measurement. In recent years, voltammetric techniques have gained traction as an alternative to potentiometric pH sensing as they yield faster and more robust responses [4] as well as higher selectivity [11].

Galdino et al. [20] experimented with a voltammetric approach for the development of a pH sensor in 2015. The proposed device was made up of graphite electrodes screen-printed onto a polyester substrate. The electrodes were subjected to chemical pre-treatment that led to the immobilization of oxygenated species at their surface. By monitoring the current peaks resulting from the redox behavior of these oxygenated species (Figure 3.4c), a strong correlation was found between peak location and pH level variation, resulting in a linear shift response within a pH range of 1.76 to 13.12 and a near-Nernstian sensitivity of 57 mV pH^{-1}.

Several active species have been the target of study within these approaches, one of

them being riboflavin which, while its redox peak shift with pH was well established, it was not until 2018 that the application as an immobilized pH sensitive electrode modifier was explored by Casimero et al. [11]. The incorporation of riboflavin-based redox film sensitive to pH onto a composite carbon-fiber-polymer laminate for application within microbial reactors was achieved. The device exhibited Nernstian behavior with a 55 mV pH^{-1} sensitivity with minimal drift within a 2-8 pH range deeming it suitable for monitoring within these batch reactors (Figure 3.4b).

More recently, Chaisiwamongkhol et al. [12] experimented with a different voltammetric approach in 2019 through electrodeposition of iridium oxide onto an iridium micro-disc electrode using square wave voltammetry (SWV) as it demonstrated to lead to lower uncertainty of the pH measurements when compared to CV. The device displayed high sensitivity (121 mV pH^{-1}) while tested in sheep's blood and buffer solution within a 2 to 8 pH range.

Still in 2021, Barber et al. [4] achieved impressive results by implementing Lin's LIG technique [42] and developing a LIG-based pH sensor on PI substrate. In this study, both potentiometric and voltammetric methodologies were explored. Potentiometric iteration was achieved by simply lasing two electrodes onto the PI substrate, a bare LIG WE and an Ag/AgCl RE, and monitoring the potential difference between them at different pH solutions. This device displayed a sub-Nernstian response with a sensitivity of 24 mV pH^{-1}. To improve upon the preliminary approach, the team experimented with a voltammetric operating principle (Figure 3.4a), devising a three-electrode pH sensor and modifying the WE with riboflavin and monitoring its redox response to different pH values. The latter exhibited a classic Nernstian response of 56 mV pH^{-1} over a 3-8 pH range.

To summarize, multiple pH monitoring approaches have been carried out recently, each with distinct characteristics. However, when compared with the voltammetric approach, potentiometric pH sensors have been much more extensively researched, expanding the interest in the development of a voltammetric system, which, while not as simple as potentiometric, the indirect assessment of pH values through the analysis of the redox behavior of a certain electroactive species may lead to faster, sturdier and more selective outcomes [11].

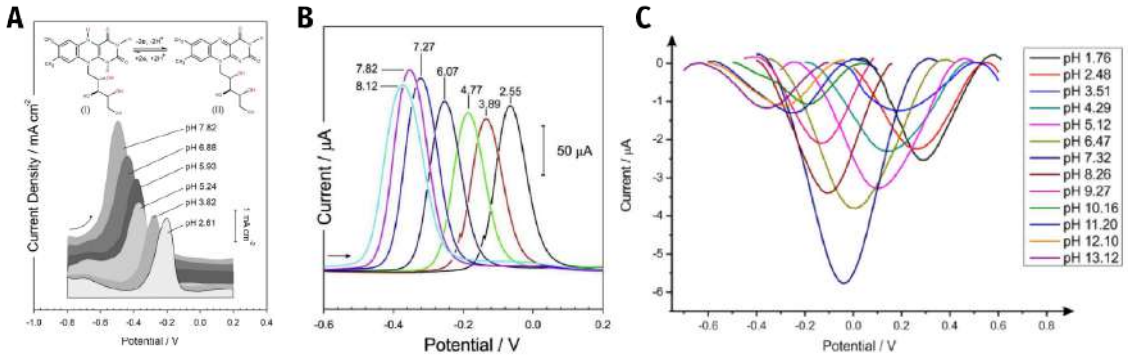

Figure 3.4: Response profile of voltammetric pH-sensing devices: (a) square-wave voltammogram of a riboflavin-based pH sensor (adapted from [4]); (b) current profile of flavin-phenol composite film pH sensor (adapted from [11]); (c) electrochemical signal from SWV on graphite screen-printed electrodes against different pH environments (adapted from [20]).

Chapter 4

Materials and Methods

In the course of this chapter, all methods and materials used throughout this thesis project are detailed. Beyond that, insight is given on the equipment required to manufacture and characterize both LIG and the pH-sensing electrodes. Furthermore, a thorough description of the experimental procedure towards fabrication and implementation of the proposed sensor is presented.

4.1 Materials

All solutions were prepared using ultrapure Milli-Q water laboratory grade. Buffer solutions were Britton-Robinson (BR) buffers, comprised of a mixture of acetic (CH_3COOH), phosphoric (H_3PO_4), and boric acid (H_3BO_3), purchased from Sigma-Aldrich. Sodium tetraborate decahydrate ($Na_2B_4O_7.10H_2O$), and riboflavin (vitamin B_2) were also attained from Sigma. Potassium hexacyanoferrate (III) ($K_3[Fe(CN)_6]$), and potassium hexacyanoferrate (II) trihydrate ($K_4[Fe(CN)_6].3H_2O$) were acquired from Roth. Sodium hydroxide (NaOH) was purchased from Labkem. Hydrochloric acid 37 % (HCl) was acquired from ITW Reagents. All chemicals were used without any further purification.

Whatman chromatography paper grade 1 (Whatman International Ltd., Florham Park, NJ, USA) was utilized as the substrate for LIG production and subsequent electrode fabrication after a wax pre-treatment using the Xerox ColorQube printer. A6 glossy plastic laminating pouches (Staples Europe BV., The Netherlands) were used to seal and encapsulate the paper-based sensors. Silver conductive ink (AG-510 silver ink, Conductive Compounds, Inc., Hudson, NH) was used to coat the electrical contacts, and Ag/AgCl ink (AGCL-675, Conductive Compounds, Inc., Hudson, NH) was implemented in the fabrication of the RE of all sensors.

4.2 Experimental Fabrication Equipment

4.2.1 Commercial CO_2 Laser

During the development of this project, the commercial CO_2 laser was a fundamental piece of equipment in the electrode fabrication process. The Center for Materials Research (CENIMAT|i3N) at NOVA University Lisbon is equipped with a VLS 3.50 desktop laser by Universal Laser Systems (Figure 4.1).

Figure 4.1: Universal Laser Systems VLS 3.50 commercial CO_2 laser available at CENIMAT|i3N.

This system is a pulsed cutting laser capable of producing a radiation beam with a wavelength of 10.6 µm and a maximum power of 50 W. As seen in Figure 4.2, it has a set of plano-convex lenses attached, with a focal length of 50.8 mm and depth of focus of 2.54 mm, that converges the light beam, producing a spot size with a diameter of 0.127 mm at the focal point [83].

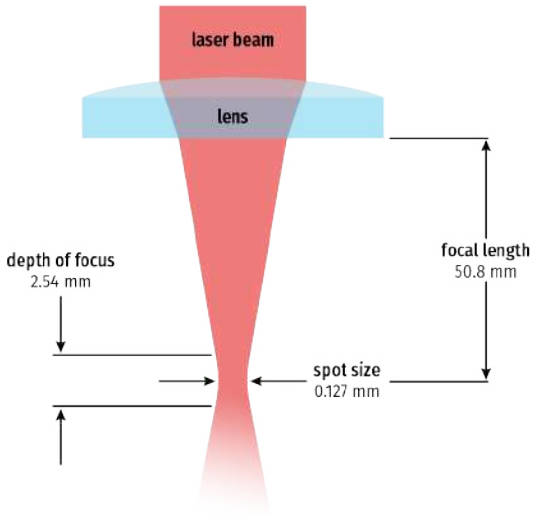

Figure 4.2: Illustration of CO_2 laser beam profile through 2.0 beam focusing lenses. Adapted from [83].

To operate this machine, the user can submit any design via the laser computer interface. This input must be a vectorial image with a specific red, green and blue (RGB) color

map used to encode particular laser parameters, such as laser speed, power, and repetition rate. Throughout this work, all designs were first conceived using Adobe Illustrator and then sent to the laser software for printing.

The computer interface is a software that allows the user to control all settings of the laser engraver (Figure 4.3). Three primary variables have to be taken into account when laser printing. The Power setting enables the selection of a laser power percentage to be applied from 0.1 to 100 %, 100 % being equivalent to the maximum laser power of 50 W and 0.1 % to 0.05 W. This setting controls the duty cycle of each laser pulse so that the higher the power, the deeper it engraves or cuts. The Speed setting allows the selection from 0.1 to 100 % of the travel rate of the system. This parameter determines the linear velocity of the laser gun motion, varying from 0.127 to 127 cm s^{-1} in Rast mode, and from 0.0254 to 25.4 cm s^{-1} in Vect mode [84]. In Rast mode, the laser beam is applied to the substrate in a series of pulses along one fixed axis sequentially, completing the design layer by layer. In contrast, in Vect mode, the system deploys laser pulses in a continuous movement following the vectorial lines of the design. The third setting is PPI which controls the pulse frequency of the laser. In other words, the number of pulses per linear inch the laser cartridge will emit while printing/cutting the material. PPI can vary between 1 and 1000 PPI. A higher value may lead to melting, charring, or burning on the edges of the design, while a lower value can generate a serrated look on the edges due to the lower pulse overlapping [84].

Figure 4.3: Laser computer interface software.

The laser system is comprised of 3 modules: the CO_2 laser source; the beam delivery system that has a set of mirrors that guide the laser beam towards the focusing lens; and the moving stages that position the laser beam in the specific X and Y coordinates during the printing process in order to complete the design. The Z position is specified by the vertical movement of the base platform (Figure 4.4).

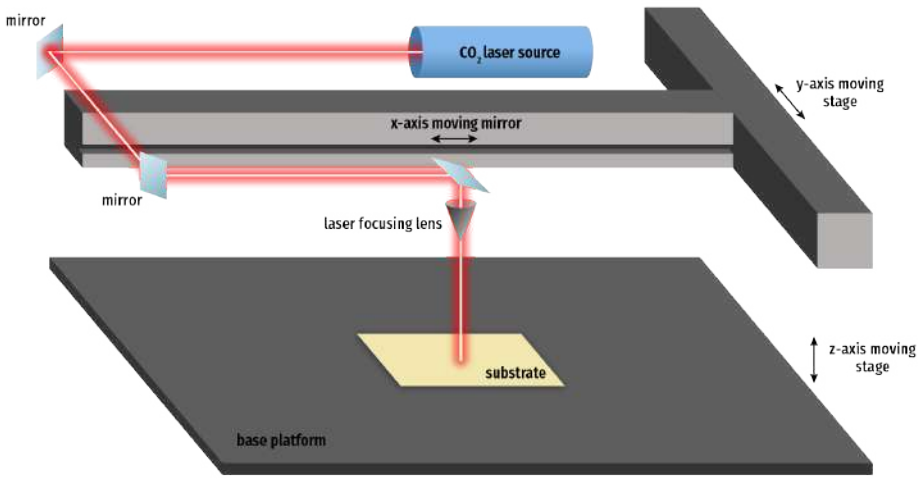

Figure 4.4: Schematic of the laser system working principle and its components.

4.3 Characterization Equipment

Several characterization techniques were employed with the aim of studying the chemical and morphological properties of the synthesized LIG and optimizing the laser settings for its fabrication. Electrochemical characterization was also required to acquire sensor performance data. The following sections provide an overview of the working principles of the equipment used.

4.3.1 Scanning Electron Microscope

SEM analysis of LIG fibers was performed using the Hitachi TM 3030Plus Tabletop Microscope (Figure 4.5). This is an imaging technique commonly used in biomaterial morphological analysis at microscopic scales, allowing the characterization of surface-level structure, composition, and defects [89]. SEM images are formed in a similar way to the traditional optical microscopes that collect their image through the emission of a light beam, the difference being that in electron microscopy, instead of light, a high-energy electron beam is scanned along the sample surface, interacting with the atoms in the object of interest. These electrons travel with very high energies (between 2 and 1000 keV), and their wavelengths range from 0.027 to 0.0009 nm, which gives this imaging method an excellent spatial and depth resolution, between 1 µm and 1 nm [91]. When the beam electrons interact with the sample, secondary electrons are ejected from the surface atoms of the specimen. A detector then captures these electrons to form the image. Additionally, electron beam interaction leads to the emission of backscattered electrons from deeper in the sample that can also be detected to form an image. Backscattered electron images have less resolution than secondary electron images but can give information about chemical composition and crystal structure [91].

Figure 4.5: Hitachi TM 3030Plus Tabletop Microscope.

4.3.2 Energy-dispersive X-ray Spectroscope

Beyond secondary and backscattered electrons, electron beam interaction with deeper atoms results in X-ray emission. EDS analysis is based on the capturing of this radiation using a detector attached to the SEM device. Radiation emission is a product of inner-shell excitation from electron interaction. When inner-shell electrons of the sample are excited from electron beam interaction, a transition to higher levels occurs. This shift leaves an inner-shell gap that is filled with an electron from higher energy levels, resulting in the emission of X-rays with energy between those levels [78]. Since this radiation has distinct energy, each element present in the sample can be identified from peak energy location and quantified by the integrated intensity [78, 91]. The system available at CENIMAT|i3N was made up of a Bruker Scan Generator and XFlash Min SVE.

4.3.3 Micro-Raman Spectroscope

MRS is a spectroscopy characterization technique based on the study of the Raman effect [7]. This effect consists of the inelastic scattering of incident radiation as a consequence of its interaction with molecules of a certain material. To induce this effect, a monochromatic laser beam is emitted towards the sample. After interacting with the sample molecules, some incident light is absorbed, reflected, or scattered [31]. A portion of the scattered light has the same wavelength as the incident light, resulting from elastic collisions, called Rayleigh scattering. The other portion of scattered light results from inelastic scattering, resulting in radiation with different wavelengths to the incident and giving rise to the Raman scattering. Analysis of this effect gives information about the sample's chemical composition and structure since every material has its unique Raman spectrum, working as a "fingerprint" of the sample [14].

4.3.4 X-ray Photoelectron Spectroscope

XPS is another chemical characterization technique based on the determination of the kinetic energy spectrum of photoelectrons resultant of incident X-ray radiation interaction with a given sample in a vacuum environment [35]. When radiation interacts with the sample's atoms, an ejection of inner shell electrons (photoelectrons) occurs with specific energies unique to each element. This is a surface-sensitive technique, being useful in the chemical assessment of almost all materials' surfaces, being able to detect all elements except helium and hydrogen [81].

Moreover, the concentration of the element is determined by the intensity of the electrons ejected. This way, it is possible to assess the biochemical composition of the sample [79].

4.3.5 4-point Probe Resistivity Measurement Device

The preliminary stage of laser parameter optimization for LIG on paper was the study of the sheet resistance of samples generated with different laser parameters. The Biorad HL 5500 was used to perform this task (Figure 4.6).

Figure 4.6: Biorad HL 5500 sheet resistance measurement device.

Sheet resistivity is an essential physical property since it can give insight into how well a given material resists the flow of electrical current. It can be measured by placing four probes on our sample and applying an electrical current between two of them, resulting in a measurable potential difference between the other two probes. The resistivity measurement is proportional to the potential difference generated, divided by the applied current. This ratio is dependent on the geometry of the sample, and the probe array [32].

Several 4-Point Probe Resistance Measurement techniques are used nowadays, such as the In-Line Spreading, Van der Pauw, Hall Bar, and Montgomery method. All of them can

be applied on the basic assumption that the sample is homogeneous [8]. In this work, Van der Pauw or Square 4-Point Probe Resistance technique was employed. This method is the second most used after In-Line Spreading and requires some prior sample conditions to get valid sheet resistance results:

1. The sample must be homogeneous.
2. The sample must be isotropic.
3. The sample must be 2D, meaning the structure thickness must be much smaller than its width and length.
4. The sample boundaries must be sharply defined.

Beyond these conditions, the sample should be symmetrical and free of any isolated impurities. The placement of four contacts achieves the connection between the sample and the probes. These contacts must be located at the edges of the piece and be as small as possible, at least one order less than the testing area [25, 8]. Once the contacts are established (Figure 4.7), two resistance measurements are performed (R_{AB-CD} and R_{BC-DA}), and the R_s is calculated using the following formula:

$$R_s = \frac{\pi}{\ln 2} \frac{R_{AB-CD} + R_{BC-DA}}{2} f \tag{4.1}$$

Where π is the numerical value for pi and f is the Van der Pauw correction factor, which is dependant of the R_{AB-CD}/R_{BC-DA} ratio [8].

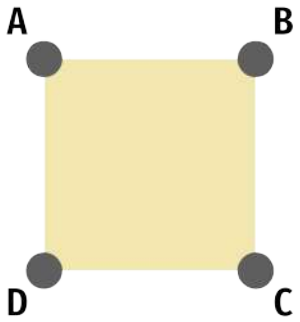

Figure 4.7: Illustration of Van der Pauw geometry sample and electrical contact setup for sheet resistance measurements.

4.3.6 Potentiostat

All electrochemical characterization and testing were carried out using the PalmSens4 Potentiostat (Figure 4.8). A Potentiostat is an electronic instrument equipped with a set of electrodes that are used to perform almost all electroanalytical experiments. Potentiostats are capable of accurately controlling the potential difference between the WE and the RE. This is achieved through the application of a specific current through an AE or CE,

resulting in the user's desired potential difference between the working and reference electrodes [52, 21].

Figure 4.8: PalmSens4 Portable Potentiostat. Adapted from [61].

The WE is the electrode where the electrochemical reaction of interest is occurring. At this site, the potential is controlled, and the resulting current is measured. WE are usually made of inert materials such as gold, platinum, or glassy carbon [21].

The CE, also known as AE, is responsible for closing the circuit in the electrochemical cell by assuring that the current that flows into the solution through the WE goes out of the solution through the CE. The CE area must be higher than of the WE so that it doesn't impair the flow of electrons [52, 21].

Finally, the RE is a stable electrode with a known potential that is used as a reference in the electrochemical cell. This electrode should have a constant potential while no current is being applied. The most common RE are the Ag/AgCl electrodes [21].

The available device is equipped with one WE, one RE, one CE and one ground connection. It has a potential range of ±10 V and a current range of 100 pA to 10 mA [61].

4.4 Experimental Procedure

4.4.1 Substrate Pre-treatment

All throughout the experimental procedure of this work, from laser parameter optimization for LIG production to sensor fabrication, Whatman paper grade 1 was used as the substrate for laser irradiation. First, paper sheets were cut into A6 standard size (105 × 148 mm). Then, chemical treatment was performed by soaking the sheets in sodium tetraborate decahydrate solution (0.1 M), 10 minutes on each side, and left to dry overnight as demonstrated in Figure 4.9a. Once dried, sodium tetraborate decahydrate will work as a fire retardant, improving the resistance of the paper fibers to thermal laser radiation, functioning as a heat sink. Since laser irradiation is a high-energy process, this chemical pre-treatment is necessary to stop the substrate from deteriorating as cellulose fibers in the paper are very fragile to these levels of radiation, as demonstrated by Pinheiro et al. [65].

After the chemical treatment, the paper was submitted to a wax coating by running the sheet through a Xerox ColoQube wax printer (Figure 4.9b). The paper with wax was placed on a hot plate for about 2 minutes at 120 °C, allowing the wax to melt and become embedded in the paper fibers (Figure 4.9b). Wax treatment was crucial to the waterproofing of the paper substrate needed for sensor fabrication and testing. Paper samples tend to lose smoothness with treatment, becoming rough and irregular. To prevent this from affecting lasing effectiveness and introducing other variables, all paper pieces were affixed to a glass substrate with tape, ensuring a smoother surface, ideal for consistent results. All experiments were performed using pre-treated paper as the substrate.

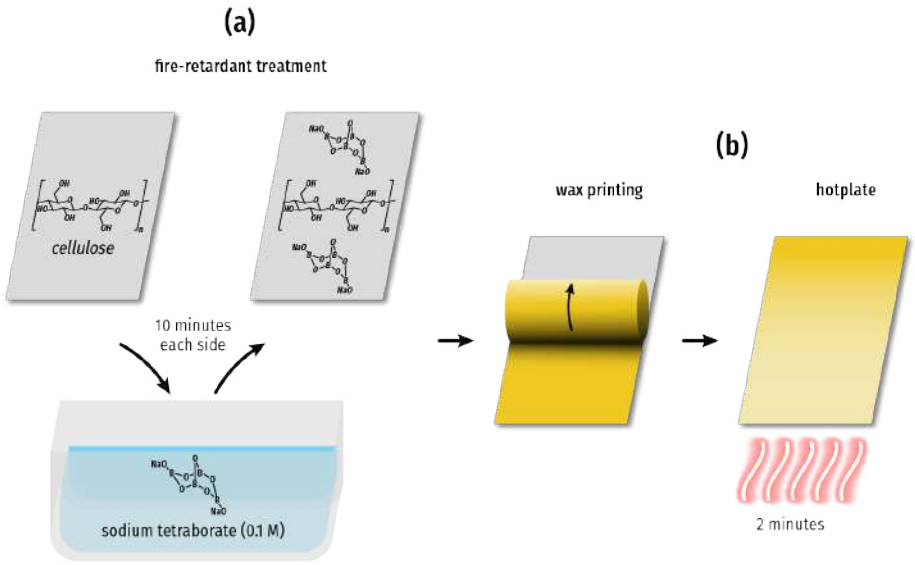

Figure 4.9: Paper substrate pre-treatment procedure: (a) chemical treatment by immersion in sodium tetraborate solution. (b) wax modification of paper substrate to induce its hydrophobicity.

4.4.2 LIG Synthesis Environment

All lasing steps were conducted in a controlled environment with room temperature varying between 20 and 25 °C. The VLS 3.50 CO_2 laser was attached to a nitrogen hose that was opened while laser etching took place, leading to a nitrogen saturated environment within the laser chamber and acting as a cooling agent. Recent advances in LIG studies have shown that lasing under a controlled atmosphere leads to changes in LIG morphology and chemical composition, allowing the user to fine-tune the hydrophobicity or hydrophilicity of the produced surface [98]. Lasing of cellulose-based substrates under an inert atmosphere, such as nitrogen, has also been shown to lead to better resistance of these materials to laser ablation [13].

4.4.3 Paper-based LIG Fabrication and Optimization

The first stage of the proposed work required optimization of the CO_2 laser operation parameters towards LIG synthesis on paper. To achieve this, a systematic study was carried out in which the influence of laser power (P) and speed (S) percentages on LIG quality was measured. Beyond that, the effect of laser defocusing (distance of substrate from the laser source) on graphitization levels was also studied. The goal of this stage was to find a set of laser parameters that resulted in LIG samples with the best electrical and electrochemical characteristics by measuring their sheet resistance and electrochemical performance.

4.4.3.1 Laser Parameter Optimization Matrix

The initial procedure consisted of varying the power and speed settings from 1 to 8 % of its maximum operating capabilities (0.50 to 4.00 W and 1.27 to 10.16 cm s^{-1}, respectively), generating a laser power vs. speed matrix. Table II.1 of annex II display the conversions of laser power and speed percentages to standard units. This matrix was scribed at a fixed height of z = -0.10" (-2.54 mm), corresponding to a distance of 0.79 mm from the focal plane. The focal plane is set at a *z* value of -0.07" (-1.75 mm).

The design used to build each row of the matrix is presented in Figure 4.10a, where each square is 2 mm wide, and its color encodes a specific power percentage in the laser software (Figure 4.3), from 1 to 8 %, from left to right. The matrix was built row by row, increasing the speed percentage by 1 % and shifting the design downwards in the laser interface (Figure 4.10b). This procedure was repeated three times for three other *z* parameter values: z = -0.05" (-1.27 mm), z = -0.00" (0.00 mm) and z = 0.05" (1.27 mm), which correspond to a distance of 0.48, 1.75 and 3.02 mm below the focal plane.

Two more trials were done to determine the influence of multiple lasing scans on LIG characteristics. Two matrices were lased at a *z* value of -0.10" (-2.54 mm) following an identical procedure to the previously fabricated matrices but with repeated lasing. For the first one, the paper was lased two times with the same parameters. For the other, the paper substrate was submitted to three lasing stages, keeping the same power and speed layouts within the matrix.

The resulting 8 × 8 P vs. S matrices give insight into possible S and P combinations that may produce graphitic materials of great interest, streamlining the options that require further characterization. Preliminary selection of these combinations was made by observing the matrices and disregarding any combination that led to substrate ablation or instances where laser irradiation seemed to have no effect or showed weak LIG production.

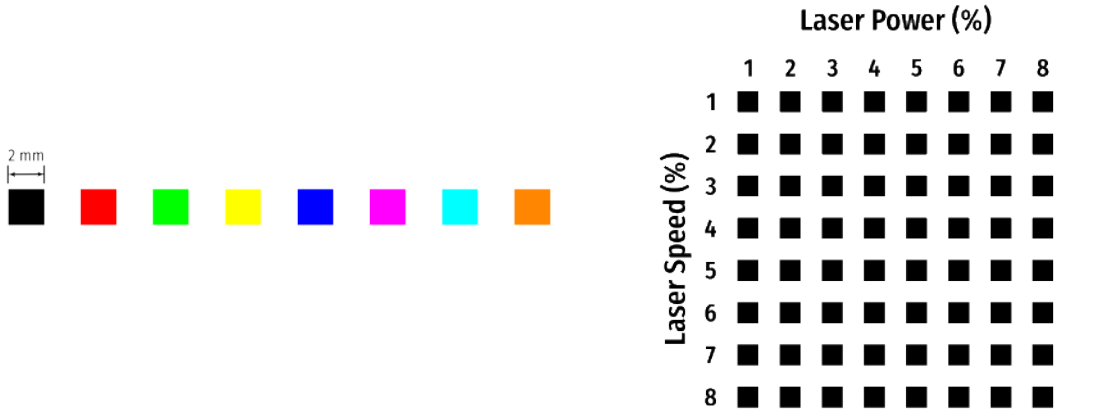

(a) (b)

Figure 4.10: Power vs. Speed matrix design: (a) design input into laser software (b) resulting matrix after lasing procedure.

4.4.3.2 Morphological and Chemical Characterization

Morphological studies of synthesized LIG were carried out through SEM analysis. All samples were 5 × 5 mm squares. This morphological characterization was conducted on LIG samples produced with different laser parameters, treated paper without any lasing applied, and LIG samples modified with riboflavin (Figure 4.11a). Graphene modification with riboflavin was achieved by drop-casting 70 µL of riboflavin solution (3.2 mM) and leaving to dry overnight at room temperature (Figure 4.11b). The test pieces were prepared and placed on the available step using double-sided carbon tape. The step was previously adjusted to the ideal height for correct focus. SEM images were captured at 100, 300, 1000, and 3000× zoom, with EDX as the observation condition and mode Mix selected, corresponding to secondary and backscattered electrons detection.

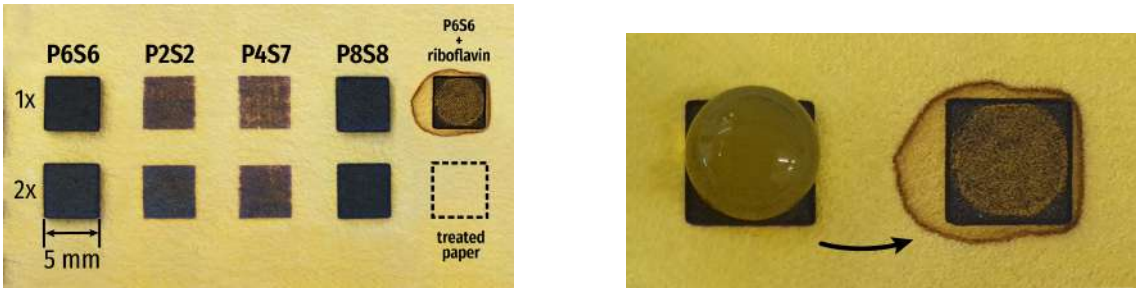

(a) (b)

Figure 4.11: SEM sample preparation: (a) printed samples (b) drop-casting process for graphene modification with riboflavin.

Following SEM observations, EDS tests were performed for chemical characterization

and thorough element analysis of the fabricated LIG. EDS trials were carried out on SEM images captured at 300× zoom, with EDX and Mix options selected. The running time was set to 60 s, the target area was 289 μm^2, and sample tilt was 0 °.

4.4.3.3 X-ray photoelectron spectroscopy

To supplement chemical characterization, XPS analysis was carried out to mainly confirm the presence of sp^2 hybridized carbon, characteristic of graphene. XPS measurements were performed using a Kratos Axis Supra spectrometer. Survey spectra were acquired with 180 W X-ray power in 1 eV steps. Elemental spectra were captured with 225 W X-ray power and 0.05 eV step size. The data were analyzed with CasaXPS software.

4.4.3.4 Micro-Raman Spectroscopy

Primary LIG optimization was complemented with a systematic study of the Raman spectra from several LIG samples produced using different laser conditions. This technique is key for analyzing the quality of the graphenic structures induced by laser irradiation.

Raman spectroscopy was done with a Renishaw inVia Qontor Raman microscope (Figure 4.12) equipped with a Renishaw Centrus 2957T3 detector using the green laser, characterized by a wavelength of 532 nm, with 10 % power, 10 s acquisition time with three accumulations. Five measurements were carried out for each sample.

Figure 4.12: Renishaw inVia Qontor Raman microscope available ate CENIMAT|i3N.

4.4.3.5 Electrical Characterization

With graphene-inducing parameters selected, sheet resistance measurements were carried out using a 4-point probe resistivity measurement device to perform electrical characterization of LIG. The test pieces were 5 mm wide squares produced by laser irradiation with the previously selected speed, power, and height parameters. For each parameter combination, four samples were fabricated to have a statistical grounding of the resistance measurements. Silver ink contacts (1.8 mm diameter) were painted on the corners of each square sample for the best electrical connection between the probes and the LIG.

A mask was created by laser cutting small circles (one for each vertex of the squares) on one side of a laminating pouch (Figure 4.13a), applying 70 % of laser power and 100 % speed. This facilitates the painting process and ensures that the contacts are as homogeneous and thin as possible, as shown in Figure 4.13b. The sample must be fixed onto a small glass substrate and placed on the middle of the four probes to initiate resistivity measurements. Then, each probe is lowered until it sets contact with the silver ink spots, as seen in Figure 4.13c.

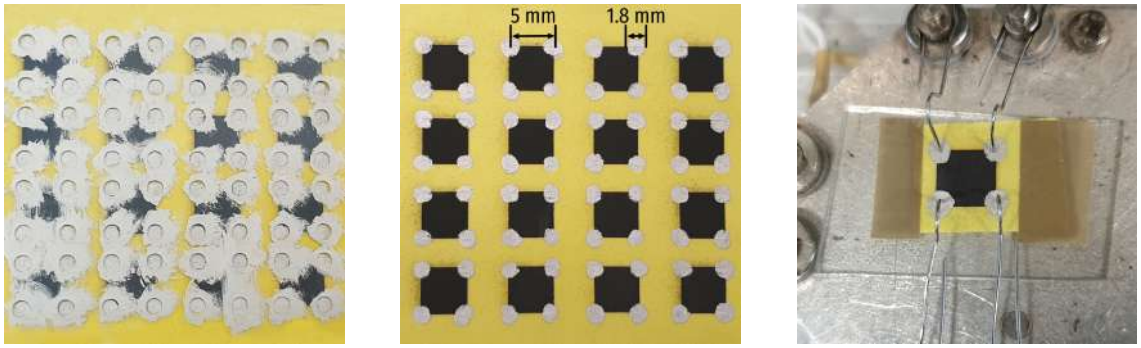

(a) (b) (c)

Figure 4.13: Sheet resistance sample fabrication and measurement setup: (a) a laminating pouch was lased to create a mask to help the painting process (b) this ensured thin and homogeneous electrical contacts; (c) 4-point probe sheet resistance measurement setup.

4.4.3.6 Electrochemical Sensor Production for LIG Optimization

After all sheet resistance measurements were acquired, a selection of the best lasing settings combinations (with lowest resistance values) was gathered with the aim of continuing the LIG optimization experiments through electrochemical characterization. Three-electrode sensors were designed in Adobe Illustrator (Figure 4.14) consisting of one WE (1.3 × 3.1 mm), one RE (1.3 × 2.1 mm) and one surrounding CE with a thickness of 1.3 mm and outer length of 13.6 mm. Each electrode had its respective track and electrical contact area (2.9 × 5.6 mm).

The design was submitted from Adobe Illustrator to the VLS 3.50 laser software and engraved onto the treated paper substrate (Figure 4.15a). Next, small openings were laser-cut on plastic laminating pouches to establish the electrical contacts and sensors' working area. The plastic sheets were previously covered with adhesive tape to serve as masks in the contact painting process.

Subsequently, the paper-based electrodes were aligned and placed inside the laminating pouches and sealed by passing them through a thermal laminator, establishing a passivation layer for the sensors.

The ensuing step consisted of painting with silver conductive ink over the respective openings of the passivation layer, using a paintbrush, establishing the conductive tracks. Ag/AgCl ink was applied over the LIG area corresponding to the RE using the same

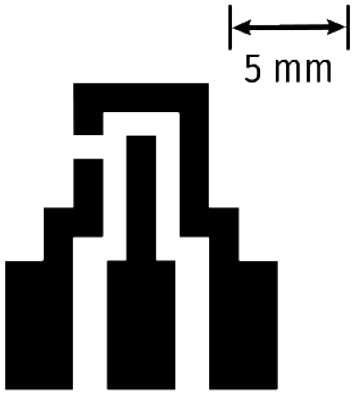

Figure 4.14: Three-electrode sensor design for electrochemical characterization comprised of one WE (1.3 × 3.1 mm), one RE (1.3 × 2.1 mm), one CE (1.3 mm wide and 13.6 mm long), and three electrical contacts (2.9 × 5.6 mm) and respective conductive tracks.

method (Figure 4.15c). Once the painting process was finished, the sensors were placed over a hot plate at 75 °C for 2 hours to allow the silver and Ag/AgCl inks to cure, enhancing their electrical properties. After the curing process, the sensor batch was withdrawn from the hot plate, and the adhesive tape was removed (Figure 4.15d). The fabricated sensors were individualized using a pair of scissors.

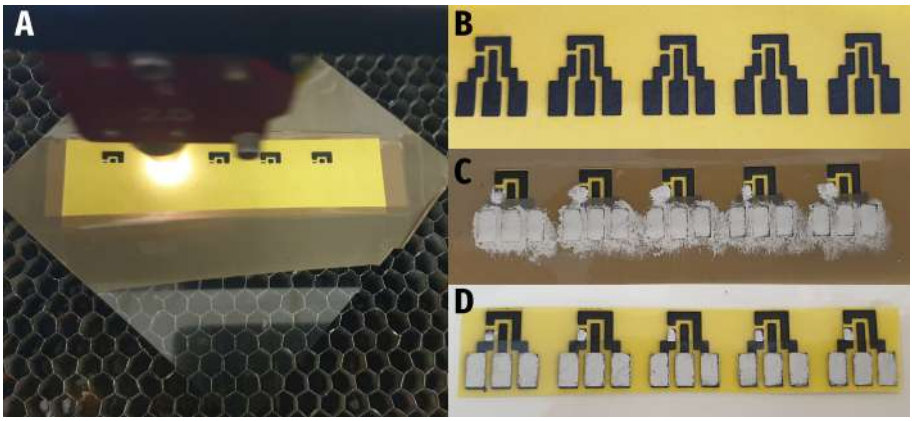

Figure 4.15: Electrochemical sensors fabrication steps: (a) laser engraving of the LIG electrodes onto the paper substrate; (b) LIG electrodes after the laser process; (c) encapsulated sensors with the silver ink contacts and Ag/AgCl RE established; (d) complete electrochemical sensors after adhesive tape mask removal.

4.4.3.7 Electrochemical Sensor Characterization for LIG Optimization

The produced sensors underwent a series of tests to evaluate electrochemical performance. The sensors were connected to the PalmSens 4.0 Potentiostat by clipping the device's crocodile tips to the respective electrical contacts: blue for the RE, red for the WE and black for the CE, as shown in Figure 4.16. Before initiating the characterization,

the sensors were subjected to an electrochemical pre-treatment procedure by running it through 5 CV cycles, from -2.0 to 2.0 V, a potential step of 0.1 V, and a scan rate of 150 mV s^{-1} with 60 µL of KCl (0.1 M) as the supporting electrolyte. After pre-treatment, sensors were subjected to subsequent CV measurements, each consisting of 6 scans, from -0.3 to 0.7 V, a potential step of 0.01 V, at a scan rate of 10, 30, 50, 70, 90, 110, 120, 130 and 150 mV s^{-1}. CV trials were carried out using a redox probe solution containing a mixture of equal parts (30 µL) potassium hexacyanoferrate (III) ($K_3[Fe(CN)_6]$), and potassium hexacyanoferrate (II) trihydrate ($K_4[Fe(CN)_6].3H_2O$), both 10 mM and prepared in KCl (0.1 M).

Figure 4.16: Sensor connection demonstration for electrochemical trials.

4.4.4 pH Sensor Fabrication and Testing

With the laser parameters for LIG on paper production and sensor fabrication optimized, the next step of this thesis was the fabrication of the proposed pH sensor, with respective modification/funtionalization and testing.

4.4.4.1 pH sensor fabrication

pH sensor fabrication followed an identical procedure as in Section 4.4.3.6. However, a different sensor architecture was used, which displayed a circular electrode setup with a 3 mm wide WE, as seen in the design presented in Figure 4.17. This architecture was employed due to its higher electrochemically active surface area, determined from CV trials, described in the next chapter (Section 5.1.4.3), as well as to facilitate electrode modification since the solution drop conforms to a semi-spherical shape (Figure 4.18a). The lasing step was performed on pre-treated paper, under nitrogen atmosphere, by means of a single lasing scan at 6 % of laser power (3.0 W) and 6 % (7.62 cm s^{-1}) of laser speed, which was previously established from Section 4.4.3.7 as the optimum settings combination for LIG production with significant electrochemical performance.

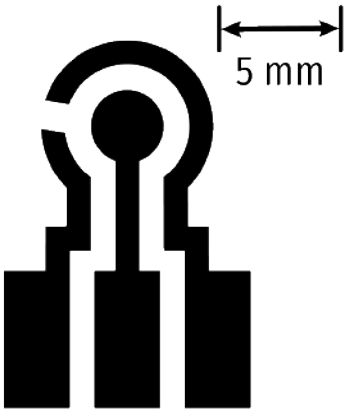

Figure 4.17: Three-electrode sensor architecture for pH monitoring: one WE (3 mm diameter), one curved RE, one curved CE, and three electrical contacts (2.9 × 5.6 mm) and respective conductive tracks.

4.4.4.2 Electrode Modification

Graphene paper-based sensors had to be modified to achieve a pH-sensitive behavior. Using a micropipette, 15 µL of riboflavin solution (3.2 mM) was carefully drop-casted onto the surface of the sensors' WE (Figure 4.18a) and left to dry overnight (Figure 4.18b). This procedure was performed with extreme care to ensure that the riboflavin drop didn't slide away from the WE and onto other components of the sensor due to the graphene's high hydrophobicity. Once dry, the sensors were ready to be tested.

(a)

(b)

Figure 4.18: pH sensor with (a) riboflavin solution (3.2 mM) drop-casted onto WE and (b) after drying process overnight.

4.4.4.3 Buffer Solution Production

To test sensor pH response, BR buffer solutions were produced by mixing in a container equal parts of previously prepared acetic, boric, and phosphoric acids solutions, all 0.4 M. Sodium hydroxide solution (1.75 M) and hydrochloric acid (0.70 mM) were prepared to adjust the pH levels of the BR buffer solution throughout the proceeding trials.

4.4.4.4 pH Sensor Testing and Validation

The experimental setup utilized in the pH sensing tests is shown in Figure 4.19: a 100 mL glass beaker containing 30 mL of BR buffer solution was placed on top of a magnetic stirrer with a magnet inside; a stand with two clamps was positioned next to the stirrer, the bottom clamp held the pH meter inside the solution, and the top secured the cables from the PalmSens Potentiostat in place; these cables were connected to the sensors through its crocodile tips. The clamp height in the stand is adjustable, which allows the sensors to be easily attached to the setup and submerged in the solution during testing.

The magnetic stirrer was turned on with a stirring rate of 200 rpm with the sensor connected and submerged. To initiate the experiment, the previously calibrated pH meter was turned on. Once the measurement stabilized on the device, pH was registered, and SWV scan was performed from -2.00 to 2.00 V, with an amplitude of 0.25 V and frequency of 20 Hz. After the scan, 700 µL NaOH was added to the beaker, inducing a rise in the pH level. Once the pH was stable, a new SWV scan was done, and the respective pH was registered. This procedure was repeated nine times until the pH levels registered on the pH meter reached ≈9, noting the pH level in each scan.

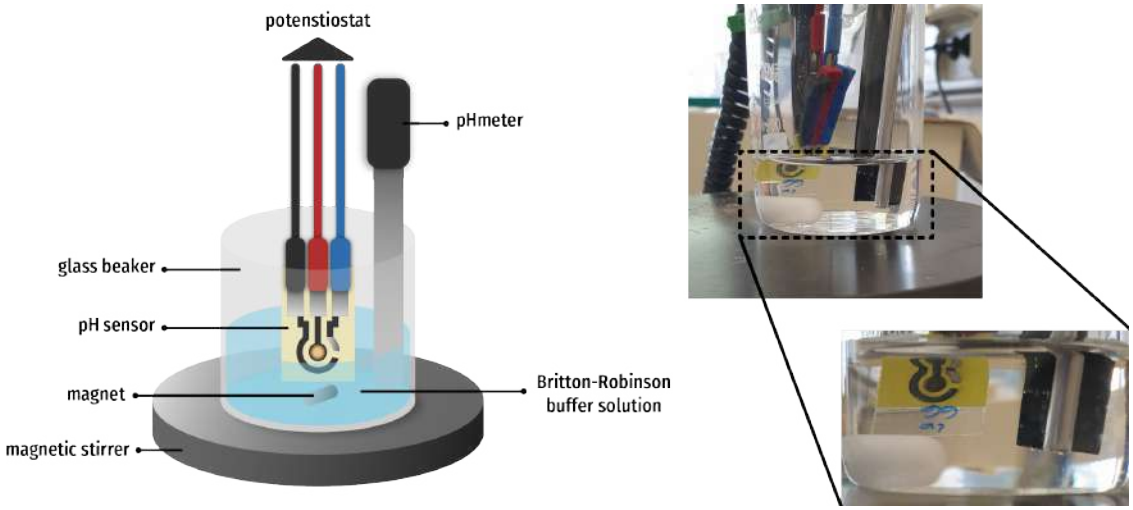

Figure 4.19: Illustration of the experimental setup for pH measurements.

Chapter 5

Results and Discussion

The current chapter reports all developments achieved from the experimental stages of this work. Laser parameter optimization results are described and implemented in the fabrication of working pH sensors. pH sensor performance is characterized thoroughly, and a possible prototype implementation is defined. Beyond that, all findings are analyzed and discussed, leading to the final remarks presented in the concluding chapter.

5.1 Laser Parameter Optimization for LIG Fabrication

Intending to achieve the best performing LIG-based sensor, a series of systematic studies had to be conducted. Firstly, laser power and speed matrices were fabricated as a means to visually infer on possible sets of laser parameters with LIG-producing capabilities. Chemical and morphological characterization was performed to scrutinize the effect of laser operation on the paper substrate and to investigate the chemical and network structure properties of the fabricated LIG samples. Next, laser defocus level was optimized by repeating the power and speed matrix procedure for different platform heights and analyzing the influence on LIG resistivity. Sheet resistance measurements were performed on samples produced with laser parameters that appeared to lead to graphitization. From this, an optimum lasing defocus was determined. A generalized study on the influence of multiple lasing exposures at the selected defocus level was conducted by repeating the lasing sequence two and three times, respectively. Electrical characterization was performed to find the best sets of laser parameters, optimizing graphene electrical performance. Finally, electrochemical characterization was done on three-electrode sensors produced with optimized laser settings. A scan rate study followed by deep analysis using the methods described in Section 2.2.1.1 resulted in the discovery of the best electrochemically performing sensor parameters that were then employed in the pH sensor

fabrication and characterization sections.

5.1.1 Power vs. Speed Matrix

The first step towards the fabrication of a working graphene-based pH sensor on paper was a laser effect study on the paper substrate. To do this, laser Power (P) vs. Speed (S) percentages matrices were lased onto paper substrate, following the procedure described in Section 4.4.3.1, varying these settings from 1 to 8 % of its range (0.50 to 4.00 W and 1.27 to 10.16 cm s^{-1}, for power and speed, respectively) at a laser height of z = -0.10". Figure 5.1a displays the resulting 8 × 8 matrix where it is observable that LIG synthesis occurs predominantly on its main diagonal, that is, where the power and speed settings display equal or similar percentage values, or at lower speed registers, where the speed percentage is somewhat lower than the power percentage.

Observing Figures 5.1a and 5.1b, it is clear that three distinct areas arise from laser irradiation, depending on the effect this process has on the substrate. For high scanning speeds coupled with lower power settings, the amount of energy absorbed by the substrate is insufficient to break the cellulose fibers' C-O, C=O, and C-N bonds, necessary for LIG formation. Thus, the laser does not affect the paper substrate, and no graphitic material appears to be forming, as seen, for example, in the P2S7 coordinates of Figure 5.1a and represented by the white region of the Figure 5.1b heatmap. On the opposite side, when laser power percentages are much higher than the scanning speed, the substrate absorbs extreme amounts of energy that are capable of breaking all chemical bonds in the substrate and don't allow for lattice recombination characteristic of LIG formation. The energy absorbed is so high that substrate ablation occurs, leading to paper perforation. Surface carbonization with some LIG formation is seen on the edges of the perforated site, which is explained by the thermal energy dissipation gradient in the boundary of laser interaction with the substrate, as described by Samouco [74]. Laser ablation can be seen in the P7S2 coordinates of Figure 5.1a and is illustrated in the red region of Figure 5.1b. One can conclude that there needs to be an equilibrium between power and speed parameters in order to achieve LIG formation through laser irradiation. The applied energy has to be sufficiently high to induce chemical bond breakage and carbon lattice recombination (as described in Section 2.4.1), but not so high that it leads to complete tearing of the substrate. These results were in line with the obtained in the works of Pinheiro et al. [65], and Samouco [74].

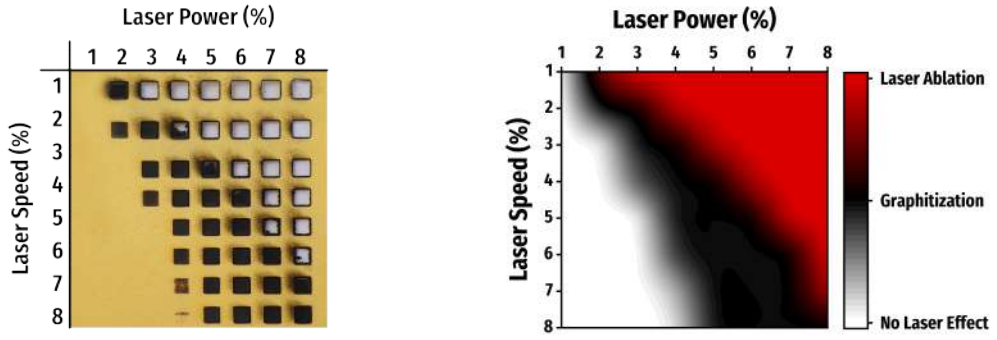

(a) (b)

Figure 5.1: Laser Power vs. Speed matrix results for z = -0.10" where (a) depicts the resulting laser-engraved matrix on the paper substrate and (b) is an illustrative heatmap for better visualization of the different laser-effect regions.

5.1.1.1 Morphological Characterization

Morphological analysis of the cellulose fiber structure of the Whatman paper substrate was performed through SEM images of pre-treated paper substrate with no laser irradiation (Figure 5.2a) and after lasing with 3.0 W of power and 7.62 cm s^{-1} of speed (P6S6) (Figure 5.2b). From Figure 5.2 observation, it is clear that laser irradiation has a big effect on the paper fiber structure. Unlased fibers present a smooth, intertwined structure, and upon laser irradiation, a high degree of ablation is observed characteristic of LIG formation. Cellulose fiber surface loses its smoothness, becoming more ragged and irregular with laser irradiation, increasing substrate porosity. This increase in degradation and porosity with the laser application to the paper substrate confirms what was previously observed at a macro level. This excess degradation/porosity is unwanted for electrochemical applications since it may lead to capillary transport of solutions within sensors' substrate, counteracting LIG hydrophobicity, and, in case of it reaching electrical contacts, short-circuiting may occur [65].

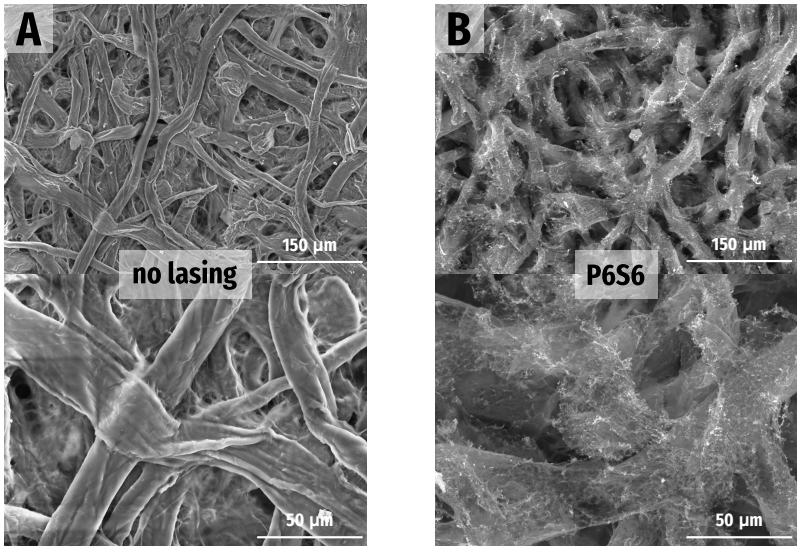

Figure 5.2: SEM images of pre-treated cellulose fibers (a) with no laser irradiation and (b) after laser irradiation with 3.0 W of power and 7.62 cm s^{-1} of speed (P6S6). Images captured at 300× (top) and 1000× (bottom) magnification.

5.1.1.2 Chemical Characterization

Chemical characterization of the produced LIG samples was conducted through an EDS analysis which gave insight into the chemical composition of different LIG samples, the paper substrate, and the relative atomic percentage variations between them. Figure 5.3 displays the resulting EDS maps of a pre-treated paper substrate sample without laser irradiation (Figure 5.3a), and of a LIG sample obtained from lasing with the P6S6 parameter combination (Figure 5.3b). Coupled with Figure 5.3c, one can see that the main constituents of these samples are oxygen and carbon, although with some differences between their relative percentages. The substrate pre-treatment with fire retardant solution may explain sodium presence on these samples. Pre-treated Whatman paper presents similar relative atomic percentages of carbon and oxygen, 53.6 ± 0.4 % and 45.9 ± 0.4 % respectively, as expected since the chemical formula of cellulose is $C_6H_{10}O_5$, having a similar atomic ratio between these elements. Note that hydrogen is not present in the chemical analysis because the equipment does not detect these atoms. An evident rise in carbon percentage to 87.8 ± 0.5 % and a decrease in oxygen to 11.2 ± 0.5 % is seen upon laser irradiation. These results once again highlight the potential conversion of cellulose fibers to LIG described in Section 2.4.1 and as verified by previous reports [65, 96, 42]

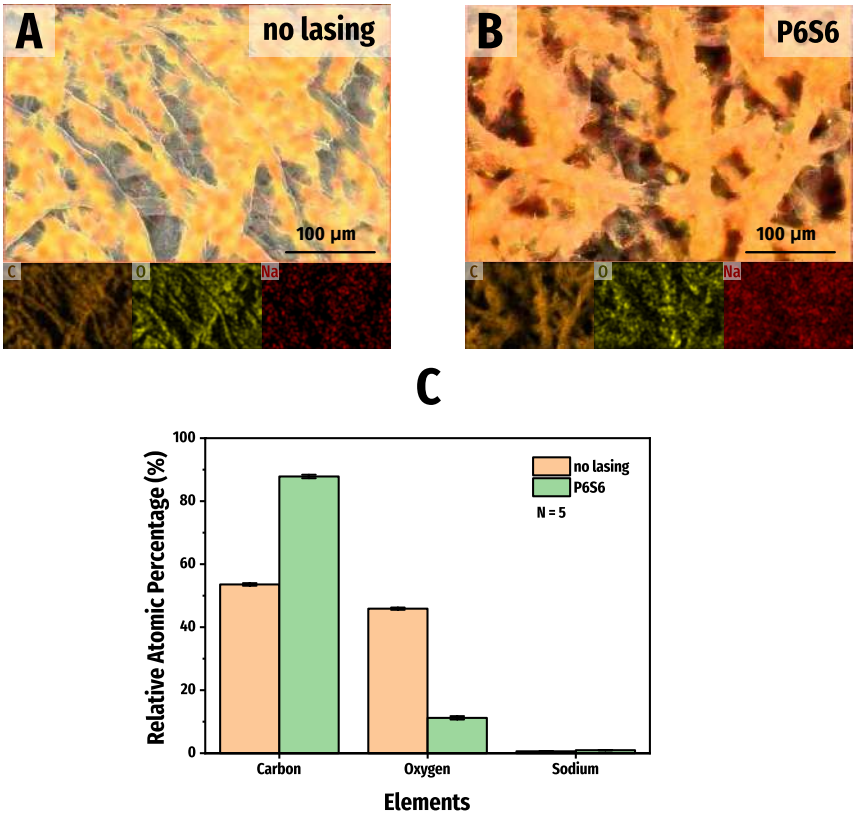

Figure 5.3: EDS analysis of pre-treated cellulose fibers (a) with no laser irradiation and (b) after laser irradiation with 3.0 W of power and 7.62 cm s^{-1} of speed (P6S6). (c) Relative atomic percentages of carbon, oxygen and sodium before (orange) and after (green) laser irradiation with P6S6 parameters.

XPS was carried out to assess the nature of the chemical bonds present in LIG samples and validate the increase in carbon content with laser irradiation, verified through EDS trials. The survey spectra presented in Figure 5.4a display a comparison between the existing elements of a LIG (Figure 5.4a, bottom) and untreated paper (Figure 5.4a, top) samples. XPS analysis of the LIG sample indicates the presence of carbon and oxygen. Carbon is expected from graphene formation, while oxygen may stem from the sample being exposed to air, which may have led to oxidation. The cellulose from the paper substrate that has not been converted to graphene also contributes to the C and O presence, as these peaks are visible in the untreated paper spectrum as well [38]. Sodium and boron are also present only in the LIG sample spectrum, which is explained by the fire retardant treatment, based on sodium tetraborate decahydrate, applied to the substrate before laser irradiation [38].

High-resolution C 1s XPS spectra are presented in Figure 5.4b. Peak deconvolution of the LIG sample spectrum (Figure 5.4b, bottom) illustrates the predominant presence of an sp^2 peak at ≈284.3 eV when compared to the much smaller C-C (≈285.5 eV), C-O (≈286.6 eV), C=O (≈287.4 eV), and O=C-O peaks (≈288.5 eV), validating the LIG conversion within laser irradiated cellulose fibers [65, 38]. These peaks contrast to those of the

deconvoluted XPS spectrum for plain Whatman paper, which presents a preponderance of the C-C peak (≈284.8 eV), with no indications of the presence of an sp^2 peak.

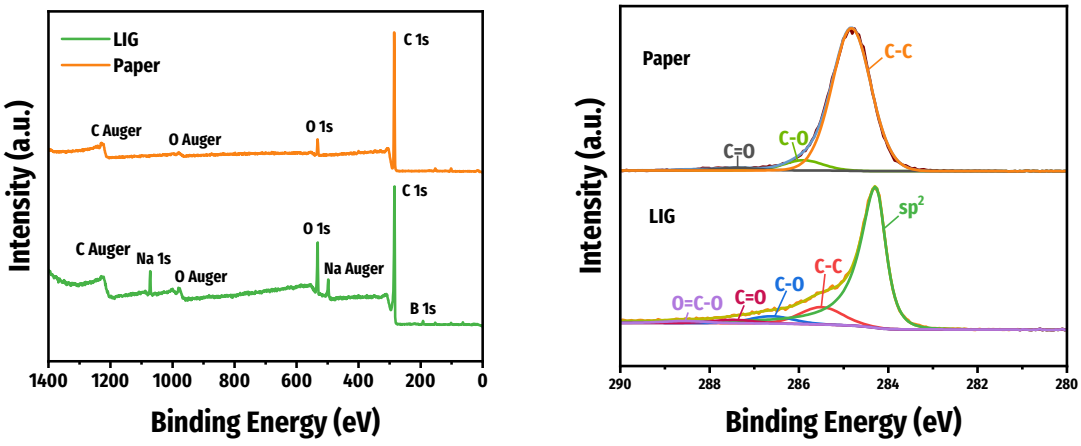

(a) (b)

Figure 5.4: XPS analysis and comparison of LIG and plain Whatman paper samples: (a) survey XPS spectra for untreated paper substrate (top), and LIG (bottom); (b) high-resolution C 1s XPS spectra with peak deconvolution of paper (top) and LIG (bottom) samples.

Raman spectroscopy was employed as a way to perform chemical structure analysis and study the quality of the fabricated LIG samples. Observing Raman spectra of a P6S6 LIG sample (Figure 5.5), three distinct peaks are observable: the D peak, located at ≈1350 cm^{-1}, is indicative of graphene structural defects or bent sp^2 carbon bonds, providing insight on the disorder in the graphene sheets and amorphous carbon species [65, 42, 10, 73]; the G peak, prominent at ≈1585 cm^{-1}, results from the first-order inelastic stretching vibrations in the sp^2 carbon bonds [10, 48], reflecting the lattice symmetry degree and overall order in the carbon atoms placement [73]; the 2D peak appears at ≈2700 cm^{-1} and is a consequence of second-order zone-boundary phonon resonance [42]. The presence of these three well-defined, narrow peaks is indicative of the formation of graphene-like material with a low degree of defects [54]. Two smaller peaks can be seen at ≈2440 cm^{-1} and ≈2940 cm^{-1}, corresponding to the T+D and D+G peaks, respectively. These are generally present in polymer-derived carbons [48], such as cellulose, confirmed by the fact that the only significant peak seen in the Raman spectra for pre-treated paper is the D+G at ≈2915 cm^{-1}. A slight shoulder can be observed within the G peak at ≈1615 cm^{-1} (see inset of Figure 5.5) designated as D', which can be an indicator of high-quality graphene-like carbon material [54].

Another set of parameters to be taken into account when analyzing Raman spectra are the peak intensity ratios, namely the I_D/I_G and I_{2D}/I_G ratios. The I_D/I_G ratio can be used to determine the graphitization quality, as well as the prevalence of defects within the crystalline structure of the graphene layers [48]. The I_{2D}/I_G ratio, on the other hand,

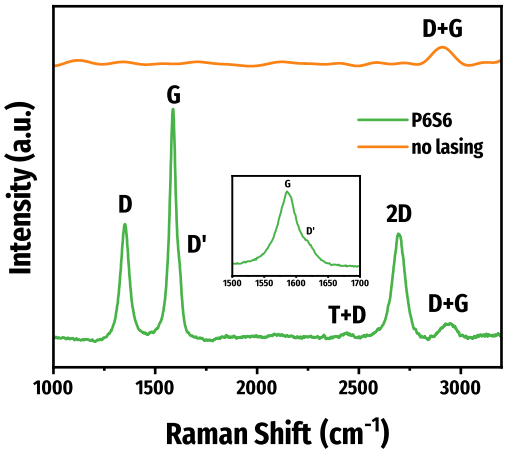

Figure 5.5: Representative Raman spectra of LIG on paper fabricated with the P6S6 laser settings vs. paper substrate with no lasing applied.

serves as a measure of the layering of graphene sheets, with graphene monolayers usually presenting $I_{2D}/I_G > 2$ [73, 65]. For the P6S6 sample an I_D/I_G ratio of 0.63 ± 0.09 (N=5) was obtained, indicating a moderate number of defective graphitic structures was already achieved with these laser parameters. I_{2D}/I_G ratio was 0.41 ± 0.06 (N=5), reflecting the multilayered morphology of the produced LIG [73].

Through Figure 5.6 it is possible to evaluate the effect of laser power variation on the quality of the produced LIG. All samples were fabricated with 7.62 cm s^{-1} laser raster speed (6 %), and the power was increased from 2, 2.5, 3 to 3.5 W (4, 5, 6, and 7 %). All Raman spectra present the three distinct graphene peaks (D, G, and 2D) at similar locations, the most noticeable difference between being the peak intensity and the T+D, and D+G peaks which are less evident (Figure 5.6a). Paying attention to Figure 5.6b, a tendency in the I_D/I_G and I_{2D}/I_G ratios is observed. As the power increases, the I_D/I_G ratio drops significantly from 0.99 ± 0.11 for 2 W laser power to 0.58 ± 0.06 for 2.5 W. This indicates that the number of defects is greatly reduced with this power increase before reaching a threshold since for higher power deliveries, the ratio and its variability increase linearly, reaching 0.63 ± 0.09, and 0.71 ± 0.12 for 3 and 3.5 W respectively. This may occur due to excess substrate ablation with higher laser power. Symmetric behavior was observed for the I_{2D}/I_G, which increased from 0.28 ± 0.10 to 0.44 ± 0.09 with laser power, reaching its peak at 2.5 W, revealing that the produced LIG had fewer layers at this point, coinciding with the least defective sample, verified from the I_D/I_G ratio. A similar response was reported by Ye et al. [99]. Table I.1 of annex I compiles all the average I_D/I_G and I_{2D}/I_G ratios determined for different laser parameters in detail, with respective standard deviations.

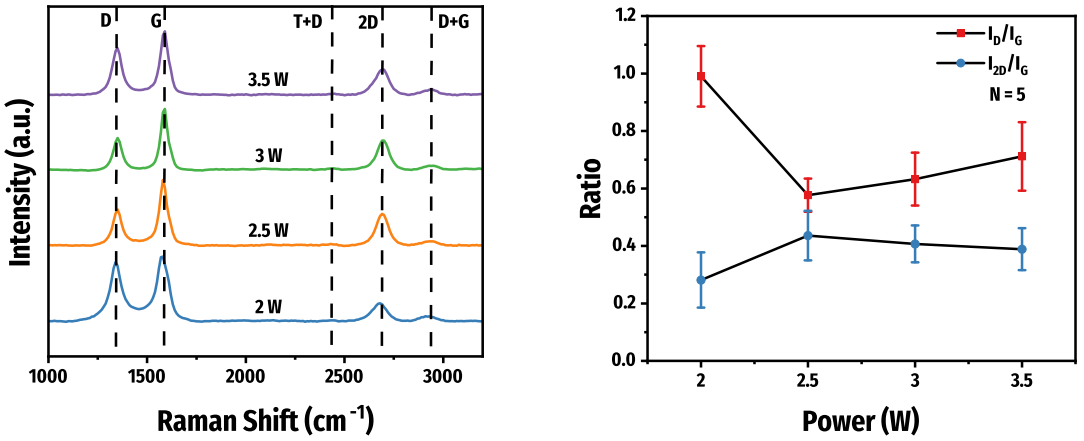

(a) (b)

Figure 5.6: Effect of laser power on LIG: (a) Laser power influence on LIG Raman spectra; (b) I_D/I_G and I_{2D}/I_G ratios dependence on laser power.

5.1.2 Laser Defocus Influence Study

The following task aimed to study the influence of laser height variation in the resulting LIG. The works of Chyan et al. [13], as detailed in Section 2.4.1, described a simple way of obtaining LIG by multiple laser exposures. Multiple exposures could be achieved either by repeating laser procedures at the focal point or by defocusing the laser beam, keeping the same pulse frequency, which leads to overlapping laser pulses and, subsequently, the equivalent to multiple laser scans. This step was performed as described in Section 4.4.3 and was necessary to optimize the lasing defocusing effect for the fabrication of sensors with the best electrical properties. With that in mind, three more matrices were constructed using the previous experimental procedure, although for z-axis settings of -0.05”, 0.00”, and 0.05” (vide infra in Figure 5.7).

The resulting matrices are presented in Figure 5.8 with their respective heatmaps. Considering laser beam profile to be symmetric from the focal point up and down, defocus levels can be arranged ascendingly from 0.48, 0.79, 1.75, and 3.02 mm corresponding to z-axis settings of -0.05”, -0.10”, 0.00”, and 0.05”, respectively. From visual analysis, it is evident there is a dependence of laser irradiation effect on defocusing level.

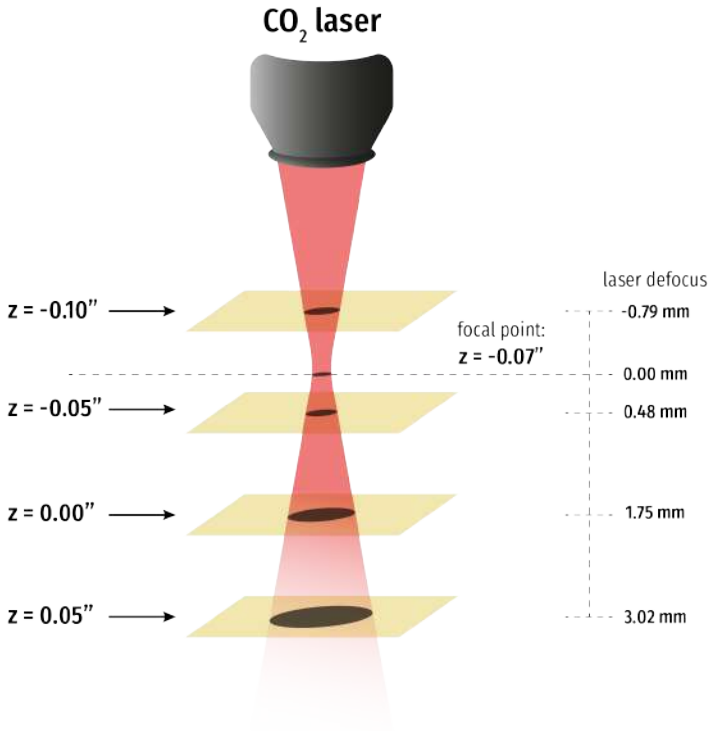

Figure 5.7: Illustration depicting selected lasing heights for matrix fabrication with distances to focal point scaled proportionally.

Comparing Figures 5.8a (z = -0.05"/0.48 mm defocus), and 5.8b (z = -0.10"/0.79 mm defocus), there is a slight distinction between the three laser-effect regions of both heatmaps, with a more pronounced laser ablation area (in red), in the first sample, leading to a smaller graphitization area (in black). This tendency isn't continuous since for higher defocusing levels, like in Figures 5.8c (z = 0.00"/1.75 mm defocus), and 5.8d (z = 0.05"/3.02 mm defocus), paper substrate suffers more damage from laser irradiation, resulting in a more prominent ablation region. A possible explanation might be that laser spot size is much larger for greater defocus, which leads to excessive overlap of pulses, equivalent to multiple laser scanning [13], which results in excess substrate perforation. As previously referred, lower defocus may also lead to a higher degree of surface ablation (Figure 5.8a). This may stem from the fact that, closer to the focal point (z = -0.05"/0.48 mm defocus), laser spot size is smaller, and smaller spot size results in higher pulse energy concentration, which can surpass graphene-inducing levels and destroy the substrate. These results lead to believe that the ideal defocus level may sit closer to 0.79 mm (z = -0.10") as it shows a larger graphitization region and, as such, a higher number of possible graphene-inducing parameters. Electrical characterization was employed on multiple sets of parameters from the different defocus levels to explore this possibility further.

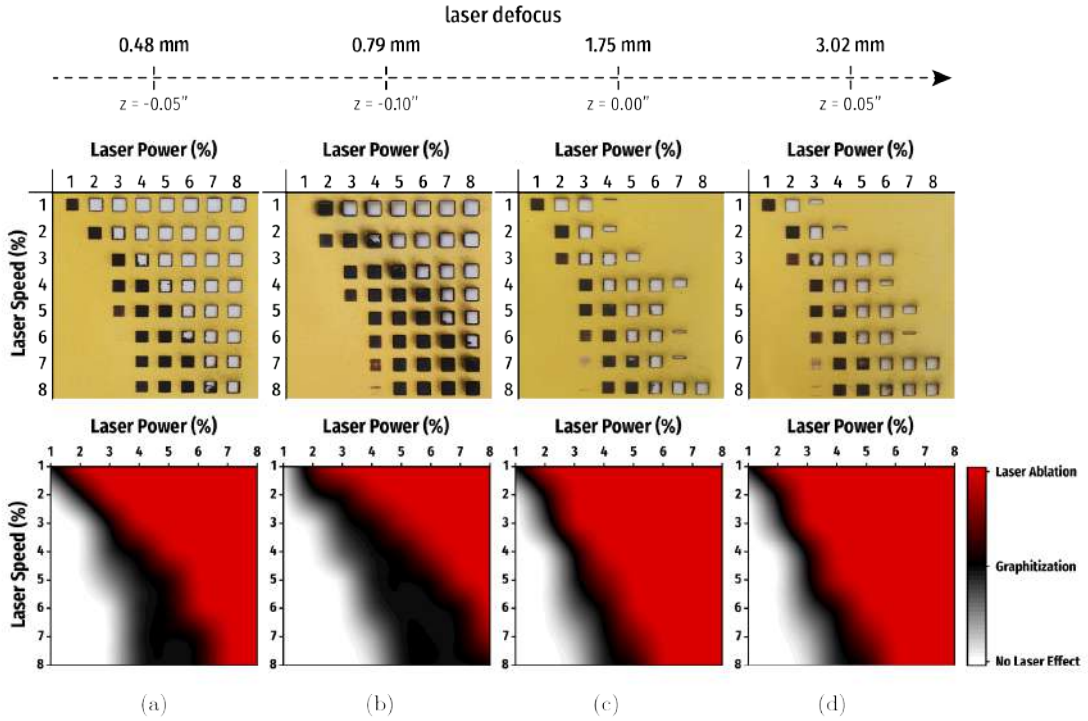

Figure 5.8: Laser Power vs. Speed matrices for different defocus levels, with respective heatmaps: (a) z = -0.05"/0.48 mm defocus; (b) z = -0.10"/0.79 mm defocus; (c) z = 0.00"/1.75 mm defocus; (d) z = 0.05"/3.02 mm defocus.

5.1.2.1 Sheet Resistance Measurements for Different Defocusing Levels

Following matrix construction and visual analysis, electrical characterization was performed through R_s measurements employing the procedure described in Section 4.4.3.5. These measurements were made on a selection of laser patterning parameters from the four multiple height settings that appeared to lead to the formation of graphitic material without substrate ablation. All samples were measured four times. Figure 5.9 presents the average resistivity results obtained. Note that percentage scales range from 3 to 8 % as a way to reduce matrix size since there were no measurable samples in the 1 and 2 % columns and rows.

Results show a significant discrepancy between sheet resistance values obtained at z = -0.10" and the remaining heights. LIG produced at z = -0.10", overall revealed much lower resistance, yielding minimum values of 21.9 ± 1.98 $\Omega\ sq^{-1}$ for 3.5 W of power, and 10.16 cm s^{-1} of speed (P7S8), and 21.9 ± 1.90 $\Omega\ sq^{-1}$ for 3.0 W of power, and 7.62 cm s^{-1} of speed (P6S6). Maximum R_s obtained was 159.3 ± 27.25 $\Omega\ sq^{-1}$ for 2.0 W of power, and 6.35 cm s^{-1} of speed (P4S5). In contrast, measurements for z = -0.05", and z = 0.05" displayed much higher resistivity, with resistance and standard deviation (SD) values being sometimes one, or even two orders of magnitude above those of z = -0.10". Note there is no table for z = 0.00" measurements, as this setting lead to only one measurable sample which displayed 5.3×10^4 ± 2.6×10^4 $\Omega\ sq^{-1}$ for 0.5 W of power, and 1.27 cm s^{-1}

of speed (P1S1). All sheet resistance measurements with respective SDs are presented in detail in Table I.2 of annex I.

Combining these results, one can see that a possible tendency arises where an increase in electrical performance (lower sheet resistances) of LIG is seen as the defocusing level increases, reaching an optimum point near 0.79 mm (z = -0.10") and then decreases with further defocusing. A similar trend was observed by Chyan et al. [13], in 2018, where, for LIG on PEI, sheet resistance values saw a significant drop (from ≈65 Ω sq^{-1} to ≈15 Ω sq^{-1}) when defocusing from the focal point to ≈ 0.75 mm. Low sheet resistance values were achieved with defocus levels between 0.75 and 1.50 mm. For higher defocusing configurations, sheet resistance saw a rising propensity. With these results, the optimum lasing height was set as z = -0.10" for further characterization and testing.

Shifting the focus of analysis to Figure 5.9b, another conclusion can be drawn: when keeping a constant lasing speed and increasing the laser power, lower R_s values were achieved. For example, for 8 % (10.16 cm s^{-1}) speed percentage, R_s decreases from 92.0 ± 3.25 Ω sq^{-1}, at 5 % of laser power (2.5 W), to 31.8 ± 1.11 Ω sq^{-1}, at 6 % of laser power (3.0 W), and 21.9 ± 1.98 Ω sq^{-1}, at 7 % of laser power (3.5 W). Lin et al. [42] reported a similar effect, varying laser power from 2.4 to 5.4 W at 8.89 cm s^{-1}, and noticing a drop in R_s from ≈32.5 Ω sq^{-1} to ≈15.0 Ω sq^{-1}. The same behavior is seen in other speed percentages within this work's results. These observations are analogous to the similarly reported effect on Raman I_D/I_G and I_{2D}/I_G ratios in Section 5.1.1.2, reiterating a possible correlation departing from the fact that higher laser power interacts deeper in the cellulose fibers, leading to a higher graphitization and degree of lattice rearrangement, hence LIG with better electrical performance. Albeit, there needs to be an equilibrium so that laser interaction is not so high that it reaches a power threshold where perforation of the substrate overcomes LIG conversion, leading to its degradation.

The following stage consisted of a generalized study of the effect of multiple lasing scans on the LIG formation, following similar procedures described in this section.

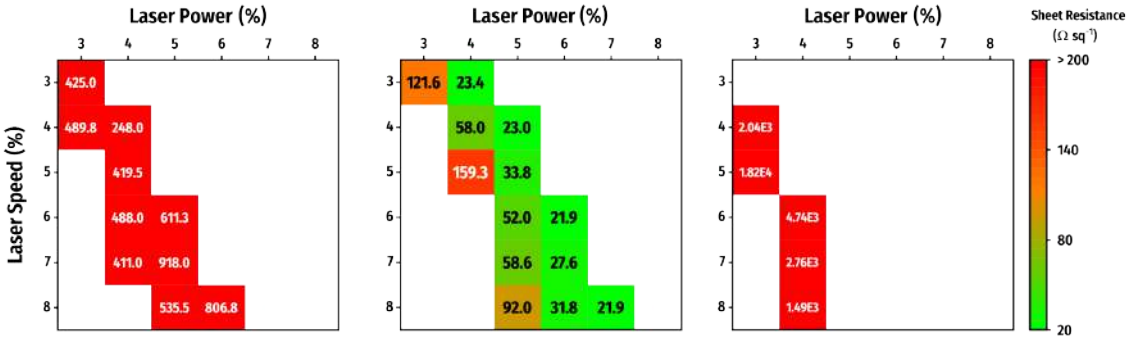

Figure 5.9: Sheet resistance measurements for different defocus levels: (a) z = -0.05"/0.48 mm defocus; (b) z = -0.10"/0.79 mm defocus; (c) z = 0.05"/3.02 mm defocus.

5.1.3 Multiple Laser Scanning Influence Study

LIG formation from different carbon precursors has been demonstrated to be achieved through multiple laser exposures, where initial laser striking leads to carbonization of the substrate, and subsequent exposures lead to graphene induction. These exposures can be achieved either by repeating lasing scans or through a single-step procedure, by laser defocus with pulse overlapping, which proved to be more time-efficient (see Section 2.4.1). The latter was explored in the previous section, where a 0.79 mm defocusing level was found to yield LIG of considerable electrical characteristics. Nevertheless, further optimization could be performed via multiple laser scans at the selected platform height. Figure 5.10 displays the resulting matrices and respective heatmaps for the previously analyzed single scan at z = -0.10", double scan, and from three lasing scans.

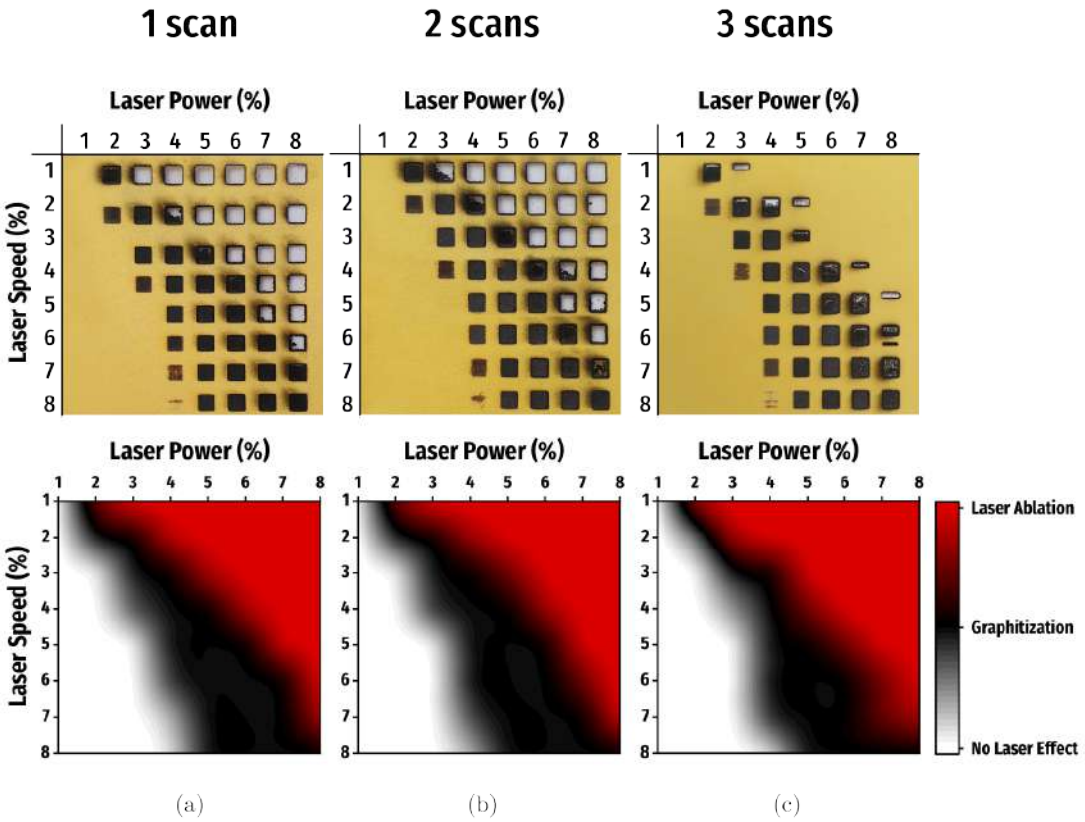

Figure 5.10: Laser Power vs. Speed matrices at z = -0.10", for single and multiple lasing scans, with respective heatmaps: (a) single lasing scan; (b) double lasing scan; (c) triple lasing scan.

From simple observation of Figure 5.10, few conclusions can be drawn, as the laser effect appears to be very similar between matrices, especially when comparing the single and double scan matrices. The beginning of the graphitization region (left border between white and black areas in the heatmaps) stays more or less constant. A slight increase in the laser ablation area is seen from the single to double scan matrix, but only in the matrix for triple laser scanning is the rise of laser ablation more noticeable. This is because, for

subsequent laser irradiation sequences, the amount of energy applied to the substrate is correlated with the number of lasing scans. The higher the number of scans, the more energy is applied, and, for each scan, the beam is striking previously carbonized material, being easier to surpass the graphene-inducing conditions. Therefore, laser ablation will occur with increasing predominance with more lasing procedures.

Electrical characterization had to be performed to complement these results and allow for more comprehensive conclusions.

5.1.3.1 Sheet Resistance Measurements for Multiple Lasing Procedures

Similar to Section 5.1.2.1, sheet resistance measurements were performed on samples fabricated with laser operating settings that showed possible LIG formation in the multiple lasing scans matrices (Figure 5.10). Results are presented in the Figure 5.11 heatmaps.

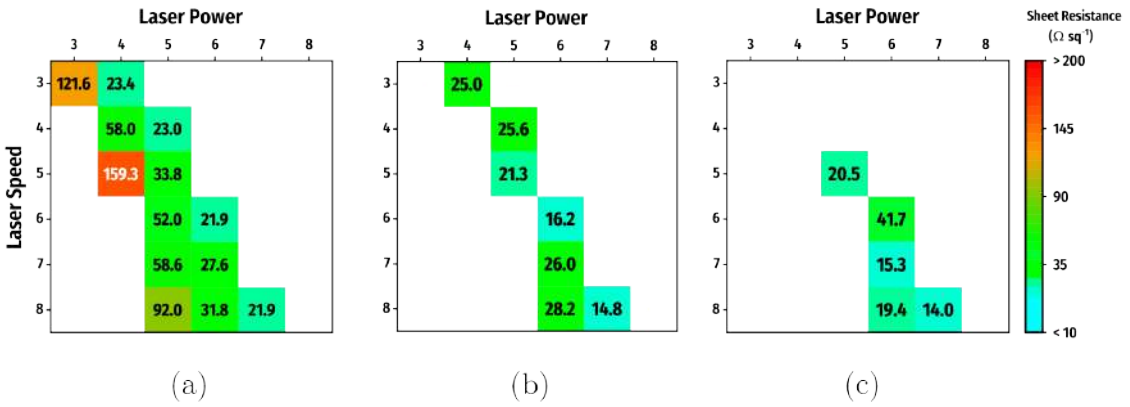

Figure 5.11: Sheet resistance measurements for single and multiple lasing scans: (a) single lasing scan; (b) double lasing scan; (c) triple lasing scan.

Although there is a decrease in the availability of samples due to substrate ablation, it is evident that there is a significant improvement in electrical performance of LIG since analogous laser settings combinations show a decrease in R_s value with multiple lasing scans. For example, for the P7S8 combination (3.5 W and 10.16 cm s^{-1}), initial R_s trials saw an average of 21.9 ± 1.98 Ω sq^{-1} (N=4), and, after two laser scans with the same parameters, a new minimum of sheet resistance was achieved with an average value of 14.8 ± 0.26 Ω sq^{-1}, and 14.0 ± 1.50 Ω sq^{-1} for three lasing procedures, with one of the measurements reaching 12.0 Ω sq^{-1}. All measurements and respective SD values are reported in Table I.3 of annex I.

In fact, 14.8 Ω sq^{-1} is a very considerable resistivity value for LIG on paper, demonstrating that a high degree of electrical optimization has been reached. Table 5.1 shows a comparison between the lowest resistivity measurements for LIG on Whatman paper and other substrates. From it, it is possible to verify that laser parameters were fine-tuned to achieve LIG with suitable electrical performance when compared with previously reached

values, presenting lower resistance than the achieved on other LIG on Whatman paper works, even lower than LIG produced on polymers like PI, polyamide (PA) and PEI.

Table 5.1: Comparison between R_s values for LIG fabricated from multiple substrates.

Substrate	**R_s (Ω sq^{-1})**	**Ref.**
PA	24.0	[46]
PEI	≈15.0	[13]
PEI	185.7	[73]
PI	≈15.0	[42]
PI	19.8	[73]
Office Paper	217.7	[65]
Whatman Paper	56.0	[65]
Whatman Paper	32.0	[38]
Whatman Paper	61.5	[64]
Whatman Paper	14.8	This work

With electrical characterization finished, the initial stage of LIG optimization was concluded, from which one can take away a general idea of the best laser operation settings for LIG on paper. Albeit, extensive electrochemical characterization procedures will be presented in the following sections as it was needed to validate and further optimize these results.

5.1.4 Electrochemical Characterization

The last phase of the LIG optimization stage was the electrochemical characterization of LIG on paper sensors. These were fabricated using laser parameters that lead to LIG with better electrical, morphological, and chemical properties in the previous sections. Electrodes were lased onto the paper substrate at the previously optimized defocus level of 0.79 mm (z = -0.10”), with the architecture presented in Figure 4.14, and following the procedure described in Section 4.4.3.6.

With the fabrication of the sensors concluded, the electrochemical performance of the sensors was examined using a potentiostat by performing CV trials at multiple scan rates (10, 30, 50, 70, 90, 110, 130, and 150 mV s^{-1}) against standard iron redox probe solution ($[Fe(CN)_6]^{3-}$]/[$Fe(CN)_6]^{4-}$] at 5 mM). Before any trial, all sensors went through electrochemical pre-treatment with CV scans against KCl (0.1 M), as described in Section 4.4.3.7.

Electrochemical characterization was performed on sensors produced with P4S3 1×, P5S4 1×, P5S5 1×, P5S5 2×, P6S6 1×, P6S6 2×, P6S7 1×, P6S7 2×, P6S8 1×, P6S8 2×, P7S8 1×, and P7S8 2× power, speed, and number of laser scans parameters, all at z = -0.10”. Note that not all power and speed combos were able to produce sensors from two lasing scans that could endure electrochemical characterization. For three lasing scans, none of the produced sensors could endure electrochemical trials. This was due to the fact that multiple lasing, despite leading to a decrease in LIG resistivity, is coupled with

an increase in substrate deterioration and in LIG porosity, which deemed these settings not suitable for electrochemical experiments as all solutions that were dropped on to the working area of the sensor would be absorbed by the paper fibers, through the passivation layer, and eventually reached the electrical contacts of the sensor.

From here onwards, the number of lasing procedures and laser height in the laser parameter description will be defined as a single scan at z = -0.10" if omitted. For example, P7S8 refers to 7 % power, 8 % speed, single scan at z = -0.10".

Figure 5.12a displays the resulting CV plots from multiple scan rates applied on a sensor fabricated using P6S6 laser settings. Only the fourth cycle of each scan rate is plotted in every CV figure. Two distinct peaks, cathodic and anodic, arise from the reduction and oxidation of the iron probes. These peaks can be seen in all the different scan rate trials, evidencing the expected occurrence of electron transfer between the LIG surface of the fabricated electrodes and the interacting redox species. Through this scan rate study, there's a visible dependence of peak current and potential location on the applied scan rate: as the scan rate increases, both anodic and cathodic peak currents (I_p) increase proportionally, in the case of the anodic peak, it rises from ≈50 to ≈340 µA; similarly, peak separation (ΔE) also increases as the scan rate increases, being ≈90 mV for 10 mV s^{-1}, and reaching ≈230 mV at 150 mV s^{-1}. When it comes to electrode kinetics, since the redox reaction is a one-electron transfer reaction, and peak separation is higher than 57 mV for all scan rates and lower than 200 mV for most of them, as explained in Section 2.2.1.2, the electrochemical behavior of this system is said to be quasi-reversible. Limitations to the electrode's reversibility may surge from hindrances in the charge transfer process, departing from the characteristic excess porosity of the fabricated LIG on paper [65].

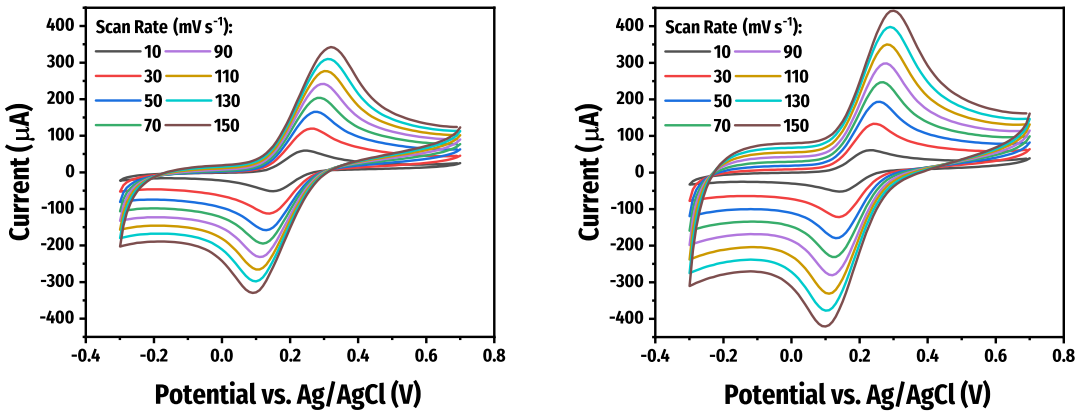

(a) (b)

Figure 5.12: Resulting CV plots for a (a) single lasing scan P6S6 sensor (P6S6 1×) and (b) double lasing scan P6S6 sensor (P6S6 2×) in the presence of ferri-ferrocyanide redox probes (5 mM in 0.1 M KCl) over multiple scan rates: 10, 30, 50, 70, 90, 110, 130 and 150 mV s^{-1}.

Observing CV trials for different sensors, one can confirm that the previously reported tendencies are consistent, with peak potential location and current being dependent on the applied scan rate. Furthermore, when comparing the results from different sensors, there are apparent differences in their electrochemical behavior. Looking at Figure 5.13 where CV scans at 70 mV s^{-1} scan rate for all single lasing procedure sensors are presented, the difference between the current responses is clear. Sensors produced with P4S3, P5S4, and P6S6 laser settings, induced higher peak currents with relatively lower peak separation.

Figure 5.12 is also very illustrative of the differences between electrochemical behavior of sensors produced with the same laser parameters but with one (Figure 5.12a) versus two (Figure 5.12b) lasing scans. Evidently, there is a significant increase in peak current values for all scan rates as well as a shortening of peak separation for sensors fabricated with a double lasing procedure, bringing the sensor's electrochemical performance closer to the reversible domain. This may be suggestive of an improvement in electron transfer kinetics of the induced LIG which will be studied through the analysis of the k^0 and electrochemically active surface area (ECA) in the following sections.

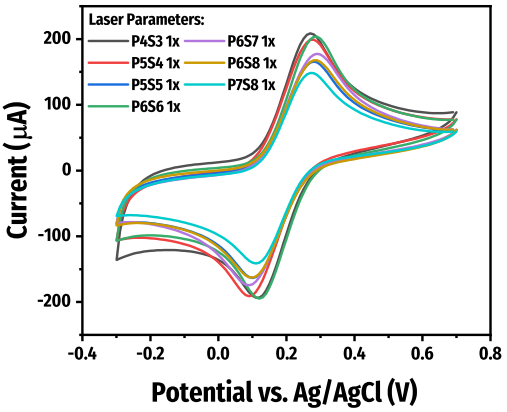

Figure 5.13: CV response for different single lasing sensors against standard iron redox probe at a scan rate of 70 mV s^{-1}.

5.1.4.1 Electrochemically Active Surface Area Determination

The ECA or electroactive area of an electrode is an important measure to be considered when analyzing sensors' performance. ECA is a key variable in material characterization for electrode applications because it quantifies the electrode surface area available for electron transfer interactions, giving the amount of reaction site, which conditions electrode kinetics [100]. This parameter should not be mistaken with the geometric area (GA), that, while it quantifies the exact physical 2D area of the electrode in question, it doesn't give us insight on the actual surface area taking part in the electrochemical reactions [22], which for high porosity materials like LIG, is much higher than the GA.

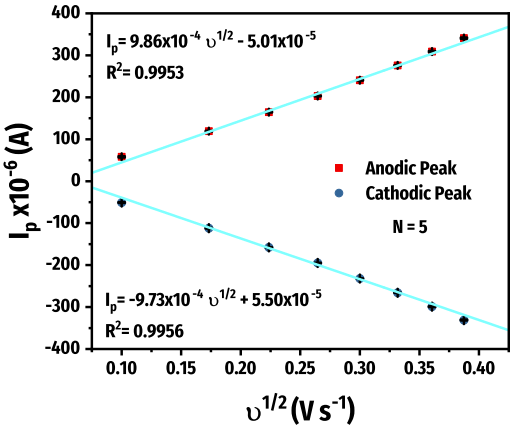

Figure 5.14: Plot of the average currents for the anodic and cathodic peaks resulting from oxidation and reduction of the redox species involved, relative to the square root of the respective scan rate in CV procedures of P6S6 single lasing scan sensor.

Determination of the ECA can be done through CV analysis. Figure 5.12a presents the current plots for CV scans at the previously described scan rates for a P6S6 sensor. By averaging the anodic and cathodic peak currents of all cycles for each scan rate and correlating it with the square root of the respective scan rate, Figure 5.14 is obtained. These plots show a linear relationship between peak currents (I_p) and the square root of the respective scan rate ($\upsilon^{\frac{1}{2}}$), indicating this is a diffusion-controlled electrochemical process. The slope (m) of the linear regression corresponding to the anodic peaks dataset (oxidation stage) can be correlated to the positive Randles-Ševćik equation for quasi-reversible systems (Equation 2.4), described in Section 2.2.1.2:

$$I_p^{quasi} = 0.436nFA_eC\sqrt{\frac{nFD_r\upsilon}{RT}} \tag{5.1}$$

Where I_p is the peak current (in A), and υ is the applied scan rate (in V s^{-1}), D_r is the diffusion coefficient of the reduced species, ferrocyanide ($[Fe(CN)_6]^{4-}$), for the oxidation stage (6.7×10^{-6} cm^2 s^{-1} [36]), in KCL (0.1 M), n is the number of electrons transferred per molecule in the electrochemical reaction (n=1), and C is the bulk concentration of

the redox probe (5×10^{-6} mol cm^{-3}). By applying the known constants, Equation 5.1 is simplified to:

$$I_p^{quasi} = 3.39\times10^{-3}Av^{\frac{1}{2}} \tag{5.2}$$

This relationship can be associated with the oxidation peaks regression slope (m) since:

$$I_p = mv^{\frac{1}{2}} \tag{5.3}$$

Equating expressions 5.2 and 5.3, it is possible to extract the value for the electroactive are of the fabricated electrode:

$$\begin{aligned} 3.39\times10^{-3}Av^{\frac{1}{2}} &= mv^{\frac{1}{2}} \\ A &= \frac{m}{3.39\times10^{-3}} \end{aligned} \tag{5.4}$$

In the case of the P6S6 sensor, the anodic slope, displayed in Figure 5.14, is ≈9.86×10^{-4} A s V^{-1}, which leads to an ECA value of 29.1 mm^2. The geometric area of the WE of the produced sensor was 4.7 mm^2, meaning there's a 617 % increase in the electroactive surface area, compared to the 2D dimensions of the electrode. These calculations were performed on CV results from all sensors that underwent electrochemical characterization trials.

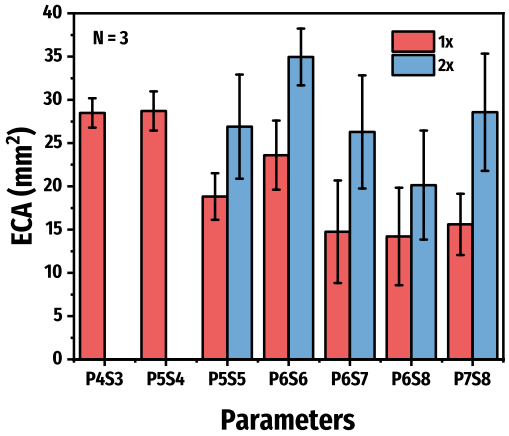

Figure 5.15: Graphic comparison between the average electroactive surface area values determined for different sensor fabrication settings with respective SDs.

Figure 5.15 shows the average ECA values with respective SDs. For each parameter, a total of three sensors were tested, reflecting three ECA values. These results, first of all, demonstrate that for all sensors, electrodes' electroactive surface area is significantly higher than geometric area, portraying the expected effect of the highly porous fabricated

LIG seen in the SEM images in Figure 5.2. This high porosity is related to the fact that raw, untreated Whatman paper is porous by nature, presenting an extensive network of cellulose fibers that leverages this effect upon laser irradiation. Next, when comparing different samples, it is visible that sensors produced with two lasing scans yield higher ECA values. This may be due to the excess laser effect on the cellulose surface, which increases fiber degradation and graphitization, which not only leads to better resistivity measurements but also increases LIG porosity, and consequently, its electrochemically active surface area. The highest ECA value was obtained for the P6S6 2× sensor, with 35.0 ± 3.29 mm^2. This laser power and speed combination also presented one of the highest ECA values for a single laser scan sensor, with 23.6 ± 3.99 mm^2, although slightly lower than P4S3 and P5S4, with 28.5 ± 1.70 and 28.7 ± 2.26 mm^2, respectively. Table 5.2 presents all determined ECA values in greater detail.

Table 5.2: Average ECA values for different single and double lasing scan parameters with respective relative standard deviations.

	1x		**2x**	
Parameters	$\overline{\text{ECA}}$ **(mm^2)**	**RSD (N=3)**	$\overline{\text{ECA}}$ **(mm^2)**	**RSD (N=3)**
P4S3	28.5	6 %	-	-
P5S4	28.7	8 %	-	-
P5S5	18.8	14 %	26.9	22 %
P6S6	23.6	17 %	35.0	9 %
P6S7	14.7	40 %	26.3	25 %
P6S8	14.2	40 %	20.1	31 %
P7S8	15.6	23 %	28.6	24 %

5.1.4.2 Heterogeneous Electron-transfer Rate Determination

The second parameter to be taken into account when performing electrochemical characterization is the k^0. k^0 is a cornerstone of electrode performance analysis since it gives insight into the speed of electron transfer between the electrode's surface and the electroactive species, even being useful to assess whether the electrochemical reaction is limited by the electrode material [71]. Like ECA, k^0 can be determined through the analysis of CV experiments calculating the dimensionless kinetic parameter (ψ), by employing the Nicholson and Lavagnini methods, described in Section 2.2.1.2.

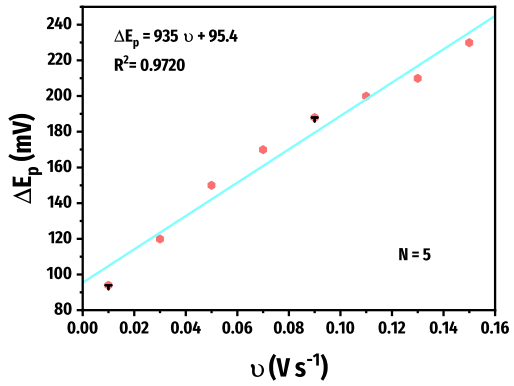

Figure 5.16: Peak separation as a function of the applied scan rate from CV procedure on a P6S6 sensor.

Figure 5.16 displays the average peak separation (E_p) for each scan rate procedure in Figure 5.12a. Since the Lavagnini method (equation 5.5) provides a direct relationship between peak separation (X) and the kinetic parameter (ψ), it is possible to extract this value by applying the different separation values.

$$\psi = \frac{(-0.6288 + 0.021X)}{1 - 0.017X} \tag{5.5}$$

A correlation between the kinetic parameter, peak separation, and subsequently, its respective scan rate is derived from these calculations. Converting the scan rate values to the inverse of their square root, Figure 5.17 is obtained, displaying this relationship via a ψ vs. $\upsilon^{-\frac{1}{2}}$ plot.

The Nicholson expression (Equation 5.6) is the final tool needed to extrapolate the k^0 of the electrode in question.

$$\psi = k^0 \left(\frac{D_o}{D_r}\right)^{\frac{\alpha}{2}} \sqrt{\frac{RT}{\pi n F D_o \upsilon}} \tag{5.6}$$

D_o = 7.2×10^{-6} cm^2 s^{-1}, and D_r = 6.7×10^{-6} cm^2 s^{-1} are the diffusion coefficients of the oxidized ($[Fe(CN)_6]^{3-}$), and reduced ($[Fe(CN)_6]^{4-}$) forms of the electroactive species in KCL (0.1M) [36]. T is the temperature in Kelvin (T = 295.15 K), n is the number of transferred charges in the electrochemical reaction (n = 1), υ is the scan rate (in V s^{-1}). α

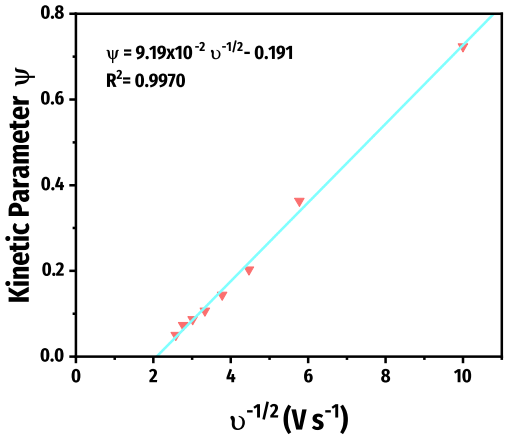

Figure 5.17: Plot of the dependency of the dimensionless kinetic parameter ψ on the applied scan rate, used in the extrapolation of the k^0 parameter of a P6S6 sensor.

is the system's transfer coefficient which can be determined using the Laviron equation $\alpha = \frac{\delta_{ap}}{\delta_{ap}-\delta_{cp}}$ (Equation 2.6), where δ_{ap} and δ_{cp} values can be extracted from the regression slopes of the linear portions of the anodic and cathodic peak currents vs. logarithm of the scan rate plots, presented in Figure 5.18.

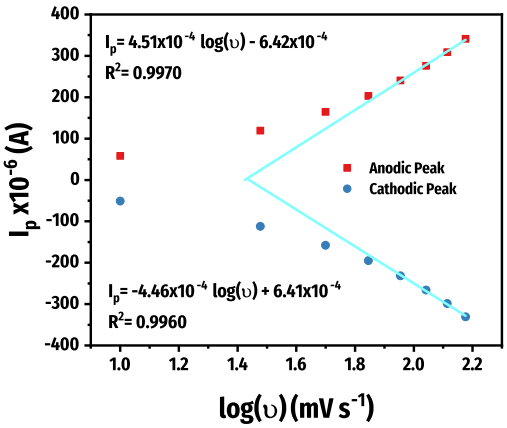

Figure 5.18: Peak current vs. logarithm of the scan rate plot, from which the transfer coefficient (α) can be calculated.

With the α value now calculated ($\alpha = 0.5029$ for the P6S6 sensor), by applying all the known constants, Equation 5.6 can be simplified to:

$$\psi = 34.195 k^0 \upsilon^{-\frac{1}{2}} \tag{5.7}$$

k^0 can easily be determined from the slope (m') of Figure 5.17, given by equation 5.8:

$$\psi = m' \upsilon^{-\frac{1}{2}} \tag{5.8}$$

Which can be equated with expression 5.7:

$$\begin{aligned} 34.195 k^0 \upsilon^{-\frac{1}{2}} &= m' \upsilon^{-\frac{1}{2}} \\ k^0 &= \frac{m'}{34.195} \end{aligned} \tag{5.9}$$

Resulting in a k^0 value of 27×10^{-4} cm s^{-1} for the P6S6 sensor. These calculations were performed on all the previously examined sensor parameters, with results being presented in detail in Table 5.3.

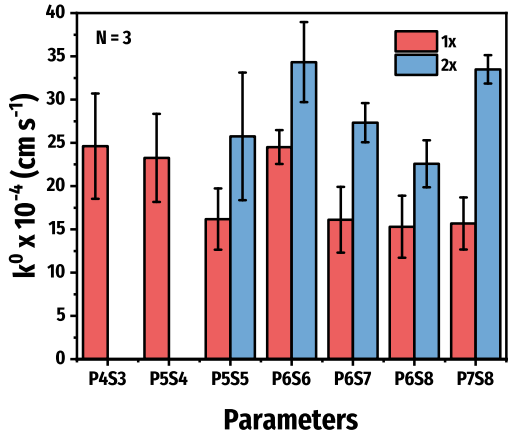

Figure 5.19: Graphic comparison between the average k^0 values determined for different sensor fabrication settings with respective SDs.

Observing table 5.3 and Figure 5.19 it is possible to verify a similar performance trend to the one seen in Section 5.1.4.1. Overall there is a leap in the charge transfer kinetics when comparing the same laser power and speed settings, but one or two lasing scans, the latter yielding better results. For a single lasing scan, P4S3 and P6S6 proved to be the best laser setting combos yielding a k^0 value of 24.6 ± 6.09×10^{-4} and 24.5 ± 1.96×10^{-4} cm s^{-1}, respectively. Despite having similar average values, P4S3 resulted in higher variability of results as well as a longer fabrication time. For double lasing procedures, the same tendency was observed, with P6S6 2× resulting in a k^0 value of 34.3 ± 4.62×10^{-4} cm s^{-1}, being closely followed by the P7S8 2× sensors, which had a lower variability and a k^0 of 33.5 ± 1.64×10^{-4} cm s^{-1}, rendering the best charge transfer properties. In general, these results are of great interest and demonstrate that a high degree of electrochemical optimization was accomplished when compared to previously reported values for k^0 of LIG on paper electrodes, with ferri-ferrocyanide redox probes in KCl (0.1 M) of, for example, Pinheiro et al. [65], who achieved an average k^0 of 6.85×10^{-4} cm s^{-1} (3.7 % relative standard deviation (RSD)).

Table 5.3: Average k^0 values for different single and double lasing scan parameters with respective relative standard deviations.

	1x		2x	
Parameters	$\overline{k^0}$ **(×10^{-4}cm s^{-1})**	**RSD (N=3)**	$\overline{k^0}$ **(×10^{-4}cm s^{-1})**	**RSD (N=3)**
P4S3	24.6	25 %	-	-
P5S4	23.3	22 %	-	-
P5S5	16.2	22 %	25.7	29 %
P6S6	24.5	8 %	34.3	13 %
P6S7	16.1	24 %	27.3	8 %
P6S8	15.3	23 %	22.6	12 %
P7S8	15.7	19 %	33.5	5 %

5.1.4.3 Sensor Architecture

To investigate the influence sensor architecture had on the electrochemical performance, an additional CV study was performed following the previous steps, only applied to electrochemical sensors with a circular WE architecture (Figure 4.17), in opposition to a square strip architecture (Figure 4.14). Figure 5.20 displays a comparison between the CV results for a 70 mV s^{-1} potential scan, and respective k^0 and ECA values for circular and squared sensor architectures, both using P7S8 laser parameters at z = -0.10". Initial observation of the CV current plot (Figure 5.20a) shows differences in electrochemical response, with the circular WE yielding higher peak current, although with higher peak separation. Figure 5.20b confirms the expected performance discrepancy with the squared sensors presenting better electron transfer kinetics with a k^0 of 12.9 ± 1.00×10^{-4} cm s^{-1} and an ECA of 14.1 ± 1.52 mm^2. In contrast, the round sensor displayed a k^0 of 10.0 ± 1.08×10^{-4} cm s^{-1} and and ECA of 18.4 ± 2.10 mm^2. Despite having slightly slower electrode kinetics, the round sensor was the selected architecture for pH sensor fabrication since it allowed for easier electrode modification by drop-casting and for its higher electroactive surface area.

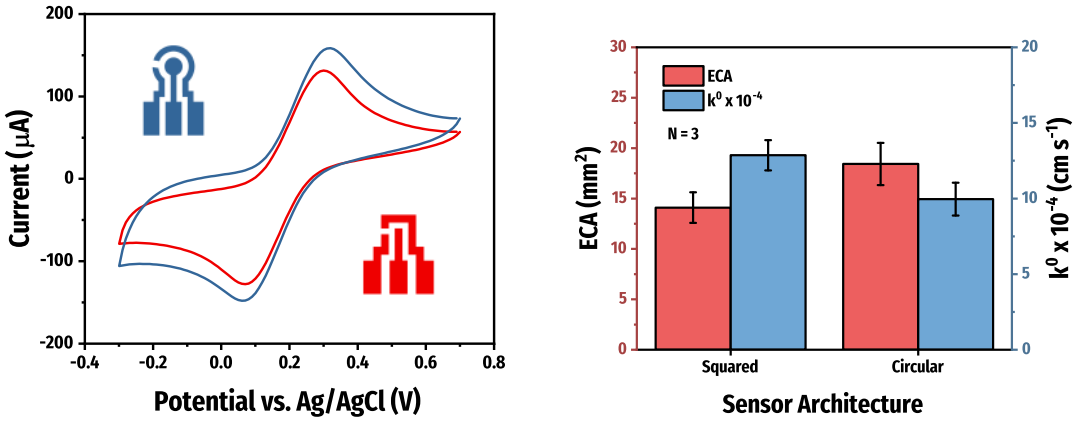

(a) (b)

Figure 5.20: Electrochemical performance comparison between different sensor architectures: (a) CV plots at 70 mV s^{-1} of both sensor architectures; (b) ECA and k^0 value comparison for both sensor designs.

5.2 pH Sensor Characterization

With the preliminary LIG optimization methodology finalized, the optimum laser operation parameters combination was defined as P6S6 1×, that is, 3.0 W of laser power, and 7.62 cm s^{-1} raster speed, at z = -0.10". These were the settings used in the fabrication of all pH sensors reported in the following stages. Despite not being the laser settings combo that resulted in the highest k^0 and ECA values, it displayed similar electrochemical performance. Furthermore, single scanning proved to be better in the context of this work since it results in lower power and time consumptions, adding upon the general sustainability motif behind paper-based sensors. Beyond that, while displaying better electrochemical properties, multiple laser scanning sensors were very unstable in some cases. This was due to the excessive porosity as a result of extreme laser ablation, leading to absorption of the buffer solutions by the paper network until it reached the electrical contacts, inducing a short-circuit and turning the sensor unusable (Figure 5.21).

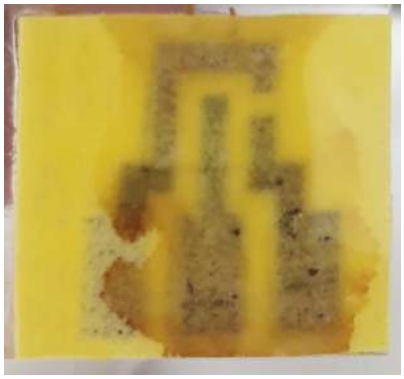

Figure 5.21: Effect of extreme LIG porosity on electrochemical sensors, observed from the backside.

pH sensors were fabricated following the procedure described in Section 4.4.4. WEs were modified with riboflavin or, more commonly known, vitamin B_2 ($C_{17}H_{20}N_4O_6$). Riboflavin is an organic compound that has been previously used in pH-sensing devices due to its pH-dependent response in electrochemical procedures [4, 11]. One of the reasons it makes this compound a good fit for electrode modification is the fact that it is biocompatible, making it suitable for pH monitoring within wound environments with no risk for the user. Figure 5.22 highlights riboflavin's redox transitions, characterized by a two-electron transfer electrochemical process between the reduced (I) and oxidized (II) species of this compound [4].

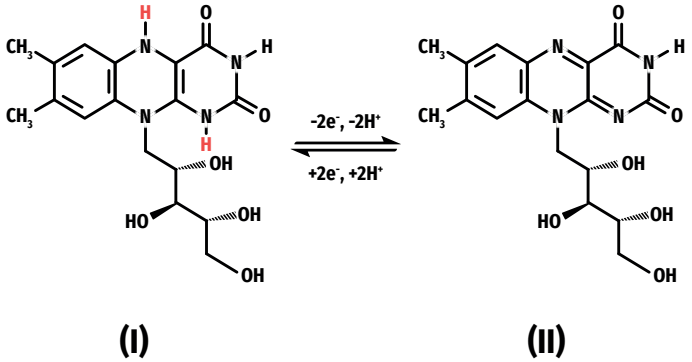

Figure 5.22: Representation of the different chemical structures of the (I) reduced and (II) oxidized forms of riboflavin throughout its electrochemical transitions.

This redox transition and its property alterations with pH variation will be the target of study in the characterization of the proposed pH sensor throughout the following sections.

5.2.1 Morphological Characterization of Riboflavin-Modified Electrodes

SEM imaging provided a detailed look into the microscopic nature of the riboflavin modification and the effect this had on the LIG morphology. Figure 5.23 compares the structure of laser irradiated cellulose fibers, both with 3.0 W of power and 7.62 cm s^{-1} of speed (P6S6), after riboflavin modification (Figure 5.23a), and bare LIG (Figure 5.23b). Figure 5.23a displays a high amount of riboflavin crystals adsorbed onto the LIG porous surface. These crystals range from 50 to 100 µm in length and can be seen deep into the cellulose fiber network. No significant alteration is seen in the LIG sites within this sample, leading to the belief that riboflavin solution drop-casting and its adsorption do not alter LIG morphology.

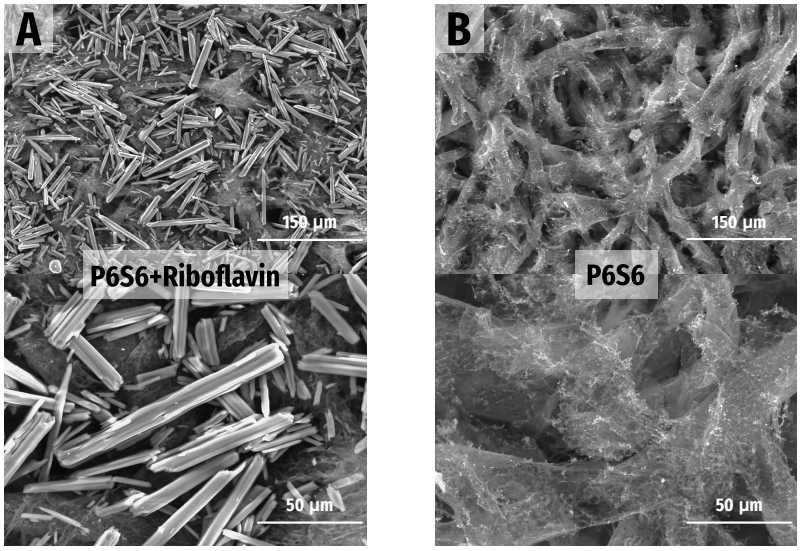

Figure 5.23: SEM images of LIG surface before (b) and after (b) riboflavin modification. LIG was induced by laser irradiation with 3.0 W of power and 7.62 cm s^{-1} of speed (P6S6). Images captured at 300× (top) and 1000× (bottom) magnification.

5.2.2 pH Sensor Measurements

To employ the fabricated devices in pH sensing procedures, SWV was carried out from -2.00 to 2.00 V, in BR buffer solutions at different pH levels (adjusted with NaOH additions) as described in detail in Section 4.4.4.4.

SWV is a voltammetric technique similar to CV where the current response of an electrochemical cell is monitored while the potential is scanned between an initial and final value. The difference is that SWV is a pulsed technique. That is, the potential is not linearly scanned like in CV; instead, a series of potential pulses is applied, generating steps that connect the initial and final potential. This technique has been shown to lead to better results in voltammetric devices, with improved signal-to-noise ratios, and consequently, better peak definition that facilitates measurements [12]. Figure 5.24 puts in view the resulting current plots from the SWV scans of two different sensors, one modified with riboflavin and the other being bare LIG (without WE modification).

Extremely contrasting results were obtained: in Figure 5.24b, for every scan, there's a clear current peak located, initially, at ≈-409 mV for pH 2.65, shifting towards more negative potentials with subsequent measurements at higher pH levels, reaching ≈-938 mV at pH 9.29. These peaks are a product of riboflavin oxidation reaction, shown in the I→II process of Figure 5.22 and their location comes over as being dependent on the solution pH, deeming it as a possibly suitable method for pH measurements. Figure 5.24a on the other hand, exhibits the resulting current in the bare LIG sensor, where no riboflavin oxidation peaks occur, evidencing only an increase in baseline current with subsequent measurements at rising pH levels. This validates the reported peaks as being specific to riboflavin electrochemical behavior.

Intending to prove the riboflavin peak potential shift was, in fact, tied to the pH

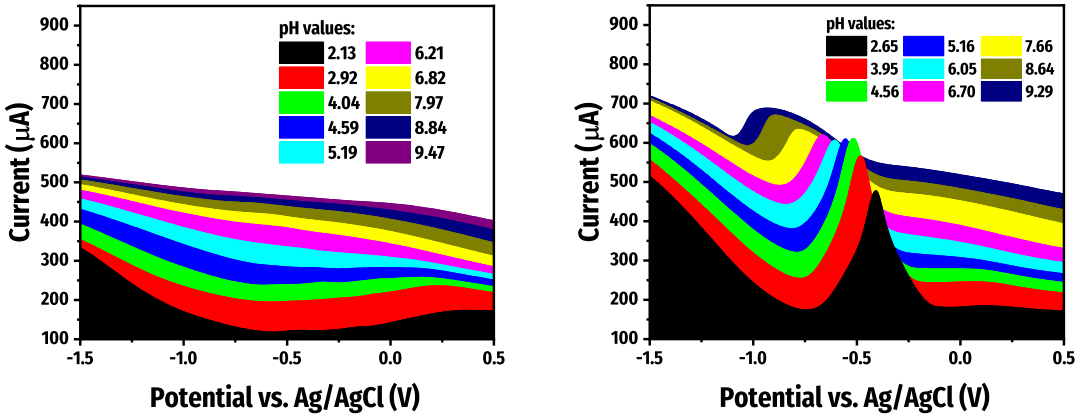

(a) (b)

Figure 5.24: Comparison between resulting SWV plots of (a) bare LIG sensor and (b) riboflavin modified sensor throughout varying pH values.

variation of the solution and not a result of sequential scans, a total of five subsequent SWV trials were performed for similar pH values (e.g. 5.24, 5.24, 5.25, 5.28, and 5.30). These scans were carried out over a short period of time. The process was repeated for five different pH ranges. Figure 5.25 shows the resulting riboflavin oxidation peaks for all scans where one can see that there is an agreement between the peak location at similar pH values. The shift of these peaks occurs only with subjection to more distant pHs, confirming that the movement is indeed due to the pH of the solution in which the sensor is immersed and not from consecutive voltammetric cycles.

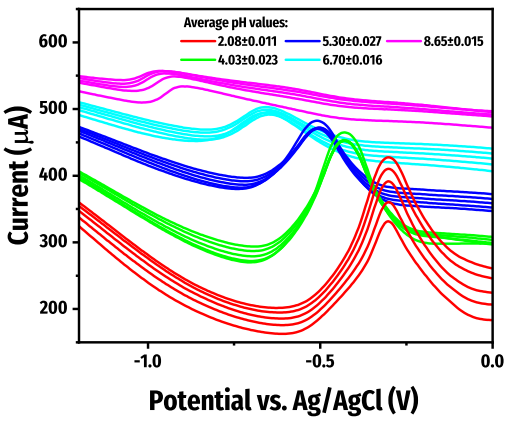

Figure 5.25: Graphic of the resulting riboflavin redox peaks for different pH values proving a pH-dependence shift towards more negative potentials at higher pH ranges.

Furthermore, an additional test was performed starting at a higher pH level buffer solution and reducing it to more acidic pH values with the addition of HCl (0.70 mM). Once again, the same pH dependence of the riboflavin current peak position was observed (Figure 5.26), with more alkaline pH levels leading to the redox peak locating at more

negative potentials. The peak position shifted to less negative potentials as the pH levels were reduced confirming once again, that the redox peak movement is due to the pH of the solution in which the sensor is immersed.

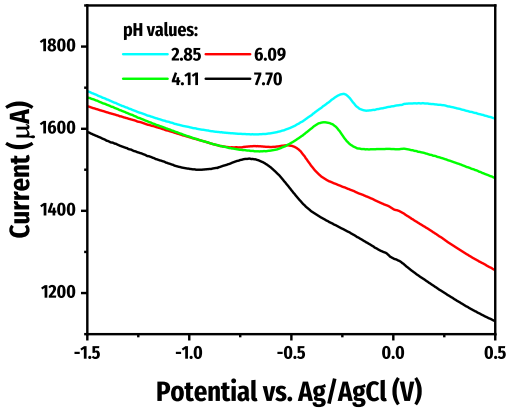

Figure 5.26: Graphic of the resulting riboflavin redox peaks for different pH values applied in reverse order, from high pH levels, to more acidic ones, proving once again the riboflavin peak shift dependence with pH.

5.2.3 pH Sensor Calibration

To correctly characterize the pH sensors, it was necessary to calibrate them by converting the acquired current measurements to a pH vs. peak potential relationship, from which the user could extract the pH value of the sensor environment. Some post-processing had to be executed to correctly perform this calibration. SWV procedures were conducted as previously described in Section 4.4.4.4, resulting in potential vs. current plots as shown in Figure 5.27a. Once again, the riboflavin oxidation peaks emerge in every scan. For a solution pH of 2.70, the oxidation peak was located at -353 mV, shifting negatively with higher pH levels until reaching -857 mV at pH 9.47. It is these peak potential locations that need to be extracted, and then, by plotting them against the respective pH value at which they were acquired, the calibration curve is constructed (Figure 5.27b). There aren't error bars displayed due to each data sample of the plot representing a single measurement because, in this experiment, it was not possible to perform subsequent SWV scans for the exact same solution pH since this wasn't a static parameter.

The calibration curve is a valuable characterization tool, conveying the pH-sensing capabilities of the device through its linear regression slope. In the case of Figure 5.27b, the fabricated sensor presented a sensitivity of -81.9 mV pH^{-1}. Therefore, the linear regression curve expression E = -81.9 pH-120.5 (R^2=0.9824) can be used to extrapolate the pH value of any solution the sensor is placed in based on its peak location.

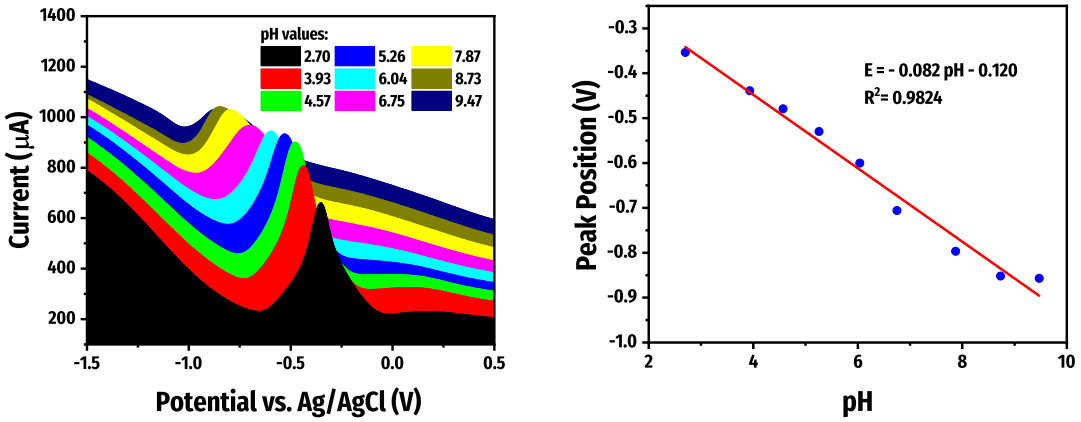

(a) (b)

Figure 5.27: pH sensor calibration procedure results: (a) primary SWV plots for different pH levels; (b) calibration curve from the extrapolation of peak potential locations towards each solution pH.

5.2.4 pH Sensor Performance Summary

The sensitivity of pH sensors can be obtained through the *Nernst Equation* (Equation 2.2), which can be modified by converting the natural logarithmic to decimal logarithm:

$$E = E^0 - 2.303\frac{RT}{nF} \times (-\log_{10}[H^+]) \tag{5.10}$$

Equation 5.10 can be further modified by applying the constants and replacing the oxidized and reduced species concentrations for the hydrogen ion activity in the electrochemical reaction. As reported by Galdino et al. [20], molecules immobilized on the surface of the electrodes can be excluded from the *Nernst Equation* resulting in a solely pH-dependent potential equation [20, 63, 70]:

$$E = E^0 - 0.05916\text{pH} \tag{5.11}$$

Where -0.05916 V pH^{-1} (-59.16 mV pH^{-1}) is the potentiometric sensitivity corresponding to Nernstian potential shift, E is the measured potential, and E^0 is the standard electrode potential.

The voltammetric scans and calibration curve extrapolation procedures were conducted on a total of 8 sensors. Table 5.4 summarizes the pH sensing performance data obtained for all tested sensors.

Table 5.4: pH sensors sensitivity summary with respective y-intercept and R^2 values.

Sensor	Sensitivity (mV pH^{-1})	y-intercept (mV)	R^2
1	-81.2	-120.5	0.9824
2	-74.9	-176.3	0.9582
3	-74.4	-116.9	0.9803
4	-82.5	-148.1	0.9750
5	-74.3	-143.7	0.9936
6	-77.8	-197.2	0.9821
7	-79.3	-184.6	0.9747
8	-80.6	-99.4	0.9805
Average	-78.2 ± 3.37	-148.3 ± 35.19	0.9784 ± 0.01000

An average pH sensitivity of -78.2 ± 3.37 mV pH^{-1} was reported for a linear range of ≈2-8 pH, corresponding to Super-Nernstian sensor behavior [47], given by a sensitivity value above the theoretical limit of the Nernst equation (-59.16 mV pH^{-1}). The y-intercept values correspond to the standard electrode potential, which resulted in an average of -148.3 ± 35.19 mV. Super-Nernstian devices are capable of a more precise pH detection performance [47] making these findings of great interest for future application and expansion.

Linear Range

In order to ensure that the produced sensors could be employed within smart bandage technology, it was vital that the pH sensitivity range would match or encompass that of the wound environment, making the sensor performance clinically relevant. As described in Section 2.1.4, wound pH is an ever-changing parameter, varying from ≈4 in the inflammation stage and peaking at ≈8, which lies within the 2-8 pH range of the fabricated sensors. This positively reinforces the possibility of the proposed paper-based pH sensors being implemented within smart bandages. The pH range was verified by observing the riboflavin peak shift within pH values outside the reported range. As seen in Figure 5.28, linear response of peak locations is seen in the 2-8 pH range (green area). Linearity in the peak potential shift is lost outside these pH values (red areas), with some instances even leading to a deletion of the oxidation peak. This may be due to the fact the extreme pH values compromise the structural integrity of the cellulose fibers of the paper substrate and LIG surfaces, affecting the overall performance of the sensor.

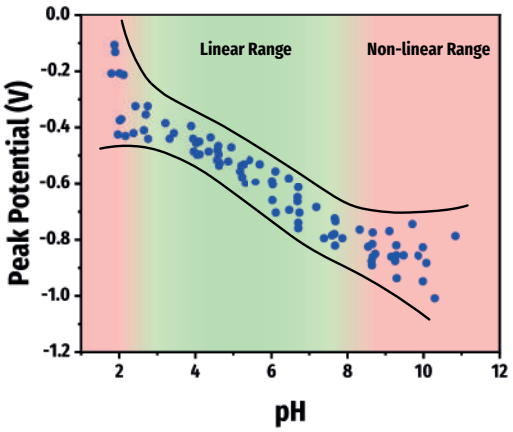

Figure 5.28: Dispersion graph containing all registered peak locations for different pH values of all tested sensors, conveying a clear linear (green) behavior over a 2-8 pH range and a non-linear (red) response outside this pH window.

Sensor Reproducibility

Sensor reproducibility was another important parameter to be taken into account in this work as it gives insight into the performance discrepancies between different sensors. Reproducibility was evaluated from the SD of the performed measurements. The average sensitivity of -78.2 mV pH^{-1} was coupled with a SD of ± 3.37 mV pH^{-1}, translating to 4.3 % RSD (N=8). The average standard electrode potential value showed higher variability with -148.3 ± 35.19 mV, 23.7 % RSD (N=8). It is common for the intercept values to show a higher degree of uncertainty [26], which might result from inconsistencies in the manufacturing process. Still, this discrepancy can be compensated through sensor calibration. These results convey good sensor reproducibility, which is crucial for validating the sensor fabrication process. However, this can be improved by implementing a standardized manufacturing process with precise steps, control, and additional studies that could eventually lead to sensors ready for use from factory calibration, allowing for the upscaling of the fabrication process.

Sensor Stability

Another critical parameter to be analyzed in sensor performance is sensor stability. To achieve the main goal of sensor implementation within smart bandages and wound dressings, the pH sensor must be able to endure long periods of exposure to wound exudate while maintaining its ability to measure pH correctly. To test this, a sensor was immersed in a BR solution of ≈5 pH, following the previously used experimental setup (Figure 4.19). SWV scans were made every hour, for 24 hours, and the riboflavin redox peak position was tracked in every scan. A pH meter served as a reference for the natural shift in solution pH. Figure 5.29 reports the achieved results. The test showed good stability, with the sensor displaying a characteristic riboflavin peak for 16 hours and an average peak shift of 3.2 mV H^{-1}, which may be linked to the natural pH variations registered by the pH

meter. These are promising results despite being below the required time since wound dressings usually need to be changed daily or every two days, depending on the wound status and type. One should also bear in mind that this test was conducted under extreme conditions with the sensor fully immersed in liquid with constant agitation, unlike what would be encountered in a wound environment.

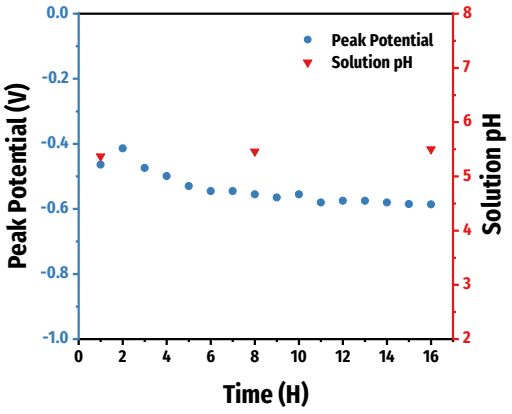

Figure 5.29: pH sensor stability over a 16 hour period of full immersion within BR buffer solution showing a peak drift of 3.2 mV H^{-1}.

Sensor Comparison

Table 5.5 reports the average pH sensor absolute sensitivity values for different voltammetric and potentiometric approaches to pH measuring devices developed in recent years.

From Table 5.5, it is possible to verify that the sensors produced during this work present an average pH sensitivity and linear range values on par with other approaches found in the literature. The achieved sensitivity is even higher than the riboflavin-modified LIG on PI pH sensors reported by Cameron et al. [4], and Casimero et al. [11].

Table 5.5: Absolute pH sensitivity value comparison between different sensor approaches.

Sensor	Type*	Sensitivity (mV pH^{-1})	Linear Range (pH)	Ref.
Bare LIG	Pot.	24	3-8	[4]
Graphene oxide	Pot.	46	4-10	[92]
PANI	Pot.	54	4-8	[68]
PANI	Pot.	66	4-7	[96]
PANI	Pot.	62	4-10	[63]
PANI	Pot.	62	2-8	[50]
Iridium oxide	Volt.	121	2-8	[12]
Graphite	Volt.	57	2-13	[20]
Riboflavin	Volt.	55	2-8	[11]
Riboflavin	Volt.	56	3-8	[4]
Riboflavin	Volt.	78	2-8	This work

* The sensor type refers to the technique used to measure pH, the options being Potentiometric (Pot.), or Voltammetric (Volt.).

5.3 Cost Analysis of the Sensor Fabrication Process

In order to verify the sensor met the low-cost motivation set out at the beginning of this work, an analysis of the cost of fabrication of the pH sensor was performed (Table 5.6). These calculations did not take into account the electricity expenses and equipment wear during the fabrication process, namely with the use of the CO_2 laser, although this will come much less expensive than CVD-based graphene, that costs ≈2 cents per cm^2 at Sigma-Aldrich. An approximate cost of 2.36 cents (0.0236 €) per unit was determined, which comes to show the proposed device is indeed a low-cost instrument. Albeit, there is still room for improvement as the most significant expense stemmed from the silver ink application to establish the electrical contacts, which was done by hand with a paintbrush, leading to some wasted ink. A standardized and optimized painting process could tackle this issue, as well as the use of other sensor architectures with smaller electrical contact areas that still assured good connectivity, are both ways of reducing the wasted ink and lowering the cost per sensor.

Table 5.6: pH sensor fabrication cost analysis.

Material	Quantity per Sensor*	Price per Quantity	Price per Sensor
Whatman paper	2.68 cm^2	0.00075 € cm^{-2}	0.00201 €
Fire retardant	0.01096 g	0.07980 € g^{-1}	0.00087 €
Wax	2.68 cm^2	0.00083 € cm^{-2}	0.00224 €
Laminating pouches	2.68 cm^2	0.00142 € cm^{-2}	0.00379 €
Silver ink	0.00289 g	4.72 € g^{-1}	0.01366 €
Ag/AgCl ink	0.00019 g	4.26 € g^{-1}	0.00080 €
Riboflavin	1.80×10^{-5} g	111.12 € g^{-1}	0.00020 €
Total			**0.02358 €**

* The sensor area was considered to be a 2.00 by 1.34 cm rectangle capable of fitting an entire sensor inside with a safe border all around.

5.4 pH Sensor Prototype Implementation

A possible prototype implementation within a commercial bandage was envisioned (Figure 5.30), taking inspiration from the device proposed by Pal et al. [60]. The pH sensor was fabricated following the steps reported in Chapter 4, with some alterations. When laser cutting the laminating pouch openings for the electrical contacts, both sides of the passivation layer were cut. This was done to allow the electrical contacts to be established on the backside of the sensor using silver ink. The exposed electrical tracks on the front side were isolated using Kapton tape. The sensor was placed within a commercial bandage, between the cotton padding, which provides continuous contact of the sensor's working area with wound exudate, and the porous back sheet, which had three openings laser cut and aligned with the contacts. A PalmSens' Sensit Smart portable mini-potentiostat, available at CENIMAT|i3N, could then be connected to the sensor by placing the three pins in contact with the respective WE, CE, and RE contacts. The potentiostat was connected to a smartphone via a USB type-c connection, and all measurements could easily be performed using the PSTouch app. All SWV data could then be exported for evaluation and determination of the wound pH value, allowing for the wound pH to be monitored until the bandage has to be changed and the sensor disposed. A similar implementation can be achieved within medical wound dressings to monitor larger wounds, with the possibility of incorporating an array of pH sensors instead of a single sensor, to achieve 2D mapping of wound pH.

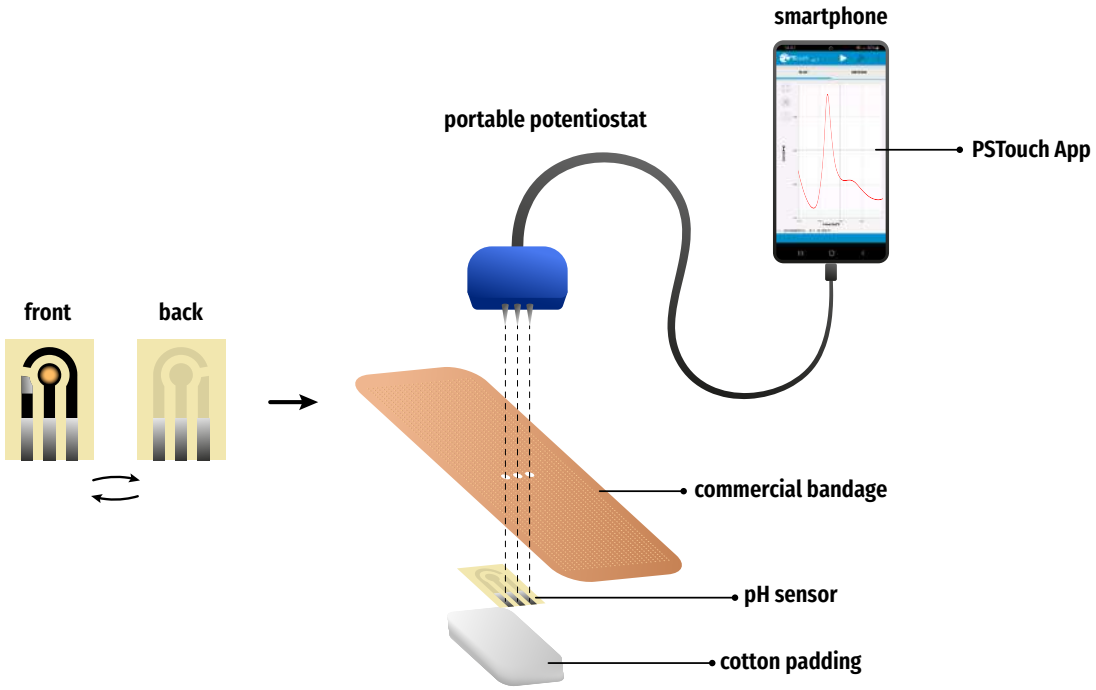

Figure 5.30: Prototype implementation of the pH sensor within a commercial wound bandage.

Chapter 6

Conclusions and Future Work

The main goal of this dissertation project of LIG technique implementation in the production of low-cost pH sensors on sustainable substrates, namely paper, has been achieved. The fabricated device proved to be a suitable solution for a point-of-care and wearable pH monitoring platform for application within a wound environment due to its biocompatibility, low cost, physiologically relevant sensing performance, and being environmentally friendly.

Initially, thorough optimization of laser parameters for LIG fabrication on paper was performed to achieve the best electrode performance. LIG pH sensors were functionalized by WE modification with riboflavin via drop-casting. pH measurements were performed using a voltammetric approach by exploring the electrochemical response of riboflavin at different pH values.

A systematic study was carried out to optimize the laser procedure conditions to yield LIG with the best electrical, chemical, and morphological properties from the paper substrate. Laser power, speed, defocus level, and the number of laser scans were the parameters under consideration throughout this initial task. Laser power vs. speed matrices showed that a balance between laser power and speed was required for the LIG conversion to occur. Graphene-inducing parameters were found where power and speed percentages were similar (main diagonal of the matrices). However, excess carbonization and substrate ablation occurred if power was increased and, if much lower than the speed percentage, no laser effect would be seen on the substrate. SEM analysis was employed to evaluate the effect of laser irradiation on the cellulose fibers and observe any morphological alterations. XPS was used to perform surface chemical analysis and confirm the conversion of the cellulose fibers to graphene structures. EDS also gave insight into the chemical composition of the samples, showing a significant rise in carbon content upon laser irradiation. Next, Raman spectroscopy revealed the effect that laser

power increase had on the quality of the produced LIG, giving information about the number of defects and layers of the graphene stacked structures. Furthermore, electrical performance was assessed from sheet resistance measurements, from which an optimum defocus level of 0.79 mm (z = -0.10") was determined. The effect of multiple laser scans was analyzed from sheet resistance measurements, where a decrease in resistance values was observed throughout the laser settings combinations, reaching a minimum of 14.0 ± 1.50 Ω sq^{-1} with three laser scans with P7S8.

Extensive electrochemical characterization was conducted with CV scans to evaluate the electron transfer properties of LIG sensors. This allowed the establishment of P6S6 as the go-to parameters for sensor fabrication, which, despite not having the absolute highest k^0 and ECA values, led to less variability and some of the highest k^0 and ECA values. Beyond that, sensors with higher porosity (from two lasing scans, for example) led to frequent leakages, inducing short-circuits when testing, making them unviable for sensor application, despite having great electrochemical performance.

The proposed pH sensor was fabricated using the optimized laser settings and subsequently performing WE modification with riboflavin. pH response was tested by SWV scans with the sensor submerged within BR buffer solutions with pH values ranging between ≈2 and ≈10. To evaluate the sensor performance, the potential at which the characteristic riboflavin redox peak occurred was registered for the different pH solutions, which revealed a clear linear dependence of the riboflavin peak shift with pH. A total of 8 sensors were tested, and sensor sensitivity was acquired from the slope of the calibration curve, resulting in an average Super-Nernstian sensitivity of 78.2 ± 3.37 mV pH^{-1} (4 % RSD) across the physiologically relevant 2 to 8 pH linear range, showing great reproducibility as well. Stability test showed great potential of implementation with the sensor enduring 16 hours of complete immersion with hourly pH measurements, with a shift of 3.2 mV H^{-1}. The average standard electrode potential saw higher variability with -148.3 ± 35.19 mV pH^{-1} (24 % RSD), although this can be compensated with sensor calibration. Cost analysis showed the true low-cost nature of the fabricated sensor, coming about at a price of ≈2 cents per unit.

Finally, a possible prototype implementation within a commercial wound bandage or medical wound dressing is presented, where the sensor is placed between the cotton padding and adhesive back sheet and connected to a smartphone via a portable potentiostat. Measurements can be performed on a smartphone using the PSTouch app and then exported for data analysis.

Overall, this thesis project contributed to the expansion of lab-on-paper technology and LIG applications in the biomedical field, in particular to the wearable sensors sector. Beyond that, it serves as a building block for LIG on paper application expansion mainly in the fabrication of other electrochemical biosensors using this novel technique.

Nevertheless, some perspectives for future research arise from this work. First, there is a need for the standardization of the pH sensor fabrication process because many of its steps, like electrical contact establishment, electrode modification, or substrate

mounting, are prone to human error, which leads to higher variability, cost, and lower performance, hindering the possibility of upscaling. Sensor flexibility studies must be conducted to evaluate sensor functioning under various conformations. This is required for sensor implementation, for example, near a joint or any curved body surface, where the device must be flexible while retaining its pH sensitivity profile. Additional tests must be performed to validate and enable sensor deployment within wound environments, namely with natural or artificial wound exudate samples trials. Furthermore, riboflavin concentration and modification techniques could be optimized to lead to better sensing results. Other WE modifications and sensor approaches could be explored with different active molecules, like PANI by electrodeposition, with the aim of WE functionalization within a potentiometric system approach for continuous measurements. Lastly, different prototype implementations could be explored with the attachment of, for example, a wireless, mini-potentiostat directly to the sensor, capable of remotely sending the SWV data to the user or physician and allowing for long-distance monitoring.

As a final remark, the developed pH sensor contributes as a low-cost, sustainable and potentially efficient approach to pH monitoring within wound environment, which can ultimately better the lives of patients by preventing complications with on-time wound status diagnosis and reducing appointments, as well as the unnecessary costs for national healthcare systems. Furthermore, it opens the possibility for scalable applications with, for example, the implementation of wireless communication of results and arrays of miniaturized sensors capable of 2D mapping of the wound pH, for a more detailed control.

Bibliography

[1] Z. Altintas. *Biosensors and Nanotechnology*. Ed. by Z. Altintas. Hoboken, NJ, USA: John Wiley Sons, Inc., Jan. 2018, pp. 3–4. ISBN: 9781119065036. DOI: 10.1002/9781119065036.

[2] J. An et al. "Single-Step Selective Laser Writing of Flexible Photodetectors for Wearable Optoelectronics". In: *Advanced Science* 5.8 (Aug. 2018), p. 1800496. ISSN: 21983844. DOI: 10.1002/advs.201800496.

[3] C. B. Arnold and A. Piqué. "Laser Direct-Write Processing". In: *MRS Bulletin* 32.1 (Jan. 2007), pp. 9–15. ISSN: 0883-7694. DOI: 10.1557/mrs2007.9.

[4] R. Barber et al. "Laser induced graphene sensors for assessing pH: Application to wound management". In: *Electrochemistry Communications* 123 (Feb. 2021), p. 106914. ISSN: 13882481. DOI: 10.1016/j.elecom.2020.106914.

[5] M. S. Brown, B. Ashley, and A. Koh. "Wearable Technology for Chronic Wound Monitoring: Current Dressings, Advancements, and Future Prospects". In: *Frontiers in Bioengineering and Biotechnology* 6 (Apr. 2018), p. 47. ISSN: 2296-4185. DOI: 10.3389/fbioe.2018.00047.

[6] D. A. C. Brownson and C. E. Banks. *The Handbook of Graphene Electrochemistry*. London: Springer London, 2014, pp. 36–57. ISBN: 978-1-4471-6427-2. DOI: 10.1007/978-1-4471-6428-9.

[7] G. S. Bumbrah and R. M. Sharma. "Raman spectroscopy – Basic principle, instrumentation and selected applications for the characterization of drugs of abuse". In: *Egyptian Journal of Forensic Sciences* 6.3 (Sept. 2016), pp. 209–215. ISSN: 2090536X. DOI: 10.1016/j.ejfs.2015.06.001.

[8] M. J. Burns. "Quick Dirty Review of Resistivity Measurement Techniques". In: *Measurement Techniques* (2000).

[9] S. Cameron et al. "Laser Scribed Polyimide as a Platform for Monitoring pH within Smart Bandages". In: *2020 7th International Conference on Signal Processing and Integrated Networks (SPIN)*. IEEE, Feb. 2020, pp. 654–658. ISBN: 978-1-7281-5475-6. DOI: 10.1109/SPIN48934.2020.9070956.

[10] M. C. Carneiro et al. "Homemade 3-carbon electrode system for electrochemical sensing: Application to microRNA detection". In: *Microchemical Journal* 138 (May 2018), pp. 35–44. ISSN: 0026265X. DOI: 10.1016/j.microc.2017.12.026.

[11] C. Casimero et al. "Sensor systems for bacterial reactors: A new flavin-phenol composite film for the in situ voltammetric measurement of pH". In: *Analytica Chimica Acta* 1027 (Oct. 2018), pp. 1–8. ISSN: 00032670. DOI: 10.1016/j.aca.2018.04.053.

[12] K. Chaisiwamongkhol, C. Batchelor-McAuley, and R. G. Compton. "Optimising amperometric pH sensing in blood samples: an iridium oxide electrode for blood pH sensing". In: *The Analyst* 144.4 (2019), pp. 1386–1393. ISSN: 0003-2654. DOI: 10.1039/C8AN02238K.

[13] Y. Chyan et al. "Laser-Induced Graphene by Multiple Lasing: Toward Electronics on Cloth, Paper, and Food". In: *ACS Nano* 12.3 (Mar. 2018), pp. 2176–2183. ISSN: 1936-0851. DOI: 10.1021/acsnano.7b08539.

[14] D. Cialla-May, M. Schmitt, and J. Popp. "1. Theoretical principles of Raman spectroscopy". In: *Micro-Raman Spectroscopy*. De Gruyter, Jan. 2020, pp. 1–14. DOI: 10.1515/9783110515312-001.

[15] K. F. Cutting. "Wound exudate: composition and functions". In: *British Journal of Community Nursing* 8.Sup3 (Sept. 2003), S4–S9. ISSN: 1462-4753. DOI: 10.12968/bjcn.2003.8.Sup3.11577.

[16] W. H. Eaglstein and V. Falanga. "CHRONIC WOUNDS". In: *Surgical Clinics of North America* 77.3 (June 1997), pp. 689–700. ISSN: 00396109. DOI: 10.1016/S0039-6109(05)70575-2.

[17] R. Edwards and K. G. Harding. "Bacteria and wound healing". In: *Current Opinion in Infectious Diseases* 17.2 (Apr. 2004), pp. 91–96. ISSN: 0951-7375. DOI: 10.1097/00001432-200404000-00004.

[18] M. F. El-Kady et al. "Laser Scribing of High-Performance and Flexible Graphene-Based Electrochemical Capacitors". In: *Science* 335.6074 (Mar. 2012), pp. 1326–1330. ISSN: 0036-8075. DOI: 10.1126/science.1216744.

[19] N. Elgrishi et al. "A Practical Beginner's Guide to Cyclic Voltammetry". In: *Journal of Chemical Education* 95.2 (Feb. 2018), pp. 197–206. ISSN: 0021-9584. DOI: 10.1021/acs.jchemed.7b00361.

[20] F. E. Galdino et al. "Graphite Screen-Printed Electrodes Applied for the Accurate and Reagentless Sensing of pH". In: *Analytical Chemistry* 87.23 (Dec. 2015), pp. 11666–11672. ISSN: 0003-2700. DOI: 10.1021/acs.analchem.5b01236.

[21] Gamry. *Potentiostat/Galvanostat Electrochemical Instrument Basics*. URL: https://www.gamry.com/application-notes/instrumentation/potentiostat-fundamentals/ (visited on 11/10/2021).

[22] A. García-Miranda Ferrari et al. "Determination of the Electrochemical Area of Screen-Printed Electrochemical Sensing Platforms". In: *Biosensors* 8.2 (June 2018), p. 53. ISSN: 2079-6374. DOI: 10.3390/bios8020053.

[23] A. K. Geim. "Graphene: Status and Prospects". In: *Science* 324.5934 (June 2009), pp. 1530–1534. ISSN: 0036-8075. DOI: 10.1126/science.1158877.

[24] A. K. GEIM and K. S. NOVOSELOV. "The rise of graphene". In: *Nanoscience and Technology*. Co-Published with Macmillan Publishers Ltd, UK, Aug. 2009, pp. 11–19. ISBN: 9789814287005. DOI: 10.1142/9789814287005_0002. arXiv: 0702595 [cond-mat].

[25] E. Gieva, G. Nikolov, and B. Nikolova. "Sheet Resistance Measurement of Inkjet Printed Layers". In: *2019 42nd International Spring Seminar on Electronics Technology (ISSE)*. Vol. 2019-May. IEEE, May 2019, pp. 1–6. ISBN: 978-1-7281-1874-1. DOI: 10.1109/ISSE.2019.8810284.

[26] T. Guinovart et al. "Bandage-Based Wearable Potentiometric Sensor for Monitoring Wound pH". In: *Electroanalysis* 26.6 (June 2014), pp. 1345–1353. ISSN: 10400397. DOI: 10.1002/elan.201300558.

[27] S. Guo and L. DiPietro. "Factors Affecting Wound Healing". In: *Journal of Dental Research* 89.3 (Mar. 2010), pp. 219–229. ISSN: 0022-0345. DOI: 10.1177/0022034509359125.

[28] D. Jankowska et al. "Simultaneous detection of pH value and glucose concentrations for wound monitoring applications". In: *Biosensors and Bioelectronics* 87 (Jan. 2017), pp. 312–319. ISSN: 09565663. DOI: 10.1016/j.bios.2016.08.072.

[29] K. Järbrink et al. "Prevalence and incidence of chronic wounds and related complications: a protocol for a systematic review". In: *Systematic Reviews* 5.1 (Dec. 2016), p. 152. ISSN: 2046-4053. DOI: 10.1186/s13643-016-0329-y.

[30] W. B. Jensen. "The Symbol for pH". In: *Journal of Chemical Education* 81.1 (Jan. 2004), p. 21. ISSN: 0021-9584. DOI: 10.1021/ed081p21.

[31] N. John and S. George. "Raman Spectroscopy". In: *Spectroscopic Methods for Nanomaterials Characterization*. Elsevier, 2017, pp. 95–127. ISBN: 9780323461405. DOI: 10.1016/B978-0-323-46140-5.00005-4.

[32] F. Keywell and G. Dorosheski. "Measurement of the Sheet Resistivity of a Square Wafer with a Square Four-Point Probe". In: *Review of Scientific Instruments* 31.8 (Aug. 1960), pp. 833–837. ISSN: 0034-6748. DOI: 10.1063/1.1717065.

[33] J. P. Kirby and J. E. Mazuski. "Prevention of Surgical Site Infection". In: *Surgical Clinics of North America* 89.2 (Apr. 2009), pp. 365–389. ISSN: 00396109. DOI: 10.1016/j.suc.2009.01.001.

[34] R. J. Klingler and J. K. Kochi. "Electron-transfer kinetics from cyclic voltammetry. Quantitative description of electrochemical reversibility". In: *The Journal of Physical Chemistry* 85.12 (June 1981), pp. 1731–1741. ISSN: 0022-3654. DOI: 10.1021/j150612a028.

[35] H. Konno. "X-ray Photoelectron Spectroscopy". In: *Materials Science and Engineering of Carbon*. Elsevier, 2016, pp. 153–171. ISBN: 9780128052563. DOI: 10.1016/B978-0-12-805256-3.00008-8.

[36] S. J. Konopka and B. McDuffie. "Diffusion coefficients of ferri- and ferrocyanide ions in aqueous media, using twin-electrode thin-layer electrochemistry". In: *Analytical Chemistry* 42.14 (Dec. 1970), pp. 1741–1746. ISSN: 0003-2700. DOI: 10.1021/ac50160a042.

[37] I. S. Kucherenko et al. "Laser-induced graphene electrodes for electrochemical ion sensing, pesticide monitoring, and water splitting". In: *Analytical and Bioanalytical Chemistry* 413.25 (Oct. 2021), pp. 6201–6212. ISSN: 1618-2642. DOI: 10.1007/s00216-021-03519-w.

[38] B. Kulyk et al. "Laser-Induced Graphene from Paper for Mechanical Sensing". In: *ACS Applied Materials Interfaces* 13.8 (Mar. 2021), pp. 10210–10221. ISSN: 1944-8244. DOI: 10.1021/acsami.0c20270.

[39] M. Kumar. "Biosensor: A Hope for Our Future". In: *International Journal of Science and Research (IJSR)* 6.11 (2017), pp. 334–337. ISSN: 2319-7064.

[40] I. Lavagnini, R. Antiochia, and F. Magno. "An Extended Method for the Practical Evaluation of the Standard Rate Constant from Cyclic Voltammetric Data". In: *Electroanalysis* 16.6 (Apr. 2004), pp. 505–506. ISSN: 1040-0397. DOI: 10.1002/elan.200302851.

[41] T. Li et al. "Developing fibrillated cellulose as a sustainable technological material". In: *Nature* 590.7844 (Feb. 2021), pp. 47–56. ISSN: 0028-0836. DOI: 10.1038/s41586-020-03167-7.

[42] J. Lin et al. "Laser-induced porous graphene films from commercial polymers". In: *Nature Communications* 5.1 (Dec. 2014), p. 5714. ISSN: 2041-1723. DOI: 10.1038/ncomms6714.

[43] Z. J. Lo et al. "Clinical and economic burden of wound care in the tropics: a 5-year institutional population health review". In: *International Wound Journal* 17.3 (June 2020), pp. 790–803. ISSN: 1742-4801. DOI: 10.1111/iwj.13333.

[44] S. Luo, P. T. Hoang, and T. Liu. "Direct laser writing for creating porous graphitic structures and their use for flexible and highly sensitive sensor and sensor arrays". In: *Carbon* 96 (Jan. 2016), pp. 522–531. ISSN: 00086223. DOI: 10.1016/j.carbon.2015.09.076.

[45] G. A. Mabbott. "An introduction to cyclic voltammetry". In: *Journal of Chemical Education* 60.9 (Sept. 1983), p. 697. ISSN: 0021-9584. DOI: 10.1021/ed060p697.

[46] M. Machado. "Laser induced / scribed graphene electrodes for all- printed transistors". PhD thesis. Nova School of Science and Technology, 2017. DOI: http://hdl.handle.net/10362/118783118783.

[47] G. D. M. Madeira et al. "Model improvement for super-Nernstian pH sensors: the effect of surface hydration". In: *Journal of Materials Science* 56.3 (Jan. 2021), pp. 2738–2747. ISSN: 0022-2461. DOI: 10.1007/s10853-020-05412-w.

[48] E. R. Mamleyev et al. "Laser-induced hierarchical carbon patterns on polyimide substrates for flexible urea sensors". In: *npj Flexible Electronics* 3.1 (Dec. 2019), p. 2. ISSN: 2397-4621. DOI: 10.1038/s41528-018-0047-8.

[49] R. Martins, I. Ferreira, and E. Fortunato. "Electronics with and on paper". In: *physica status solidi (RRL) - Rapid Research Letters* 5.9 (Sept. 2011), pp. 332–335. ISSN: 18626254. DOI: 10.1002/pssr.201105247.

[50] F. Mazzara et al. "PANI-Based Wearable Electrochemical Sensor for pH Sweat Monitoring". In: *Chemosensors* 9.7 (July 2021), p. 169. ISSN: 2227-9040. DOI: 10.3390/chemosensors9070169.

[51] A. McLister et al. "New Developments in Smart Bandage Technologies for Wound Diagnostics". In: *Advanced Materials* 28.27 (July 2016), pp. 5732–5737. ISSN: 09359648. DOI: 10.1002/adma.201504829.

[52] Metrohm. "Basic overview of the working principle of a potentiostat/galvanostat (PGSTAT) – Electrochemical cell setup". In: *Autolab Application Note EC08* (2011), pp. 1–3.

[53] Z. Moore and H. Strapp. "Managing the problem of excess exudate". In: *British Journal of Nursing* 24.Sup15 (Aug. 2015), S12–S17. ISSN: 0966-0461. DOI: 10.12968/bjon.2015.24.Sup15.S12.

[54] R. Murray et al. "Design of Experiments and Optimization of Laser-Induced Graphene". In: *ACS Omega* 6.26 (July 2021), pp. 16736–16743. ISSN: 2470-1343. DOI: 10.1021/acsomega.1c00309.

[55] S. Nakata et al. "Wearable, Flexible, and Multifunctional Healthcare Device with an ISFET Chemical Sensor for Simultaneous Sweat pH and Skin Temperature Monitoring". In: *ACS Sensors* 2.3 (Mar. 2017), pp. 443–448. ISSN: 2379-3694. DOI: 10.1021/acssensors.7b00047.

[56] R. S. Nicholson. "Theory and Application of Cyclic Voltammetry for Measurement of Electrode Reaction Kinetics." In: *Analytical Chemistry* 37.11 (Oct. 1965), pp. 1351–1355. ISSN: 0003-2700. DOI: 10.1021/ac60230a016.

[57] K. S. Novoselov. "Electric Field Effect in Atomically Thin Carbon Films". In: *Science* 306.5696 (Oct. 2004), pp. 666–669. ISSN: 0036-8075. DOI: 10.1126/science.1102896.

[58] K. S. Novoselov et al. "A roadmap for graphene". In: *Nature* 490.7419 (Oct. 2012), pp. 192–200. ISSN: 0028-0836. DOI: 10.1038/nature11458.

[59] K Ousey et al. "The importance of hydration in wound healing: reinvigorating the clinical perspective". In: *Journal of Wound Care* 25.3 (Mar. 2016), pp. 122–130. ISSN: 0969-0700. DOI: 10.12968/jowc.2016.25.3.122.

[60] A. Pal et al. "Early detection and monitoring of chronic wounds using low-cost, omniphobic paper-based smart bandages". In: *Biosensors and Bioelectronics* 117.April (Oct. 2018), pp. 696–705. ISSN: 09565663. DOI: 10.1016/j.bios.2018.06.060.

[61] PalmSens. *PalmSens4 - PalmSens*. URL: https://www.palmsens.com/product/palmsens4/?gclid=Cj0KCQjwrJOMBhCZARIsAGEd4VF1r5myjLlQF50ZLuuLgy9fvig0OTyl5-cnouwxTH1lJGr8IF8YTAQaAgISEALw_wcB (visited on 11/06/2021).

[62] Q. Pang et al. "Smart Flexible Electronics-Integrated Wound Dressing for Real-Time Monitoring and On-Demand Treatment of Infected Wounds". In: *Advanced Science* 7.6 (Mar. 2020), p. 1902673. ISSN: 2198-3844. DOI: 10.1002/advs.201902673.

[63] H. J. Park et al. "Potentiometric performance of flexible pH sensor based on polyaniline nanofiber arrays". In: *Nano Convergence* 6.1 (Dec. 2019), p. 9. ISSN: 2196-5404. DOI: 10.1186/s40580-019-0179-0.

[64] H. Park et al. "Electronic Functionality Encoded Laser-Induced Graphene for Paper Electronics". In: *ACS Applied Nano Materials* 3.7 (July 2020), pp. 6899–6904. ISSN: 2574-0970. DOI: 10.1021/acsanm.0c01255.

[65] T. Pinheiro et al. "Laser-Induced Graphene on Paper toward Efficient Fabrication of Flexible, Planar Electrodes for Electrochemical Sensing". In: *Advanced Materials Interfaces* 8.22 (Nov. 2021), p. 2101502. ISSN: 2196-7350. DOI: 10.1002/admi.202101502.

[66] M. Pohanka and P. Skládal. "Electrochemical biosensors - principles and applications". In: *Journal of Applied Biomedicine* 6.2 (July 2008), pp. 57–64. ISSN: 1214021X. DOI: 10.32725/jab.2008.008.

[67] G Power, Z Moore, and T. O'Connor. "Measurement of pH, exudate composition and temperature in wound healing: a systematic review". In: *Journal of Wound Care* 26.7 (July 2017), pp. 381–397. ISSN: 0969-0700. DOI: 10.12968/jowc.2017.26.7.381.

[68] M. Punjiya et al. "A flexible pH sensing smart bandage with wireless CMOS readout for chronic wound monitoring". In: *2017 19th International Conference on Solid-State Sensors, Actuators and Microsystems (TRANSDUCERS)*. IEEE, June 2017, pp. 1700–1702. ISBN: 978-1-5386-2732-7. DOI: 10.1109/TRANSDUCERS.2017.7994393.

[69] Y. Qiao et al. "Graphene-based wearable sensors". In: *Nanoscale* 11.41 (2019), pp. 18923–18945. ISSN: 2040-3364. DOI: 10.1039/C9NR05532K.

[70] Y. Qin et al. "Microfabricated electrochemical pH and free chlorine sensors for water quality monitoring: recent advances and research challenges". In: *RSC Advances* 5.85 (2015), pp. 69086–69109. ISSN: 2046-2069. DOI: 10.1039/C5RA11291E.

[71] E. P. Randviir. "A cross examination of electron transfer rate constants for carbon screen-printed electrodes using Electrochemical Impedance Spectroscopy and cyclic voltammetry". In: *Electrochimica Acta* 286 (Oct. 2018), pp. 179–186. ISSN: 00134686. DOI: 10.1016/j.electacta.2018.08.021.

[72] M. Rippon, K. Ousey, and K. Cutting. "Wound healing and hyper-hydration: a counterintuitive model". In: *Journal of Wound Care* 25.2 (Feb. 2016), pp. 68–75. ISSN: 0969-0700. DOI: 10.12968/jowc.2016.25.2.68.

[73] A. Samouco et al. "Laser-induced electrodes towards low-cost flexible UV ZnO sensors". In: *Flexible and Printed Electronics* 3.4 (Dec. 2018), p. 044002. ISSN: 2058-8585. DOI: 10.1088/2058-8585/aaed77.

[74] A. Samouco. "Laser induced electrodes towards low cost flexible electronics and its applications in a UV sensor". In: (2017), pp. 1–98.

[75] L. A. Schneider et al. "Influence of pH on wound-healing: a new perspective for wound-therapy?" In: *Archives of Dermatological Research* 298.9 (Jan. 2007), pp. 413–420. ISSN: 0340-3696. DOI: 10.1007/s00403-006-0713-x.

[76] A. Selimis, V. Mironov, and M. Farsari. "Direct laser writing: Principles and materials for scaffold 3D printing". In: *Microelectronic Engineering* 132.October (Jan. 2015), pp. 83–89. ISSN: 01679317. DOI: 10.1016/j.mee.2014.10.001.

[77] S. Sharifi et al. "Nanomedicine in Healing Chronic Wounds: Opportunities and Challenges". In: *Molecular Pharmaceutics* 18.2 (Feb. 2021), pp. 550–575. ISSN: 1543-8384. DOI: 10.1021/acs.molpharmaceut.0c00346.

[78] D. Shindo and T. Oikawa. "Energy Dispersive X-ray Spectroscopy". In: *Analytical Electron Microscopy for Materials Science*. Tokyo: Springer Japan, 2002, pp. 81–102. DOI: 10.1007/978-4-431-66988-3_4.

[79] F. Sima et al. "Laser thin films deposition and characterization for biomedical applications". In: *Laser Surface Modification of Biomaterials*. Elsevier, 2016, pp. 77–125. ISBN: 9780081009420. DOI: 10.1016/B978-0-08-100883-6.00003-4.

[80] H. Singhal. *What is the global prevalence of surgical site infections (SSIs)?* 2019. URL: https://www.medscape.com/answers/188988-82339/what-is-the-global-prevalence-of-surgical-site-infections-ssis (visited on 01/27/2021).

[81] F. A. Stevie and C. L. Donley. "Introduction to x-ray photoelectron spectroscopy". In: *Journal of Vacuum Science Technology A* 38.6 (Dec. 2020), p. 063204. ISSN: 0734-2101. DOI: 10.1116/6.0000412.

[82] W.-H. Su et al. "Nonsteroidal Anti-Inflammatory Drugs for Wounds: Pain Relief or Excessive Scar Formation?" In: *Mediators of Inflammation* 2010 (2010), pp. 1–8. ISSN: 0962-9351. DOI: 10.1155/2010/413238.

[83] U. L. Systems. *Available Lenses*. URL: https://www.ulsinc.com/available-lenses (visited on 11/04/2021).

[84] U. L. Systems. *VLS Desktop User Guide VLS2.30, VLS3.50*. 2012. URL: https://www.manualslib.com/manual/827813/Universal-Laser-Systems-Vls2-30.html#product-VLS3.50.

[85] D. R. Thevenot et al. "Electrochemical Biosensors: Recommended Definitions and Classification". In: *Pure and Applied Chemistry* 71.12 (Jan. 1999), pp. 2333–2348. ISSN: 1365-3075. DOI: 10.1351/pac199971122333.

[86] S. K. Tiwari et al. "Graphene research and their outputs: Status and prospect". In: *Journal of Science: Advanced Materials and Devices* 5.1 (Mar. 2020), pp. 10–29. ISSN: 24682179. DOI: 10.1016/j.jsamd.2020.01.006.

[87] D. Tobjörk and R. Österbacka. "Paper Electronics". In: *Advanced Materials* 23.17 (May 2011), pp. 1935–1961. ISSN: 09359648. DOI: 10.1002/adma.201004692.

[88] J. I. de la Torre. *Chronic Wounds: Overview, The Biology of Wound Healing, Common Chronic Wounds*. 2019. URL: https://emedicine.medscape.com/article/1298452-overview#showall (visited on 01/27/2021).

[89] A. Ul-Hamid. *A Beginners' Guide to Scanning Electron Microscopy*. Cham: Springer International Publishing, 2018. ISBN: 978-3-319-98481-0. DOI: 10.1007/978-3-319-98482-7.

[90] C. A. Umscheid et al. "Estimating the Proportion of Healthcare-Associated Infections That Are Reasonably Preventable and the Related Mortality and Costs". In: *Infection Control Hospital Epidemiology* 32.2 (2011), pp. 101–114. ISSN: 0899-823X. DOI: 10.1086/657912.

[91] K. Vernon-Parry. "Scanning electron microscopy: an introduction". In: *III-Vs Review* 13.4 (July 2000), pp. 40–44. ISSN: 09611290. DOI: 10.1016/S0961-1290(00)80006-X.

[92] F Vivaldi et al. "A graphene-based pH sensor on paper for human plasma and seawater". In: *2019 41st Annual International Conference of the IEEE Engineering in Medicine and Biology Society (EMBC)*. IEEE, July 2019, pp. 1563–1566. ISBN: 978-1-5386-1311-5. DOI: 10.1109/EMBC.2019.8856991.

[93] F. Vivaldi et al. "Recent Advances in Optical, Electrochemical and Field Effect pH Sensors". In: *Chemosensors* 9.2 (Feb. 2021), p. 33. ISSN: 2227-9040. DOI: 10.3390/chemosensors9020033.

[94] P.-H. Wang et al. "Wound healing". In: *Journal of the Chinese Medical Association* 81.2 (Feb. 2018), pp. 94–101. ISSN: 1726-4901. DOI: 10.1016/j.jcma.2017.11.002.

[95] R. White and K. F. Cutting. *Modern exudate management: a review of wound treatments*. 2006. URL: http://www.worldwidewounds.com/2006/september/White/Modern-Exudate-Mgt (visited on 02/10/2021).

[96] X. Xuan et al. "A highly stretchable and conductive 3D porous graphene metal nanocomposite based electrochemical-physiological hybrid biosensor". In: *Biosensors and Bioelectronics* 120.August (Nov. 2018), pp. 160–167. ISSN: 09565663. DOI: 10.1016/j.bios.2018.07.071.

[97] Y. Yang and W. Gao. "Wearable and flexible electronics for continuous molecular monitoring". In: *Chemical Society Reviews* 48.6 (2019), pp. 1465–1491. ISSN: 0306-0012. DOI: 10.1039/C7CS00730B.

[98] R. Ye, D. K. James, and J. M. Tour. "Laser-Induced Graphene". In: *Accounts of Chemical Research* 51.7 (July 2018), pp. 1609–1620. ISSN: 0001-4842. DOI: 10.1021/acs.accounts.8b00084.

[99] R. Ye et al. "Laser-Induced Graphene Formation on Wood". In: *Advanced Materials* 29.37 (Oct. 2017), p. 1702211. ISSN: 0935-9648. DOI: 10.1002/adma.201702211.

[100] P. Zhu and Y. Zhao. "Cyclic voltammetry measurements of electroactive surface area of porous nickel: Peak current and peak charge methods and diffusion layer effect". In: *Materials Chemistry and Physics* 233.05 (May 2019), pp. 60–67. ISSN: 02540584. DOI: 10.1016/j.matchemphys.2019.05.034.

[101] C. G. Zoski. *Handbook of electrochemistry*. Elsevier, 2007, pp. 785–809. ISBN: 9780444519580. DOI: 10.1016/B978-0-444-51958-0.X5000-9.

ANNEX I

Raman Ratios and Sheet Resistance Values

In this annex, I_{2D}/I_G and I_D/I_G ratios values and respective relative standard deviation percentages are presented. Furthermore, sheet resistance measurements performed for different laser parameter samples are presented in greater detail, coupled with their respective standard deviations.

Table I.1: Average I_D/I_G and I_{2D}/I_G ratio values and respective standard deviation percentages.

	I_D/I_G		I_{2D}/I_G	
Parameters	**Average**	**RSD (N=5)**	**Average**	**RSD (N=5)**
P4S6 (z = 0.05")	1.12	15 %	0.40	15 %
P4S6 (z = 0.00")	1.01	11 %	0.34	4 %
P4S6 (z = -0.05")	0.82	18 %	0.49	8 %
P4S6 (z = -0.10")	0.99	11 %	0.28	10 %
P5S6	0.58	6 %	0.44	9 %
P6S6	0.63	9 %	0.41	6 %
P7S6	0.71	12 %	0.39	7 %
P7S8 1x	0.55	8 %	0.47	3 %
P7S8 2x	0.68	8 %	0.37	2 %
P7S8 3x	0.61	14 %	0.37	5 %

Table I.2: Average sheet resistance results for different laser parameters at different defocus levels.

	z = -0.05"/ 0.48 mm		z = -0.10"/ 0.79 mm		z = 0.00"/ 1.75 mm		z = 0.05"/ 3.02 mm	
Parameters	$\overline{R_s}$ (Ω **sq**$^{-1}$)	**RSD (N=4)**	$\overline{R_s}$ (Ω **sq**$^{-1}$)	**RSD (N=4)**	$\overline{R_s}$ (Ω **sq**$^{-1}$)	**RSD (N=4)**	$\overline{R_s}$ (Ω **sq**$^{-1}$)	**RSD (N=4)**
P1S1	-		-	-	53075.00	66 %	2514.75	31 %
P2S2	477.00	20 %	-	-	-	-	-	-
P3S3	425.00	15 %	121.63	31 %	-	-	-	-
P3S4	489.75	22 %	-	-	-	-	2043.75	13 %
P3S5	-	-	-	-	-	-	18168.25	116 %
P4S3	-	-	23.38	7 %	-	-	-	-
P4S4	248.00	13 %	57.95	12 %	-	-	-	-
P4S5	419.50	4 %	159.25	20 %	-	-	-	-
P4S6	488.00	52 %	-	-	-	-	4742.00	35 %
P4S7	411.00	10 %	-	-	-	-	2760.75	34 %
P4S8	-	-	-	-	-	-	1485.75	17 %
P5S4	-	-	23.03	3 %	-	-	-	-
P5S5	-	-	33.78	5 %	-	-	-	-
P5S6	611.25	50 %	51.95	8 %	-	-	-	-
P5S7	918.00	9 %	58.63	4 %	-	-	-	-
P5S8	535.50	22 %	92.00	5 %	-	-	-	-
P6S6	-	-	21.85	10 %	-	-	-	-
P6S7	-	-	27.55	3 %	-	-	-	-
P6S8	806.75	41 %	31.83	5 %	-	-	-	-
P7S8	-	-	21.93	11 %	-	-	-	-

Table I.3: Average sheet resistance results for single, double and triple lasing scan.

	1×		2×		3×	
Parameters	$\overline{R_s}$ (Ω **sq**$^{-1}$)	**RSD (N=4)**	$\overline{R_s}$ (Ω **sq**$^{-1}$)	**RSD (N=4)**	$\overline{R_s}$ (Ω **sq**$^{-1}$)	**RSD (N=4)**
P3S3	121.63	31 %	-	-	-	-
P4S3	23.38	7 %	24.33	13 %	-	-
P4S4	57.95	12 %	-	-	-	-
P4S5	159.25	20 %	-	-	-	-
P5S4	23.03	3 %	25.70	3 %	-	-
P5S5	33.78	5 %	21.30	2 %	20.48	14 %
P5S6	51.95	8 %	-	-	-	-
P5S7	58.63	4 %	-	-	-	-
P5S8	92.00	5 %	-	-	-	-
P6S6	21.85	10 %	16.15	2 %	41.68	69 %
P6S7	27.55	3 %	25.98	27 %	15.25	8 %
P6S8	31.83	5 %	28.15	13 %	19.38	3 %
P7S8	21.93	11 %	14.78	2 %	14.00	14 %

ANNEX II

Laser Power and Speed Conversion Chart

This annex serves as a conversion reference for the laser speed and power parameter percentages to standard units. This is useful in the translation of the PXSY syntax for lasing settings combinations, where P and S refer to the power and speed, and X, and Y are its respective percentages.

Table II.1: Laser speed and power percentages conversion to standard units.

Power (%)	**Power (W)**	**Speed (%)**	**Rast Speed (cm s^{-1})**
1	0.5	1	1.27
2	1.0	2	2.54
3	1.5	3	3.81
4	2.0	4	5.08
5	2.5	5	6.35
6	3.0	6	7.62
7	3.5	7	8.89
8	4.0	8	10.16
9	4.5	9	11.43
10	5.0	10	12.70